Electric Vehicle Powertrain Integrated Charging

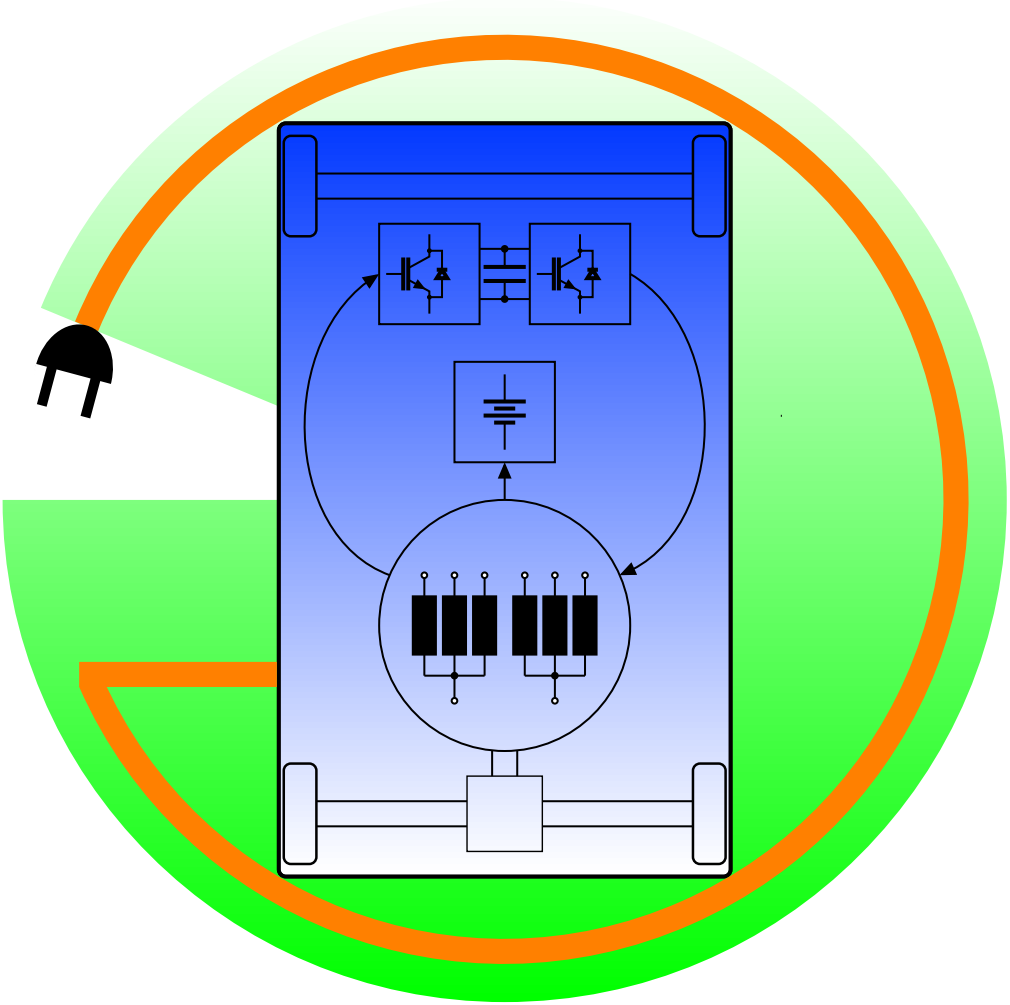

Erik Hoevenaars

Electric Vehicle Powertrain Integrated Charging

Zur Erlangung des akademischen Grades eines

DOKTORS DER INGENIEURWISSENSCHAFTEN (Dr.-Ing.)

von der KIT-Fakultät für
Elektrotechnik und Informationstechnik
des Karlsruher Instituts für Technologie (KIT)
angenommene

DISSERTATION

von
Erik Hoevenaars M.Sc.
geb. in: Gemert, Niederlande

Tag der mündlichen Prüfung:	2. Dezember 2021
Hauptreferent:	Prof. Dr.-Ing. Marc Hiller
Korreferentin:	Prof. Dr.-Ing. Nejila Parspour (Universität Stuttgart)

Acknowledgments

First of all, I would like to thank my doctoral advisor Prof. Dr. Marc Hiller for his continuous guidance, support, and encouragement throughout this work. His advices, feedback, and enthusiasm were crucial to complete this dissertation.
I would also like to thank my supervisor Dr. Philipp Schumann at Robert Bosch GmbH for his valuable feedback, support, and research interest. His advices were a great support to me.
Special thanks to Dr. Norbert Müller and to Wolfgang Volz for the possibility to carry out this work within their departments at the Corporate Sector Research and Advance Engineering at Robert Bosch GmbH in Renningen. I also want to thank my colleagues for all their support and corrections. Thanks to Ulrich Brenner, Dr. Alin Stirban, and Dr. Marina Keller for all the discussions about iron losses and thanks to Taleb Janbein and Tobias Illg for all the passionate conversations about alternative use of the drivetrain. Thanks to Wolfgang Rammaier for carrying out the iron material measurements. Thanks to Dr. Federico Carraro and Dr. Tine Konjedic for the discussions and support with the inverter measurements. Thanks to Oliver Blum, Bernhard Mader, and Jürgen Eckhardt for their support with the practical implementation, and thanks to Moritz Bräuchle for the discussions regarding safety aspects. Thanks to the Bosch PhD students in my department for all the discussions and motivations. I also want to thank my students for all their support and input.
I am grateful to my family and friends, thanks especially to my parents for their support and love. Finally, I would especially like to thank my wife Heather for her endless love, patience, and support during this period of my life. She always motivated me, especially when my ideas did not work out as planned.

Erik Hoevenaars
Stuttgart, April 2021

Abstract

Battery electric vehicles require an AC charger, which is usually located onboard the vehicle, to supply the battery with energy when the vehicle is parked. Integrated charging is a method that aims to minimize charger weight, cost, and volume by integration of the charging functionality into other powertrain components that are not used when the vehicle is parked. Charging can be galvanically isolated, or non-isolated if other safety measures e.g. detection and interruption of supply are used to avoid electrical shock. Thirty three state of the art integrated charging methods are found and compared in terms of powertrain use, required components, shaft torque of the e-drive, and efficiency.

A new isolated integrated charger concept is described and aims to improve efficiency while avoiding shaft rotation. The drive system is used as a DC/DC converter with the electrical machine as a transformer at standstill. The rotor needs to be opened to prevent shaft rotation during charging, which is as expensive as a dedicated charger. Theoretical analysis indicates a maximum charger efficiency of 88%. Novel methods for efficiency improvements and integration of energy supply to the board net are proposed and reviewed. The low efficiency and high cost make this concept unsuitable.

In order to avoid these drawbacks, two novel non-isolated charger concepts using a six-phase e-drive as a series connected boost-buck converter are proposed and analyzed in terms of extra components, efficiency, and shaft torque during charging. Drivetrain losses are assessed under charging conditions with DC currents and are based on new material characterizations for the used load conditions. Efficiencies up to 93% are measured and are well within a ±1% deviation of the calculations and simulations. Three concepts for fault current measurements are presented and reviewed with experimental results in order to provide protection against electrical shock for these charger concepts. Silicon carbide inverter technology shows charging efficiencies on par with dedicated chargers at a significantly lower cost level.

Zusammenfassung

Batterieelektrische Fahrzeuge benötigen ein im Fahrzeug eingebautes Ladegerät, um die Energie aus dem Wechselstromnetz für die Gleichstrom-Batterie aufzubereiten. Integriertes Laden ist eine Methode der Integration von Ladefunktionalität in die Antriebsstrangkomponenten, welche während des Parkens außer Betrieb sind, mit dem Ziel, Kosten, Gewicht und Volumen des Ladegerät zu sparen. Das Laden ohne die Sicherheitsmaßnahme einer galvanischen Trennung im Ladegerät ist möglich mit zusätzlichen Maßnahmen gegen elektrischen Schlag, z.B. mit einer Fehlerstromerkennung und entsprechenden Trenneinrichtung. Im Stand der Technik wurden 33 integrierte Ladekonzepte gefunden und bezüglich Antriebsstrangnutzung, benötigte Komponenten, Drehmoment der elektrischen Maschine und Wirkungsgrad verglichen.
Im Rahmen dieser Arbeit wird ein neues galvanisch getrenntes integriertes Ladekonzept beschrieben, mit dem Ziel, die Effizienz zu verbessern und gleichzeitig auftretendes Drehmoment in der Maschine zu vermeiden. Der Antriebsstrang wird als DC/DC-Wandler mit der elektrischen Maschine als Transformator im Stillstand genutzt. Berechnungen zeigen eine maximale Effizienz von 88%. Ansätze zur Verbesserung des Wirkungsgrads und zur Integration des Energieflusses im Bordnetz werden in dieser Arbeit vorgeschlagen und diskutiert. Allerdings muss der Rotorkäfig geöffnet werden, um ein Drehmoment während des Laden zu vermeiden. Dies stellt einen ähnlichen Aufwand dar wie die Darstellung eines separaten Ladegeräts. Somit ist dieses Konzept aus heutiger Sicht wegen niedriger Effizienz und hoher Kosten gegenüber einem separaten Ladegerät nicht konkurrenzfähig.
Zwei Ladekonzepte ohne galvanische Trennung, die eine sechsphasige elektrische Maschine als in Serie geschaltete Hoch- und Tiefsetzsteller nutzen, werden im Rahmen der Arbeit vorgestellt und bezüglich der benötigten Komponenten, der Effizienz und des Drehmoments des Maschine

ausgearbeitet. Die Antriebsstrangverluste werden für die Ladebedingungen mit Gleichströmen analysiert, basierend auf neuen Materialcharakterisierungen für die angewendete Belastung. Es wurden Wirkungsgrade bis zu 93% demonstriert und auch in theoretischen Berechnungen mit einer maximalen Abweichung von ±1% zum experimentellen Befund bestätigt. Zum Schutz gegen elektrischen Schlag bei nicht isolierten Ladekonzepten werden drei Konzepte für eine Fehlerstrommessung präsentiert und anhand von Messergebnissen analysiert. Siliziumkarbid-Inverter-Technologien zeigen in Kombination mit diesen Ladekonzepten Wirkungsgrade, die vergleichbar zu herkömmlichen separaten Ladegeräten sind, und weisen dabei deutlich geringere Kosten auf.

Contents

1

Introduction

Battery Electric Vehicles (BEV) are gaining more and more popularity as an answer to worldwide stricter emission standards [1]. BEV contain an electrical drivetrain (e-drive) that consists of an inverter and an Electrical Machine (EM) for electrical propulsion. Moreover, BEV enclose a High Voltage (HV) to Low Voltage (LV) Direct Current to Direct Current (DC/DC) converter, shortened to LV DC/DC converter, to supply the board net with its auxiliaries. Sometimes, an additional HV DC/DC converter is present to supply an increased and more constant Direct Current (DC) voltage to the inverter. Although this HV DC/DC converter is not required and thus sometimes left out for cost savings, it could provide increased system efficiency when installed [2]. Moreover, BEV are typically equipped with a 400 V battery to store the energy that is withdrawn from the utility grid. These batteries can be charged from dedicated fast DC charging stations in public places. In addition, BEV carry an onboard charger for lower power battery charging, for example at home or at work. These onboard chargers are usually connected to a single- or three-phase Alternating Current (AC) grid, since these power outlets are widely available. The resulting BEV powertrain with onboard charger is illustrated in Fig. 1.1. These onboard chargers contain semiconductors and passive components, i.e. inductors and capacitors, to convert the AC grid voltage into a DC voltage matching the level needed for battery charging. With reported [3] power to volume and weight densities in the range of 2 kW/l and 2 kW/kg, onboard chargers result in added cost, weight, and volume to the vehicle. The aim of integrated charging is to reduce the BEV cost, weight, and/or volume by reuse of existing traction

components such as the e-drive or the DC/DC converter as a battery charger when the vehicle is parked. Integrated charging is possible since most of the drivetrain components are not utilized for their original purposes during charging and also comprise semiconductors, capacitors, and inductors like those in the inverter, the LV or HV DC/DC converter, and in the EM. An overview of this integration approach is presented in Fig. 1.2.

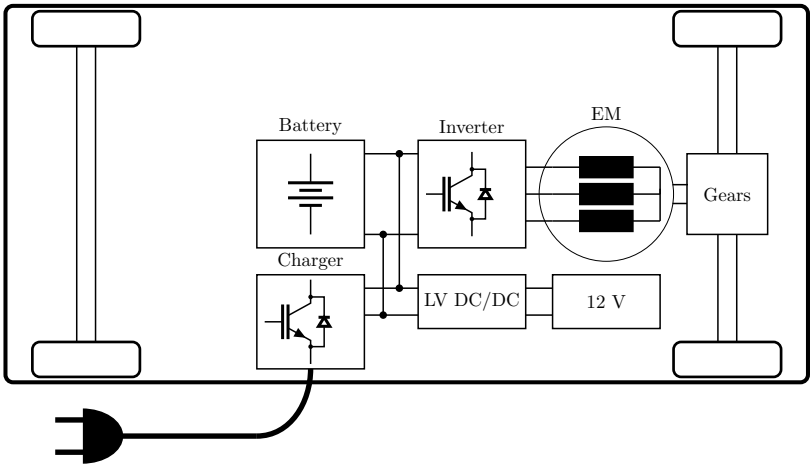

Figure 1.1: BEV with a dedicated onboard charger.

1.1 Project Background

Vehicle batteries have a relatively large voltage swing over the State of Charge (SoC) range i.e. between empty and fully charged, e.g. between 300-400 V. Moreover, the peak value of the single- or three-phase AC grid voltage is usually above the voltage level of an empty battery. Therefore, battery chargers require both voltage step up (boost) and step down (buck) functionality. As a result, integrated battery chargers that only fulfill either boost or buck functionality have to be accompanied by a dedicated converter in order to provide charging functionality across the entire battery SoC range.
Boost and buck functionality can either be implemented with or without galvanic isolation, i.e. a transformer. Although galvanic isolation typically leads

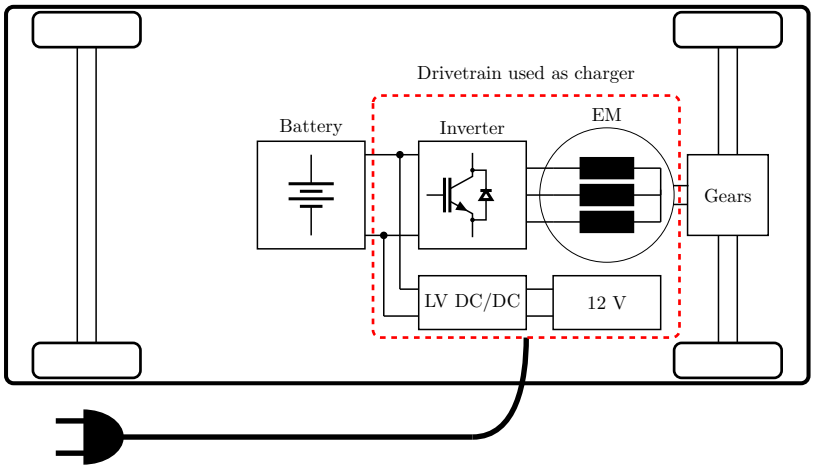

Figure 1.2: BEV using the drivetrain as an integrated onboard charger.

to additional topology complexity with a reduced efficiency, it is sometimes preferred as an additional safety measure against electric shock. An electric shock could occur as a result of residual currents that could flow through the body of the person that is in contact with an exposed potential. Exposed potentials are a result of insulation faults of any part due to a failure of the basic insulation. Basic insulation [4] is the insulation of all hazardous potentials, which normally provides a first layer of protection. An example of the resulting residual current through the body is illustrated in Fig. 1.3.
Although a Residual Current Device (RCD) type A is present in the charging or grid infrastructure as a measure to protect from AC residual currents, it cannot be guaranteed that this RCD will detect non-sinusoidal currents such as DC faults [5]. These DC fault currents shall of course be prevented at all times in order to avoid any harm or damage when exposed to basic insulation failures. Therefore, an additional safety protection in conjunction to the basic insulation is required. Galvanic isolation is a common method of additional protection. Thanks to galvanic isolation, the path of DC fault currents is interrupted by design as shown in Fig. 1.4.
Safety standards [6–9] are assessed to verify alternative methods for an additional safety measure in order to avoid an electrical shock when a DC

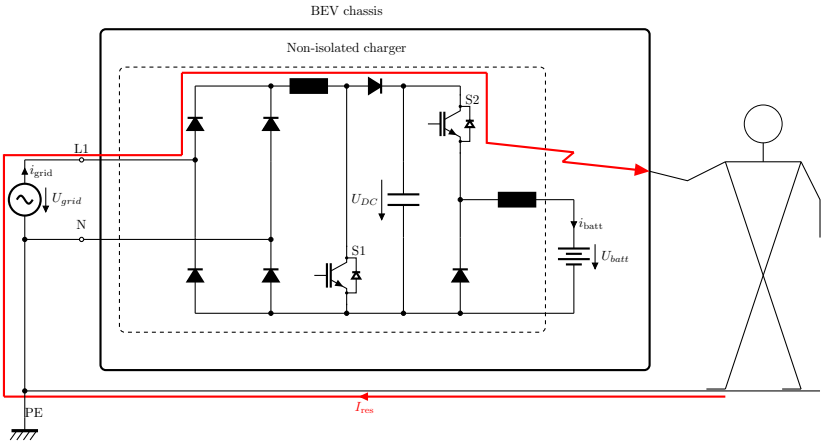

Figure 1.3: Possible circuit in case of an electrical shock.

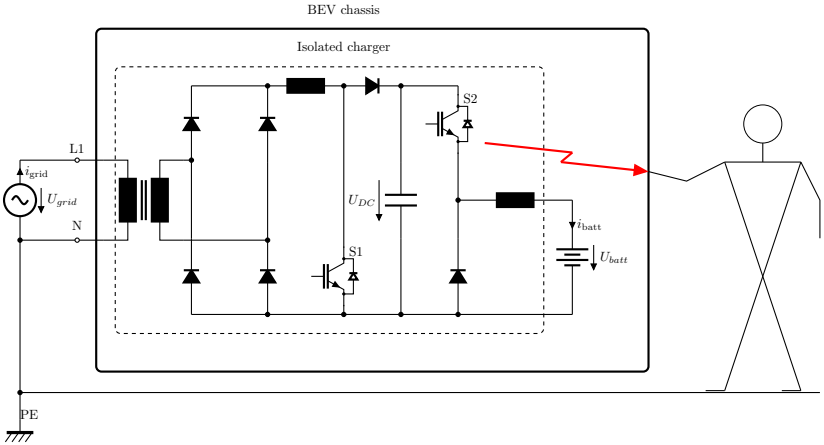

Figure 1.4: Circuit in case of electrical shock is prevented by galvanic isolation.

fault current occurs in a non-isolated integrated charger concept. The applicable markets of each of these standards are presented in Tab. 1.1.

Norm	Topic	Market
ISO 17409	EV charger safety requirements	Worldwide
IEC 61851	EV charger general requirements	Europe
GB 18487	EV charger general requirements	China
UL 2231-1	EV personnel protection requirements	North America

Table 1.1: Overview of reviewed standards for electrical safety.

All safety standards for BEV charging equipment as mentioned in Tab. 1.1 contain similar safety requirements for additional protection against electrical shock. Four possible solutions are provided:

- Double or reinforced insulation as an additional insulation protection in case a fault in the normal insulation occurs.
- Galvanic separation between supply and battery i.e. an isolation transformer within the current path.
- Automatic disconnection of supply in case a fault occurs, e.g. an RCD.
- Separated Extra Low Voltages (SELV) or Protected Extra Low Voltages (PELV), i.e. all voltages below 50 V AC and below 120 V DC.

Since SELV or PELV are not feasible due to the nature of the infrastructure and BEV with grid voltages above 50 V AC and battery voltages above 120 V DC, either improved insulation or a residual current detection mechanism with automatic disconnection of supply is required for integrated charger concepts without galvanic isolation.

1.2 Thesis Contributions

The main objective of the project embedding this thesis is to enhance the research field of e-drive integrated battery chargers. Although many concepts of integrated charging have been presented before, most concepts lack the combination of boost and buck functionality without either low efficiency and/or expensive additional components. Hence, three topologies that aim

to provide more charging functionality while eliminating the drawbacks of previous concepts are presented and described.
In addition to this conceptualization, little is known about the drivetrain losses and efficiency characterizations during charging. Although some measurement results have been presented before, detailed losses breakdowns or calculations were not provided. Therefore, detailed theoretical inverter and EM loss analysis under charging conditions are provided and compared with measurements in order to review and compare the efficiency of these concepts and also to reduce the need for measurements for future concepts or drivetrains.
The main contributions of this thesis are summarized as:

- A detailed overview, systematic categorization, and comparison of state of the art integrated battery chargers and identification of areas for improvements.
- Derivation, analysis, efficiency simulation, and cost breakdown of an isolated integrated charger concept.
- Introduction and review of methods for efficiency improvement and further powertrain functionality integration for the isolated integrated charger concept.
- Mathematical modeling of the inverter and EM copper and iron losses under non-isolated DC biased charging based on material measurements under actual load conditions.
- Introduction of a group of novel single-phase non-isolated integrated charger concepts using a six-phase e-drive as a boost-buck converter and derivation and introduction of two potential useful winding reconnection variants for charging.
- Mathematical modeling, analysis, and comparison of the two derived novel non-isolated integrated charger concepts.
- Reporting of a control method for the selected galvanically coupled integrated charger concepts including experimental implementation and verification.
- Detailed theoretical losses and efficiency analysis including measurements.
- Analysis and comparison of three electrical safety concepts for non-isolated chargers to protect against electrical shock.
- Efficiency improvements analysis for the non-isolated chargers using Silicon Carbide (SiC) technology.

- Recommendations for variants of the introduced non-isolated charger concepts that support three-phase supply.

A total of four scientific publications [E1–E4] and three patent applications [E5–E7] are resulting from the work carried out in this dissertation.

1.3 Thesis Outline

Chapter 2 presents a detailed overview of state of the art integrated battery chargers. A total of 33 concepts are found and grouped in seven categories of powertrain components use: only inverter i.e. no EM involved, a three-phase EM, multiple three-phase EMs, multi-phase machines as inductors, multi-phase EMs as transformer at standstill and with rotation, HV, and LV DC/DC converter. Moreover, five basic reconnections of three-phase machines for charging are identified and described. Finally, chapter 2 is concluded with an overview and comparison including advantages and drawbacks of each category.
In chapter 3, a novel integrated charging concept providing galvanic isolation is introduced. The efficiency and cost of this concept are analyzed, and a novel idea for further drivetrain integration is proposed. In addition, a novel method for efficiency improvements is introduced and reviewed. Although the isolated charger concept is theoretically feasible, it is in practice too expensive and has a too low efficiency.
To overcome these drawbacks of the isolated charger, non-isolated charger concepts are assessed. Therefore, chapter 4 assesses the drivetrain losses theory under DC/DC behavior, which form the basis for efficiency analysis of novel integrated charger concepts that are introduced later. A method for calculation of the EM copper and iron losses under DC biased charging conditions with dominance of the switching ripple is discussed. Moreover, material characterization measurements of the steel laminations are performed as a basis for iron loss calculations. In addition to the EM losses, inverter switching loss measurements are performed for charging conditions with reduced load power.
In chapter 5, two novel non-isolated charger concepts are derived from state of the art reconnection methods for standard three-phase EMs. These novel concepts provide both boost and buck functionality at high efficiency, without generation of shaft torque, and without expensive components. The concepts are analytically described and compared in terms of losses and efficiency, which is verified with experimental results. Furthermore, a control strategy is described and power quality measurements are reported. Finally, three concepts for

protection against electric shock are described and compared as an alternative method for protection against electrical shock for non-isolated battery chargers. Chapter 6 provides an outlook of efficiency enhancements for the non-isolated charger concepts by means of wide bandgap devices. Therefore, the losses and efficiencies using a SiC inverter are presented.
Finally, chapter 7 draws a conclusion on the presented work in this thesis. Furthermore, suggestions for future work are provided.

2

State of Art Integrated Chargers

Many concepts of integrated charging have been presented and discussed in the past [10–64]. Some of these have been compared and categorized before in [10, 11, 45, 50, 57]. This thesis aims to provide a more complete overview and a categorization based on the connection method and number of EMs and other powertrain components used in the charging process. An overview of the different used components and winding connection variants is illustrated in Fig. 2.1. The number in bold text within brackets identifies the section where each concept is discussed. Concepts that only involve the inverter are among the oldest concepts of integrated charging and are described in section 2.1. Concepts that include the inverter and a standard three-phase EM in five different basic reconnection forms are described in section 2.2. Concepts that use multiple EMs are reported in section 2.3 and concepts using one multi-phase EM as inductances or as a transformer are included in section 2.4. In contrast to concepts using the e-drive, some topologies use the HV or LV DC/DC converter. These concepts are summarized in section 2.5. Finally, an overview and comparison of all categories is presented in section 2.6.

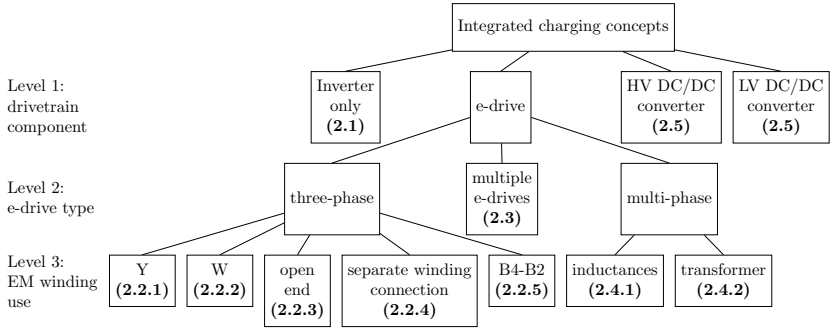

Figure 2.1: Tree diagram with different type of integrated chargers categorized in terms of component type and use.

2.1 Inverter Charger

Some of the oldest methods for integration of charging functionality into the BEV powertrain have been established by using the traction inverter in combination with separate inductors or a transformer as an Alternating Current to Direct Current (AC/DC) converter. Several variants are reported [12–17], which are discussed in this section.

A concept using the traction inverter as a three-phase boost Power Factor Correction (PFC) converter in combination with three separate inductors is presented by Fuji Electric in [12] and shown in Fig. 2.2. In addition to the three inductors, three switches are required to disconnect the EM windings during charging. A single-phase variant using two inductors is patented by Hyundai [13]. One switch is used to disconnect one motor winding and the current through another winding is measured. Charging is only allowed if this winding current equals zero.

Another invention is published by Renault [14] and uses two legs of a three-phase inverter as a single-phase full bridge boost rectifier with PFC functionality. This concept is illustrated in Fig. 2.3. The third inverter leg is connected in series with this boost stage and is operated as a step down converter. Two dedicated inductors are used: one for each conversion step. The EM is disconnected in this concept by means of two switches for the two inverter phases that are used for the boost conversion. Furthermore, a battery reconnection switch is required.

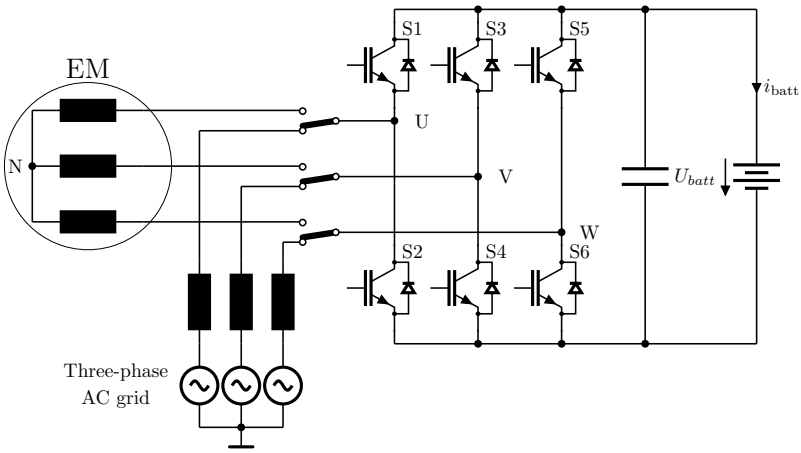

Figure 2.2: Three-phase inverter charger with dedicated inductors.

A galvanically isolated single-phase charger is presented by Sansha Electric in [15] and uses a single-phase transformer instead of an inductor. The concept is drawn in Fig. 2.4. Two out of the three inverter legs are operated as a boost converter. The third inverter leg, as well as the EM windings, are not used in the charging process. No step down functionality is provided. Two switches are required to reconnect the active inverter legs from the EM phases to the secondary transformer winding.
A similar concept, patented by Hitachi in [16], uses an isolation transformer in series with the EM windings as a single-phase boost converter for battery charging. The concept is illustrated in Fig. 2.5 The EM is used in Y connection, which is elaborated in paragraph 2.2.1. No disconnection switches are required since the EM is used in the charging process. However, an extra inverter leg is required to control the current in the secondary winding of the grid connected transformer. A concept using two out of the three inverter legs as a single-phase boost converter with two dedicated inductors and two EM phases with the third inverter leg as a buck converter is published by Renault [17]. In addition to the two required inductors, two traction rated switches are required to disconnect two machine windings from the inverter legs.
The common drawback of all above discussed concepts include the need for dedicated inductors or a transformer. These inductive components are rather

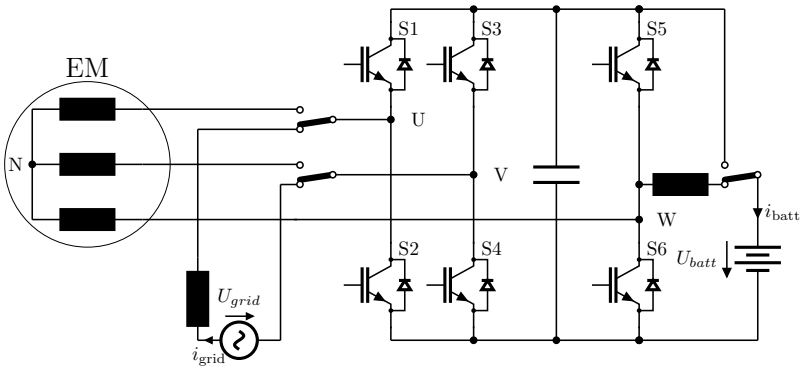

Figure 2.3: Single-phase inverter charger with boost-buck functionality.

heavy and expensive. Therefore, several integrated charging concepts that include the EM have been proposed in the past in an effort to eliminate the need for bulky and expensive inductors or a transformer, which should lead to weight and cost reduction. Different categories of how the EM is used in the charging process are reviewed in the next sections.

2.2 Three-phase EM

Many integrated chargers that have been reported by the industry [18–34] use a three-phase EM as a non-isolated boost PFC rectifier, buck converter, or buck-boost converter and can be categorized in the reconnection methods and utilization of the EM windings. The EM windings of the first three out of five concepts can either be connected to an energy source or to a sink. Common sources include AC or DC grids and the sink is typically the vehicle traction battery. If the EM windings of these three concepts are connected to a source, the DC link of the inverter is connected to the battery and hence, a boost PFC converter is created. Alternatively, it is possible to mirror these concepts by connecting the energy source to the DC side of the inverter and to connect the battery to one or more EM windings. Then, the motor drive circuit is operated as a buck converter. Many state of the art concepts are categorized in five common reconnection methods that are discussed in more detail in paragraphs 2.2.1 to

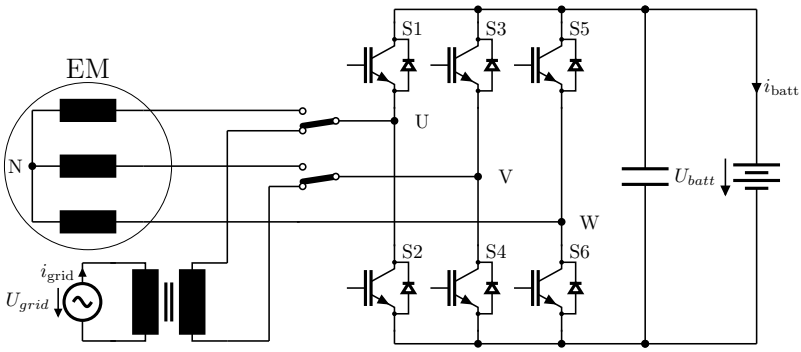

Figure 2.4: Single-phase isolated inverter charger.

2.2.5. Such systematic categorization has not been published before to this detail.

2.2.1 Y Concept

A common reconnection method is to reconnect one of the phase windings from the corresponding inverter leg to the line of a single-phase AC grid and to connect the available inverter leg to the neutral conductor of that grid. A classical example of the boost variant is the AC Propulsion concept [18], which is illustrated in Fig. 2.6. The main advantage of this topology is the high inductance thanks to the series connection of multiple machine phases as well as the possibility for bi-directional power transfer. Main disadvantages are the need for a reconnection switch rated for traction phase current and the unsymmetrical current distribution across the windings. An unsymmetrical current distribution could potentially generate shaft torque in case of an AC source, which might lead to wear on the brake system. This is especially true for a Permanent Magnet Synchronous Machine (PMSM) with a rotor position that is not aligned [19]. In contrast to alternating currents, a constant force is generated when using a DC current. The Y concept has been further developed in several variants. For example, an additional isolated DC/DC converter is added in [20]. Furthermore, a variant using a diode rectifier is patented in [21] and is discussed in [22]. This variant aims to eliminate the need for a reconnection switch, which

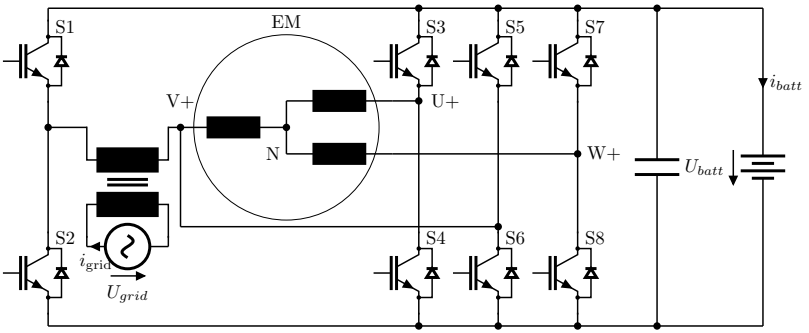

Figure 2.5: Single-phase isolated inverter charger with EM.

also eliminates the possibility for vehicle to grid energy transfer. Measured efficiencies of 93.1% are reported [22].

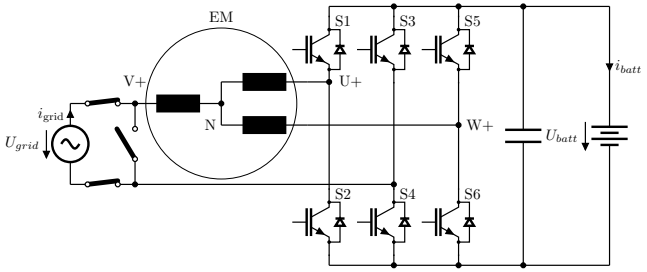

Figure 2.6: Y connected integrated charger with AC grid connection.

2.2.2 W Concept

An alternative connection method is to connect the EM neutral point N to an energy source, e.g. an AC grid, as shown in Fig. 2.7 and previously reported in [23–25]. Main advantages include the symmetrical current distribution, i.e. no shaft torque, and a smaller reconnection switch, which should be rated for charging or grid current only since the paths between the inverter legs and the EM phases are not interrupted during charging. Main drawbacks of this concept

include the need to provide access to the neutral point and the relatively small inductance due to the parallel connection of the machine windings as well as due to the zero sequence inductance. The effective inductance might be improved by introduction of interleaved switching [25]. In addition to these disadvantages, vehicle to grid energy transfer is not feasible if the W connection of the EM is operated as a boost PFC converter in combination with a passive diode rectifier.

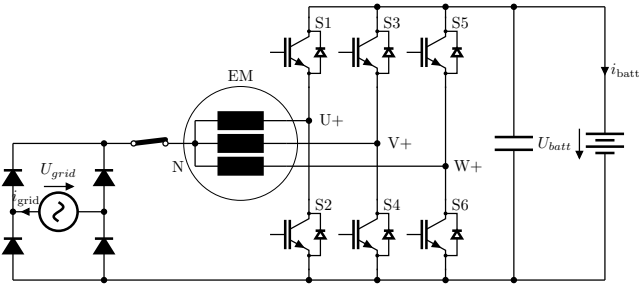

Figure 2.7: W connected integrated charger with AC grid and diode rectifier.

A variant to the classical boost PFC converter is published by Renault [26] and has been used in several generations of the Renault Zoe vehicles. In this setup, the e-drive is also used as a boost converter in W connection. However, to increase the battery flexibility range, a grid connected Current Source Inverter (CSI) is used as an additional step down converter. The drawback of this CSI based solution is that two parallel paths are required for bi-directional energy flow as the body diodes in an CSI are placed in series with the transistors instead of parallel to the transistors as in a Voltage Source Inverter (VSI). Furthermore, another solution is patented by Schneider Electric in [27] and is a mirror of the Renault concept: first, a dedicated VSI is used as a boost converter, then the e-drive is used as a buck converter with W connection to the battery. Another variant to the Zoe vehicles is also published by Renault in [28] and further integrates the wireless charging power transfer.

2.2.3 Open End Concept

Yet another connection possibility is to open the neutral point N by using three traction current rated switches and to reconnect each open end of the winding to one phase of a three-phase grid. The other end of the windings remains

connected to the inverter. This layout is proposed in [29], and is illustrated in Fig. 2.8. Although a three-phase grid can be connected with relatively large inductance, it comes at cost of shaft torque during charging at least for PMSMs and Induction Machine (IM)s. A version for an Electrically Excited Synchronous Machine (EESM) is published by Renault in [30] and proposes to cut off the rotor excitation to avoid any potential shaft torque. Facilitating access to the neutral point of the EM including the need for expensive switches rated up to traction currents is another drawback of the open end concept.

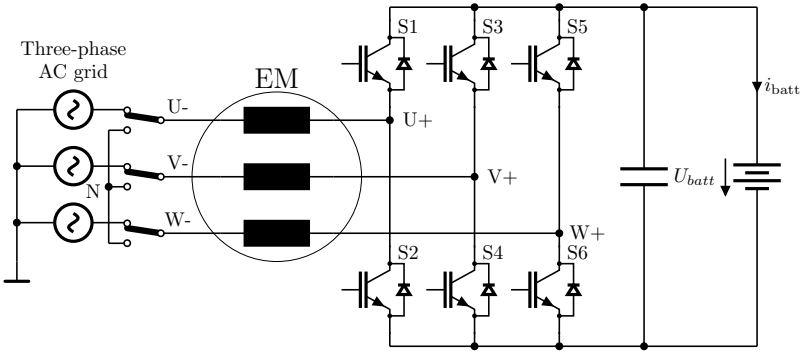

Figure 2.8: Open end connected integrated charger.

2.2.4 Separate Winding Connection

An alternative reconnection variant of the opened neutral point N is to reconnect each phase winding independently: two of the three EM phases can be connected to a single-phase AC grid, and the third EM winding can be connected between the inverter and the battery. Hence, the converter functions as a boost PFC converter with a series connected buck converter. This setup is published in [31] and illustrated in Fig. 2.9. This concept has as advantage that the battery voltage may be below the grid voltage since both AC/DC and DC/DC conversion steps are integrated into a three-phase e-drive. However, shaft torque due to unbalanced winding currents is a major drawback of this concept, as well as the need for expensive reconnection switches and contacts for accessing the EM neutral point.

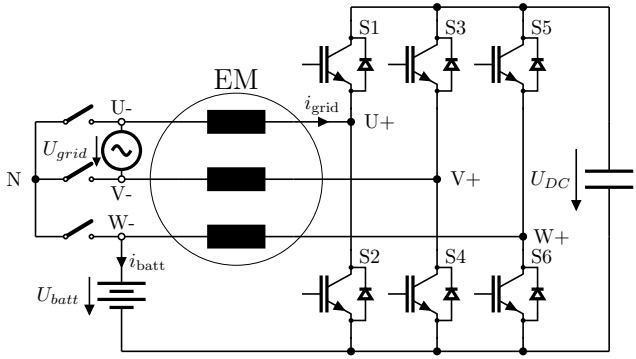

Figure 2.9: Split winding buck-boost integrated charger.

2.2.5 B4-B2 Connection

In contrast to opening and reconnecting one or more EM windings, it is also possible to open the inverter DC link and to keep the EM windings connected in original Y configuration between the inverter legs, e.g. as reported in [32] and shown in Fig. 2.10. Hence, the inverter functions as a buck-boost converter. Although this setup supports battery voltage levels below the grid voltage, it comes at the cost of needing a separate AC/DC converter for charging from AC grids and a switch rated for traction currents within the DC bus of the inverter.
A variant has been presented in [33, 34] and aims to eliminate the need of a dedicated AC/DC converter. However, drawbacks include the strong presence of the rectified grid component in the battery current and the limited efficiency, which is reported at a maximum of 89% [33]. Hence, a dedicated AC/DC converter is highly desired.

2.3 Multi EM concepts

In contrast to using one standard three-phase machine, some integrated charging concepts include multiple EMs in the charging process. Although multi EM charger concepts are more complex and require at least two e-drives to be available within the vehicle, main benefits include few required additional components and the absence of shaft torque.

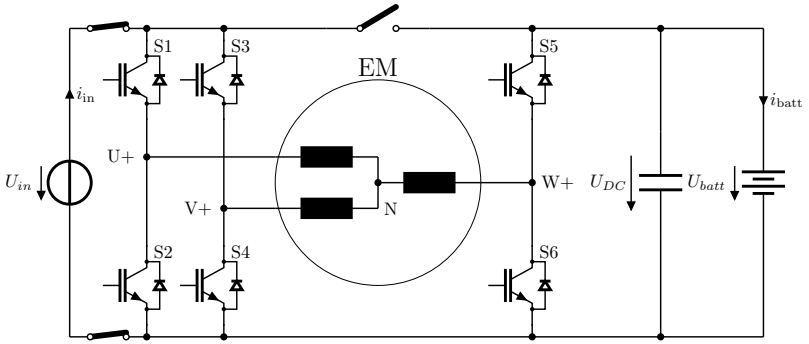

Figure 2.10: B4-B2 connected integrated charger.

An example of an integrated charger using two e-drives is the concept from Hyundai Motors [35, 36] and uses an auxiliary EM in addition to the traction EM. Both EMs are configured in W connection with accessible neutral points, to which a single-phase grid is connected. As a result, it is possible to use the system as a boost converter without generated torque. An overview of this is presented in Fig. 2.11. By using two e-drives, a bridge rectifier is no longer needed. As a result, bi-directional energy flow is provided. The machines may differ in design and/or size as the W connections provide balanced phase currents in each EM. A three-phase grid variant with two EMs in open end connection is presented in [37]. The main advantage over one standard three-phase EM in open end connection is the possibility to eliminate the shaft torque if two identical machines are used that are coupled in opposite direction on the same output shaft.
All solutions with two EMs provide only AC/DC boost functionality with PFC. Hence, a dedicated DC/DC converter is required for voltage step down.
Another concept has been proposed by Daewoo Heavy Industries LTD. in [38, 39] and uses four EMs of a Four Wheel Drive (4WD) vehicle. Similar to the Hyundai concept, all EMs have an accessible neutral point. Two EMs are used as a boost converter. Moreover, the two remaining EMs are used in parallel as a step down converter. This concept is illustrated in Fig. 2.12. An advantage of this concept over the concepts with two EMs is that both step up and step down functionality are provided without the need for a separate DC/DC converter. Moreover, only one switch is required to reconnect the battery from the positive

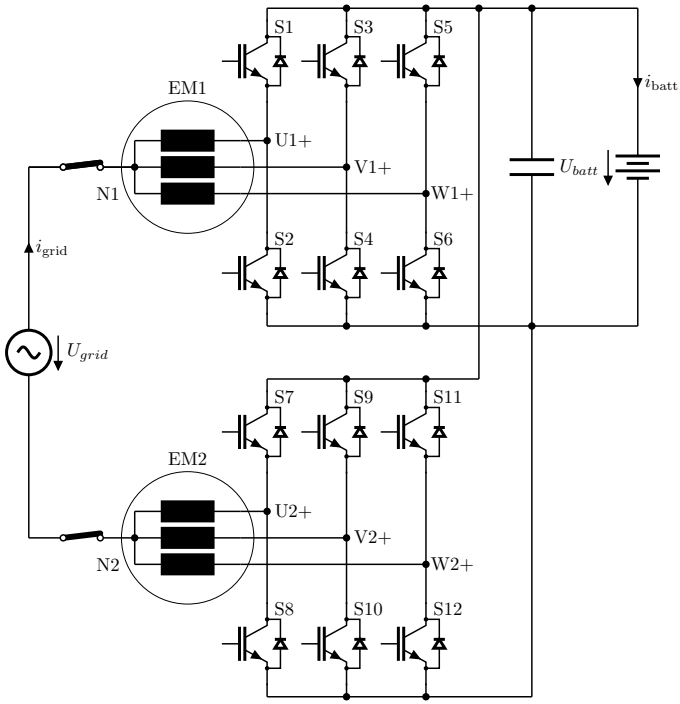

Figure 2.11: Integrated charger with two EMs as boost converter.

DC bus terminal to the neutral point of EM 3 and 4. The main drawback is of course the limited application of this concept, as most vehicles do not contain four e-drives. Even for heavier vehicles that are equipped with four e-drives, it is questionable if single-phase charging can provide sufficient power.

2.4 Multi-phase EM Concepts

In contrast to using one or multiple three-phase machines, it is possible to arrange a special winding variant within one EM: a multi-phase EM with at least five phases. Multi-phase machines can be used as inductances or as a transformer, since the different winding sets of a multi-phase EM can

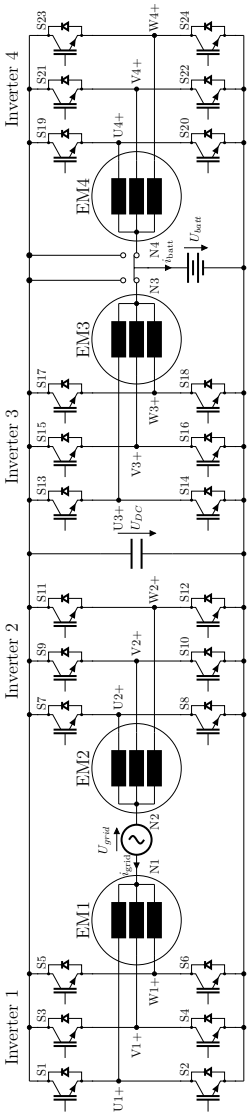

Figure 2.12: Integrated charger for a four wheel drive system.

be galvanically isolated from each other by introduction of multiple neutral points. Multi-phase EMs that are used as inductances for integrated charging are discussed in paragraph 2.4.1. Thereafter, multi-phase machines used as a transformer in the power conversion process are reported in paragraph 2.4.2.

2.4.1 Multi-phase EM as inductances

As aforementioned, multi-phase EMs can be used as inductance for the charging process. Typically, multi-phase machines are then directly connected to a three-phase grid. A topology is proposed by Valeo [40–43] and uses a six-phase EM with a center tap winding connected to a 3xH bridge inverter. It is possible to carry out the center point of the winding and use the two windings per phase as a boost converter as shown in Fig. 2.13. No Magneto Motive Force (MMF) is developed as a result of the identical currents in opposite direction through each pair of phase windings and thus, no shaft torque is generated. A variant with single-phase grid connection is presented in [43]. Moreover, three out of the twelve switches can be saved by using the presented nine switch converter [44]. A variant including a twelve-phase machine with redundancy for traction is presented in [45]. Only step up conversion is feasible for all variants. The HV DC/DC converter might be included for step down functionality if available [40], which is illustrated by transistors S13 and S14 and the battery connected inductor in Fig. 2.13. This concept can be used with different machine types, including the PMSM, the EESM, and the IM. Furthermore, a variant for a Switched Reluctance Machine (SRM) has been proposed in [46]. In addition, a single-phase integrated charger based on a SRM has been presented in [47]. There, two out of three phases are operated as a boost PFC converter. Moreover, the third phase is utilized as a step down converter, which could be a benefit in comparison to the other concepts that still need a separate DC/DC converter for step down conversion.
Alternative topologies of using multi-phase EMs as inductors for integrated chargers are proposed in [48–50]. There, several concepts are presented and mainly the concepts with five- and nine-phase machines are further investigated. The nine-phase concept is most promising as three neutral points of three separate three-phase winding sets are available for W connections. Therefore, these can be connected to a single- or three-phase grid each with symmetrical winding currents. An example is illustrated in Fig. 2.14 for a nine-phase EM connected to a three-phase grid. Single-phase grid connections for five- and six-phase machines are proposed in [48] and also use the EM neutral points. A major advantage of all variants is that no torque is generated unless a

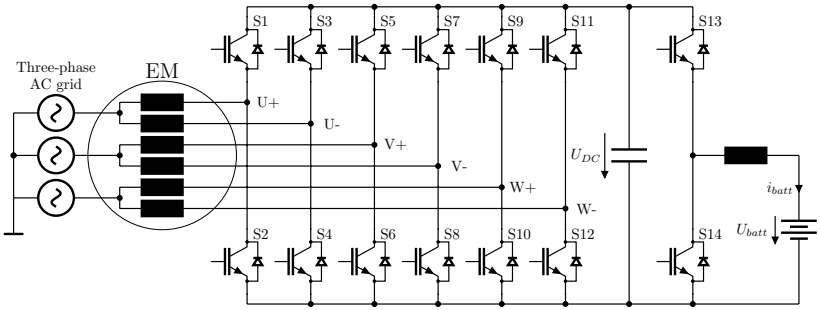

Figure 2.13: Integrated charger using a six-phase EM with center tapped windings.

Fractional Slot Concentrated Winding (FSCW) PMSM is used [51]. For these machine configurations, a control strategy is reported in [51] to reduce the torque produced by the spatial harmonics and to keep the rotor shaft at stand still. Another advantage is that high efficiency is possible: measured efficiency levels above 90% are reported [52]. However, the system is rather complex and voltage step down is only available if a dedicated DC/DC converter is in place as shown in Fig. 2.14.

2.4.2 Multi-phase EM as transformer

In contrast to using the EM as a non-isolated inductor in the charging process, it is possible to use a multi-phase EM as an isolation transformer. Several integrated charging concepts using the EM as a transformer have been presented in the past. An integrated propulsion and charging system for a fork lift truck has been reported in [53] and is presented in Fig. 2.15. In this concept, a Wound Rotor Induction Machine (WRIM) is used as a step down transformer for 48 V battery charging during charging mode. One end of the rotor windings is separated via slip rings and contactors and are connected to a three-phase grid. The stator windings remain connected to the inverter. A mechanical lock is required to avoid shaft rotation during the charging process. The efficiency is highly dependent on the length of the air gap between stator and rotor, which determines the required magnetization current. Due to the direct grid connection of 50 Hz and a typical large air gap, this current is relatively large and has thus a significant impact on the efficiency [10, 56].

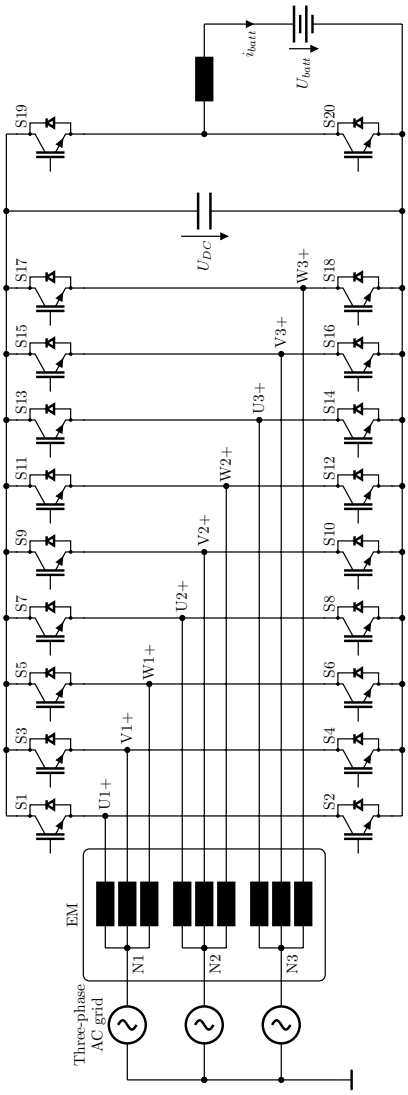

Figure 2.14: Integrated charger using a nine-phase EM with three neutral points.

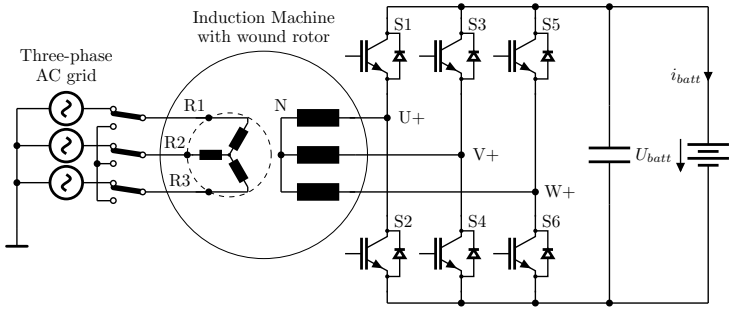

Figure 2.15: Integrated charger with WRIM as transformer.

Another concept is introduced in [54, 55] and also uses the EM as a transformer. In this reference, the EM is not used for a charging application. Instead, additional windings with a 1:n winding ratio are placed in the stator slots and the concept is used as an auxiliary DC/DC converter from the 400 V HV battery to the 12 V bus while still providing traction to the wheels. Some space is required for the additional windings, reducing the torque density of the original EM. The additional windings are all connected in series to form the secondary side of the transformer. The regular three-phase winding of the EM is used as a primary transformer winding. The concept is shown in Fig. 2.16. Although predicted efficiency levels from DC to DC of 80% are claimed for a synchronous machine used for traction [55], measured efficiencies of only 30% are reported [55] for a smaller machine. In addition to the integration of the board net DC/DC converter, this concept could in theory also operate as an HV grid isolated integrated charger when an extra AC/DC converter is used. Note that the winding ratio n should then be changed to match the grid and battery voltages. A clutch is required to decouple the rotor shaft from the wheels during charging. Single- and/or three-phase grid outlets are feasible, dependent on the AC/DC converter layout.

A third method for integrated charging with galvanic isolation is presented in [56–59]. A PMSM with two stator winding sets is used as a rotating transformer during charging. Shaft rotation is crucial to eliminate the need for high magnetization currents with resulting low efficiency for PMSMs. An advanced reconnection device with 12 contacts all rated up to traction current is needed to reconnect three of the six windings from the inverter to a three-

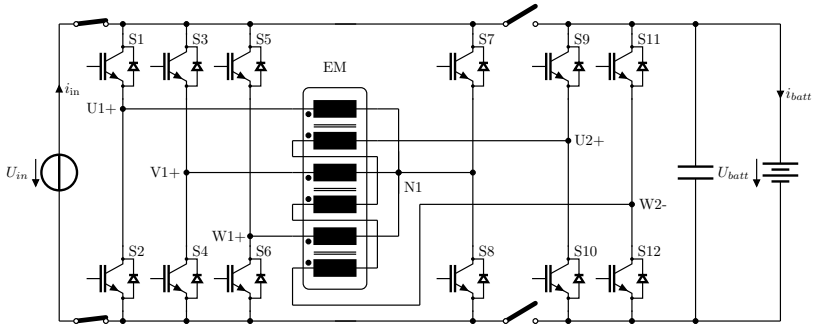

Figure 2.16: Isolated DC/DC converter with EM as transformer.

phase grid [58]. Star-delta connection is provided for reduced winding voltages at the inverter side in order to avoid the need for a separate DC/DC converter for voltage step down. A medium-high efficiency can be achieved, although measured levels up to 80% are reported [57, 59]. Moreover, it comes at the cost of shaft rotation and corresponding mechanical losses. As a consequence of the shaft rotation, a clutch between the rotor shaft and the wheels is required to avoid vehicle motion. Since not all BEV might be equipped with such a clutch, integrated charging concepts that generate shaft rotation are highly undesired for those vehicles. The concept is shown in Fig. 2.17 with the windings configured for charging mode, the reconnection device is not shown. A variant with a nine-phase EM connected to a six-phase inverter has been proposed in [60] and aims to reduce the harmonic content as a result of the harmonic filtering thanks to the special winding arrangement.

2.5 DC/DC converter

In contrast to using the e-drive in the charging process, some integrated charger concepts involve the DC/DC converter. BEV contain a LV DC/DC converter to supply energy from the HV battery to the e.g. 12 V board net of the vehicle with its auxiliaries. As stated in [65], any LV, i.e. DC voltages below 60 V, shall be galvanically isolated from any voltage above 60 V DC. Hence, the board net has to be galvanically isolated from the HV battery if this HV battery is above 60 V DC. Therefore, galvanic isolation is also required between the LV battery

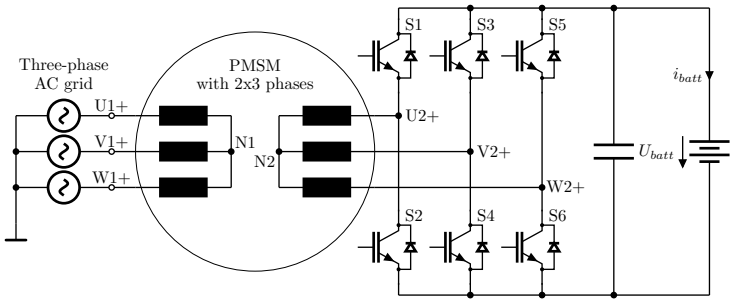

Figure 2.17: Integrated charger with PMSM as rotating transformer.

and the grid connection. Thus, a galvanically isolated charger could integrate LV DC/DC conversion as well in order to supply the board net. In contrast, a non-isolated charger may only charge HV batteries.
In addition to the LV DC/DC converter, some BEV are equipped with an HV DC/DC converter between battery and powertrain to compensate for the fluctuating battery voltage. It is feasible to add non-isolated charging functionality to this HV DC/DC converter, as both the HV battery and the HV bus side of this converter are galvanically isolated from the LV board net. A solution for this is presented in [61] and shown in Fig. 2.18. Although five diodes and five transistors are required, only one inductor is required to provide boost and bidirectional DC/DC energy transfer between the HV battery and the HV bus. Moreover, charging functionality from a single-phase AC grid is provided with the addition of only a diode bridge rectifier, i.e. diodes D7 - D10, and the transistor Q1.
In addition to utilization of the HV DC/DC converter, it is possible to integrate the battery charger with the LV DC/DC converter used for the board net, as long as galvanic isolation between the HV side, including the grid, and the LV board net is offered. An option that does not provide galvanic isolation between the grid and the HV battery is described in [62] and is shown in Fig. 2.19. In principle, charging functionality is integrated in the HV circuit of a LV DC/DC converter. This converter is built as a LCL resonant tank with a step down transformer. This tank is opened in charging mode. Furthermore, a second 0.5 kW LV DC/DC converter is added for supply to the board net during charging. The maximum charging power is limited by that of the main LV DC/DC converter, which is with typically around 3 kW significantly less

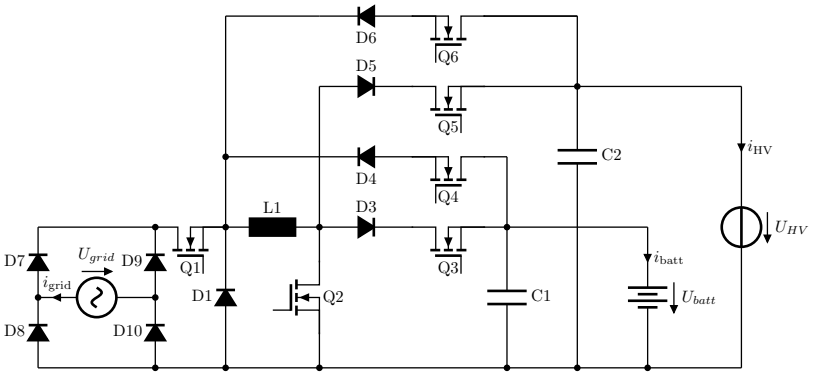

Figure 2.18: Non-isolated integrated charger using HV DC/DC converter.

than that of the e-drive and also below most desired charging power levels. Additional components include seven diodes, five transistors, three inductors, and one mechanical switch to open the resonant tank. Both boost and buck functionality are feasible and measured efficiency levels of 97% are reported [62] for charging.

Finally, a last concept is presented in [63, 64] and shown in Fig. 2.20. In this concept, a 2x3 phase e-drive is operated as a grid connected boost PFC converter in W connection. In addition to this boost functionality realized by the e-drive, the transformer of a LV DC/DC converter is equipped with a secondary HV winding and provides galvanic isolation as well as step down functionality for the battery voltage. Similar to the previous concept, the maximum charging power is in this concept also limited by the LV DC/DC converter power. More precisely, it equals 50% of the DC/DC converter power minus any power flowing to the LV circuit. The EM rotor shaft does not generate torque during charging, thanks to the balanced winding currents. Furthermore, four switches, an active full bridge, and a second high voltage winding for the DC/DC converter are among the required additional components for this concept. Both boost and buck functionality are also for this concept feasible and measured efficiencies up to 92.8% are reported [63].

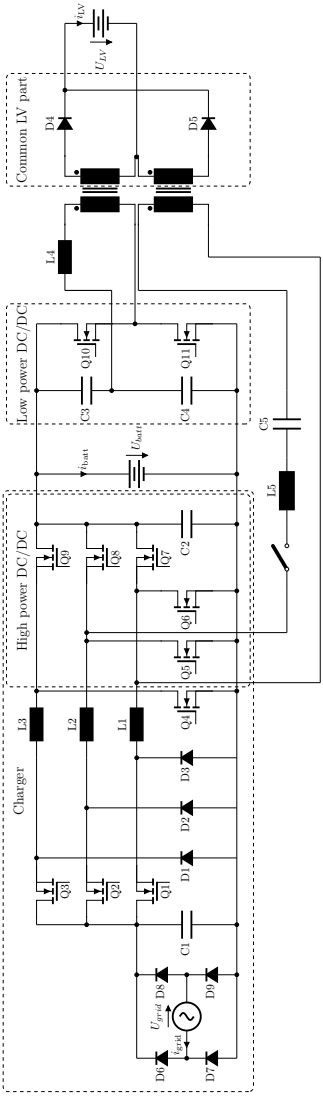

Figure 2.19: Non-isolated integrated charger using LV DC/DC converter.

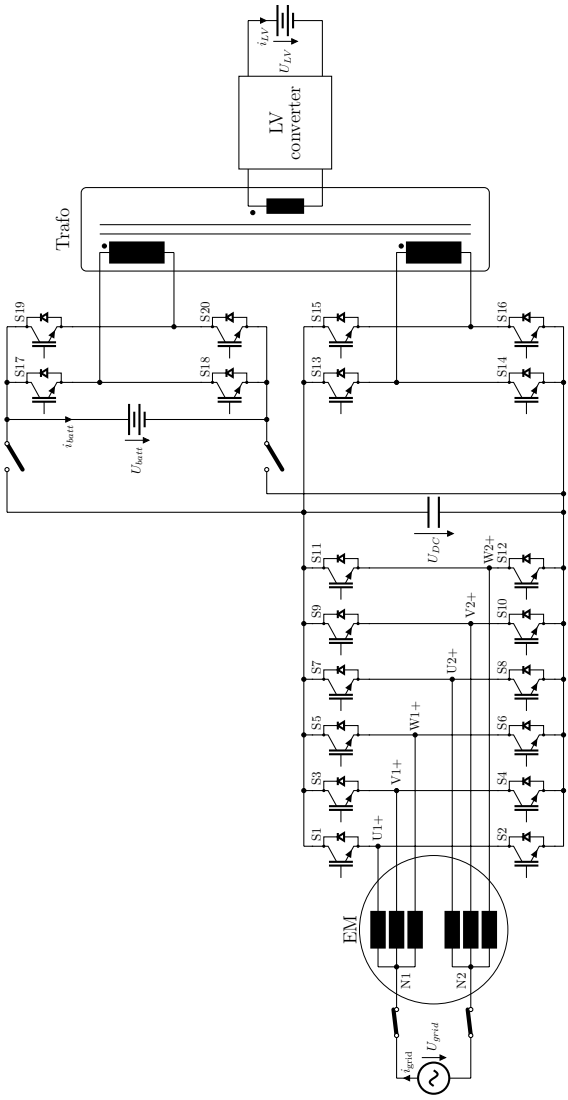

Figure 2.20: Isolated integrated charger using LV DC/DC converter and e-drive.

2.6 Comparison of integrated chargers

An overview of the different discussed integrated charger types is provided in Tab. 2.1 by categorizing into the method of EM use. In addition, the EM specific attributes are listed in Tab. 2.2. Furthermore, the key advantages and drawbacks of the different base types of integrated chargers are presented in Tab. 2.3.
As mentioned before, battery chargers require both step up and step down functionality to accommodate a wide battery voltage range. Most of the state of the art concepts using a three-phase EM are not able to perform both steps, unless expensive reconnection switches are required in combination with an AC/DC converter or generated shaft torque. Moreover, even most multi-phase concepts provide either step up or step down functionality, not both. The only exception to this are charging concepts using a 2x3 phase EM as a transformer. Although conceptually possible, there is a trade-off between efficiency and shaft rotation. High efficiency is key and shaft rotation during charging is undesired as it requires a clutch between the EM shaft and wheels in order to avoid vehicle movement, which is not standard present in many BEV due to their fixed gear ratio.
For non-isolated multi-phase EM integrated charging concepts, a separate HV DC/DC converter is required for boost and buck functionality. In contrast, concepts that involve multiple machines and/or the HV DC/DC converter could provide both step up and step down functionality. However, a drawback is that not every vehicle contains more than one EM or a HV DC/DC converter, making these concepts applicable for a smaller selection of vehicles only. Finally, including the LV DC/DC converter in the charging process is not preferred as it tends to be designed for significantly lower power levels than the desired charging power.
As a result from all the disadvantages as described above and summarized in Tab. 2.3, there is still a need for improved integrated charging concepts that provide boost and buck functionality in the drivetrain while providing high efficiency without shaft torque or expensive additional components. Therefore, novel concepts using multi-phase e-drives as voltage step up and step down converter are introduced in this thesis as these provide more flexibility for winding reconnection arrangements. A concept that uses the EM as a transformer in an isolated HV DC/DC converter during charging is reviewed in terms of efficiency and cost in chapter 3. Moreover, a method for integration of the LV DC/DC converter is also introduced there. In addition to the isolated concept, a novel non-isolated integrated charger concept with two reconnection variants is derived from state of the art concepts in chapter 5 and aims to

provide low cost high efficient integrated charging while providing boost and buck functionality.

Concept	Grid type	Isolation	Function	Components
Inverter only (2.1)	single-phase three-phase	optional	boost PFC	transformer inductor switch
Y (2.2.1)	single-phase	no	boost PFC	switch
W (2.2.2)	single-phase	no	boost PFC	diode rectifier
Open end (2.2.3)	three-phase	no	boost PFC	switch (3x)
Separate (2.2.4)	single-phase	no	boost PFC, buck	switch (3x)
B4-B2 (2.2.5)	DC	no	buck-boost	PFC rectifier, switch
Multi EM (2.3)	single-phase	no	boost PFC and/or buck	switches
Multi-phase EM as inductors (2.4.1)	single-phase three-phase	no	boost PFC and/or buck	switches
EM as transformer at standstill (2.4.2)	three-phase or DC	yes	buck-boost	mechanical brake
EM as rotating transformer (2.4.2)	three-phase	yes	buck-boost	clutch switches
HV DC/DC converter (2.5)	single-phase	no	boost PFC and buck	transistor, diode rectifier
LV DC/DC converter (2.5)	single-phase	no	boost PFC, buck	diodes switches inductor
LV DC/DC converter with EM (2.5)	single-phase	yes	boost PFC and buck	switches, trafo winding, full bridge

Table 2.1: Key parameters of different integrated charger concepts.

Concept	**Powertrain utilization**	**EM type**	**Shaft torque**
Inverter only (2.1)	low	n.a.	no
Y (2.2.1)	high	PMSM, IM, EESM	possible
W (2.2.2)	high	PMSM, IM, EESM	no
Open end (2.2.3)	high	PMSM, IM, EESM	yes
Separate (2.2.4)	high	PMSM, IM, EESM	yes
B4-B2 (2.2.5)	high	PMSM, IM, EESM	no
Multi EM (2.3)	high	all	no
Multi-phase EM as inductors (2.4.1)	high	all	no
EM as transformer at standstill (2.4.2)	high	WRIM	yes
EM as rotating transformer (2.4.2)	high	PMSM	yes
HV DC/DC converter (2.5)	medium	n.a.	no
LV DC/DC converter (2.5)	medium	n.a.	no
LV DC/DC converter with EM (2.5)	high	PMSM, IM, EESM	no

Table 2.2: Powertrain specific parameters of different integrated charger concepts.

Concept	**Advantages**	**Disadvantages**
Inverter only (2.1)	high power high efficiency	separate inductors
Three-phase EM (2.2)	high power high efficiency	only boost or buck or reconnection switches and torque or AC/DC converter
Multi EM (2.3)	high power high efficiency	four EMs needed for boost and buck
Multi-phase EM as inductors (2.4.1)	high power high efficiency three-phase grid possible	only boost
EM as transformer (2.4.2)	high power LV DC/DC integration	low efficiency or shaft torque
HV DC/DC converter (2.5)	high power voltage flexibility high efficiency	HV DC/DC converter not always available
LV DC/DC converter (2.5)	voltage flexibility high efficiency	low power

Table 2.3: Pros and cons of different integrated charger types.

3

A Galvanically Isolated Integrated Charger

A new isolated integrated charger concept using the EM as a transformer at standstill was available from previous work at Bosch by means of a filed patent application [66] and a brief introduction [S1]. This chapter starts with a more detailed introduction of this isolated charger concept by deriving state of the art concepts from paragraph 2.4.2 with the aim to improve the efficiency of isolated integrated charging at rotor standstill. Afterwards, the system efficiency based on the EM and semiconductor losses is analyzed using simulations. Furthermore, a novel method for efficiency improvements as filed with a patent application in [E5] is introduced and reviewed. Moreover, the previous work [66, S1] from Bosch is further extended with additional functionality integration of the LV DC/DC converter for the 12 V board net as filed in a patent [E6]. Finally, a cost analysis and motivation to focus on non-isolated integrated chargers is presented. A summary of the work reported in this chapter has also been presented in [E1, E4].

3.1 Concept Introduction

As discussed before, the main drawback of the galvanically isolated integrated charging concepts reported in paragraph 2.4.2 is the trade-off between low

efficiency and shaft rotation when the EM is used a transformer. Since the rotor normally responds with movement to alternating fields, the key is to find a rotor that can be deactivated, i.e. a rotor that does not respond to alternating fields during charging operation. Note that the rotor should not be removed since its iron core is a vital part of the flux path during charging.

3.1.1 Rotor Deactivation

Permanent magnet rotors are unsuitable to function as a transformer at standstill due to the inability to deactivate their permanent magnet fields. Hence, alternative machine types have to be investigated. IMs and EESMs may be used if the current path in the rotor can be interrupted in charging mode. This is because normally a current flows through the rotor, either induced by the stator fields in an IM or generated by a separate source in an EESM, which creates a force when a rotating stator field is applied. For both IMs and EESMs, these currents can be interrupted by placing switches in the rotor current paths, which is illustrated for an IM in Fig. 3.1. Hence, it is possible to avoid reaction of the rotor to stator fields without losing the rotor core as part of the transformer flux paths in charging operation.

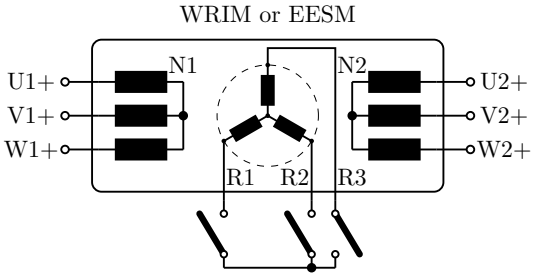

Figure 3.1: Rotor deactivation method.

These switches can either be implemented with slip rings, or with power electronics integrated onto the rotor. Both have the drawback that the switches need to withstand the full rotor currents and the maximum rotational speed in traction mode, which makes the implementation rather costly. Furthermore, a wound rotor might be preferred as electrical contact between the rotor bars of a squirrel cage rotor and the rotor steel may lead to additional losses and

shaft torque during charging. Electrical connection between rotor bars e.g. via the steel laminations should be avoided in this concept in order to prevent shaft torque. An example of such contact created in the production process is illustrated in Fig. 3.2. In this sample, liquid copper was poured into the rotor slots to form the rotor bars. A meltdown of the rotor steel occurred due to the high temperatures of the copper. It is uncertain if this electrical contact can be avoided due to the nature of the production process of squirrel cage rotors. Therefore, it might be useful to use a wound rotor instead, since those windings can easier be isolated from the rotor slots than the bars of a squirrel cage rotor. Even though a wound rotor might be preferred, the efficiency analysis is performed for a squirrel cage rotor as this EM layout was readily available.

Figure 3.2: Electrical contact between steel and copper bars formed during production.

3.1.2 Transformer Frequency

Another key method to enhance the efficiency of the EM as a transformer at standstill is to increase the frequency of the energy transfer. A 50 Hz field has a relatively high magnetization current I_M as illustrated in Fig. 3.3. Magnetization currents are frequency dependent extra currents that are required to magnetize the air gap and to facilitate power transfer. These currents lead to additional EM and inverter losses and should thus be minimized, which is achieved by

increasing the frequency of power transfer. On the other hand, the maximum power transfer for a given DC voltage is also limited by the frequency due to the frequency dependent inductive reactance. For this EM and 11 kW of energy transfer at a DC voltage of 600 V, the maximum operating frequency is 400 Hz since the induced secondary voltages are above the set 300 V primary peak voltages for frequencies above 400 Hz. This leads to a 180° phase shift in the secondary currents, which results in opposite power flow. Hence, it is preferred to operate the transformer somewhere between 50 and 400 Hz. The optimal operation frequency value will be investigated in paragraph 3.2.

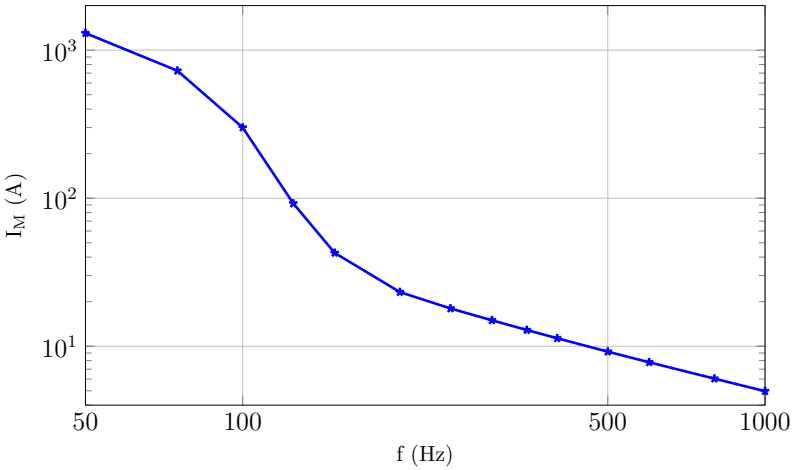

Figure 3.3: Magnetization current as function of frequency for the analyzed IM.

3.1.3 System Topology

Since the optimal transformer frequency is above the grid frequency, it is recommended to decouple the transformer from the grid. This can be achieved by use of a 2x3-phase e-drive with two VSIs as filed in patent application [66] and shown in Fig. 3.4. In traction mode, both inverters are connected to the battery. In charging mode, one of both inverters is disconnected from the battery and should be used for creation of the higher frequent AC currents in the primary transformer windings instead of creating a direct connection of these windings to

the 50 Hz grid. A dedicated AC/DC converter can be connected to this inverter to enable charging from AC grids, as is shown in Fig. 3.5. A variant of this concept with the AC/DC converter placed in the offboard infrastructure instead of onboard the vehicle is presented in [S1].

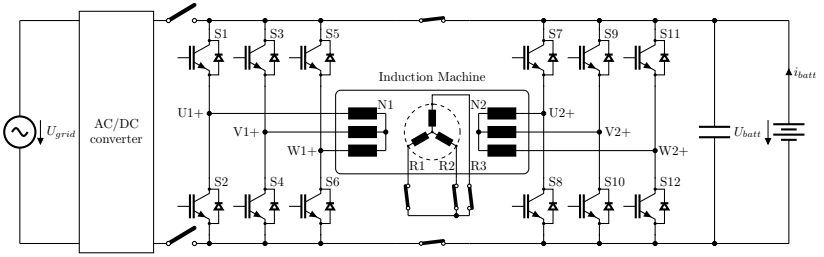

Figure 3.4: 2x3-phase e-drive in traction mode.

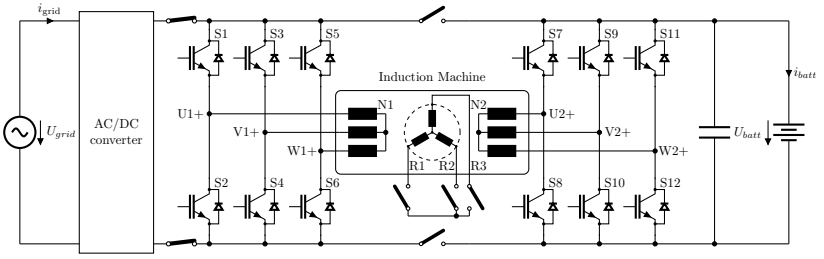

Figure 3.5: 2x3-phase e-drive used as a transformer at standstill for charging.

3.2 Losses and Efficiency Analysis

The efficiency η of the isolated DC/DC converter part of the integrated charging system is analyzed in this section. Two Dimensional (2D) Finite Element Method (FEM) simulations are used for calculation of the transformer losses. In addition, the losses of the VSIs are reported. The grid connected AC/DC converter is not reviewed as it is a state of the art dedicated converter. A 4-pole, 153 kW, 15,000 rpm, and 287 Nm Squirrel Cage Induction Machine (SCIM)

with phase resistances of 103 mΩ and a base speed frequency of 171 Hz is used for all analyses. Moreover, this EM has a 0.7 mm air gap. Both classical ohmic copper and iron losses are reviewed for a 11 kW, 600 V battery charger with the primary EM phase voltage defined at 300 V peak. More detailed specifications of this EM are presented in chapter 4.

3.2.1 Transformer Efficiency

The Bosch in-house FEM tool Edyson was used for the investigation of the power transfer capabilities and the iron losses. Edyson is similar to the commercial tool JMAG. A co-simulation with Matlab was established for correct load simulation since the FEM tool does not incorporate any electrical loads [S2]. During this co-simulation, the magnetization current is calculated using the FEM tool. Once in steady state, the secondary current is calculated based on the secondary side open circuit voltage and a predefined load representing the charging power. This current will then be led back to the FEM tool and a new induced voltage in the secondary windings will be calculated. Thereafter, a new load current will be calculated and led back to the FEM tool. This process will continue in several iterations until steady state is reached for the desired load condition and is repeated for each frequency of the energy transfer. Eventually, the copper and iron losses are provided by the FEM tool.
The iron losses are calculated with FEM and are based on the Jordan loss separation method with the losses split into hysteresis and eddy current components:

$$P_{\mathrm{Fe}} = P_{\mathrm{hys}} + P_{\mathrm{eddy}} = K_{\mathrm{h}} f^{\alpha} B^{\beta} + K_{\mathrm{e}} f^{\gamma} B^{\delta}. \tag{3.1}$$

A safety factor of 1.5 is used to obtain a realistic overview of the actual iron losses. This factor is based on empirical analysis from EM experts and is used to compensate for the additional iron losses due to the material cutting techniques as the material parameters in (3.1) only reflect raw material values without processing damage. The primary and secondary voltages and currents in steady state are plotted in Fig. 3.6 for one phase for a frequency of 300 Hz.
Ideal sinusoidal voltages and currents are used for the loss analysis to shorten the duration of the FEM calculations. Hence, any potential additional iron and copper losses due to the switching ripple are not considered for this charger concept. Moreover, extra copper losses due to the skin effect, the proximity effect, and due to circulating currents are neglected. These assumptions are

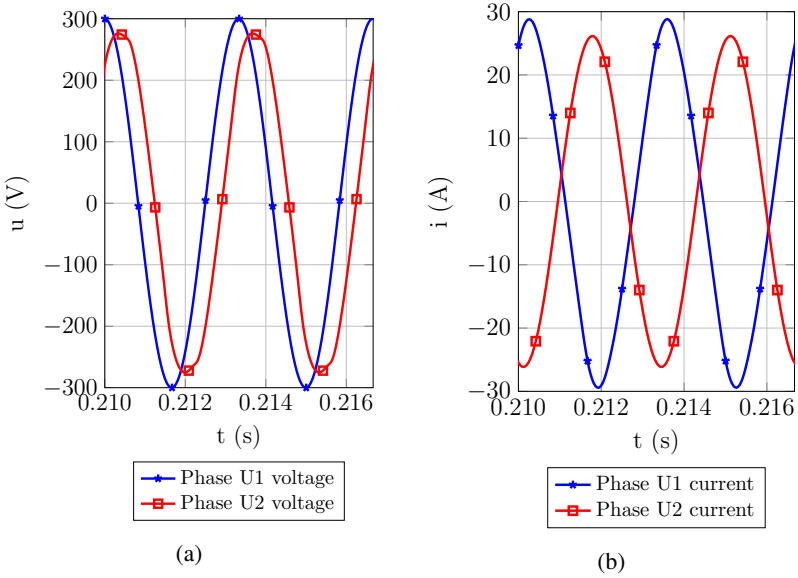

Figure 3.6: Phase U primary and secondary (a) voltages and (b) currents.

made to provide a first estimation of the upper level of the achievable efficiency with this charger concept. More detailed calculations including these effects are only useful if the efficiency is promising enough to further analyze the isolated charger concept.
The calculated copper and iron losses are shown in Fig. 3.7 for various frequencies. The transformer efficiency is plotted in Fig. 3.8 for various operating frequencies. The iron losses are dominant. Note that both the iron and the copper losses decrease at increased frequencies as a result of a reduction in the magnetization current.

3.2.2 System Efficiency

In addition to the transformer losses created by the IM, there are losses in the inverters that are reviewed in this paragraph. Therefore, loss maps of the inverter Insulated Gate Bipolar Transistor (IGBT) and diode switching losses based on the Semikron SKAI2 1200 V / 450 A VSIs are used for a switching frequency

of 15 kHz. These loss maps have been measured using a double pulse test method, which is explained in more detail in section 4.4. Furthermore, the inverter conduction losses are calculated using the datasheet values that are also elaborated in section 4.4. The optional grid connected AC/DC converter is not included in the loss analysis. All other system losses P_{loss} are listed in Fig. 3.7.

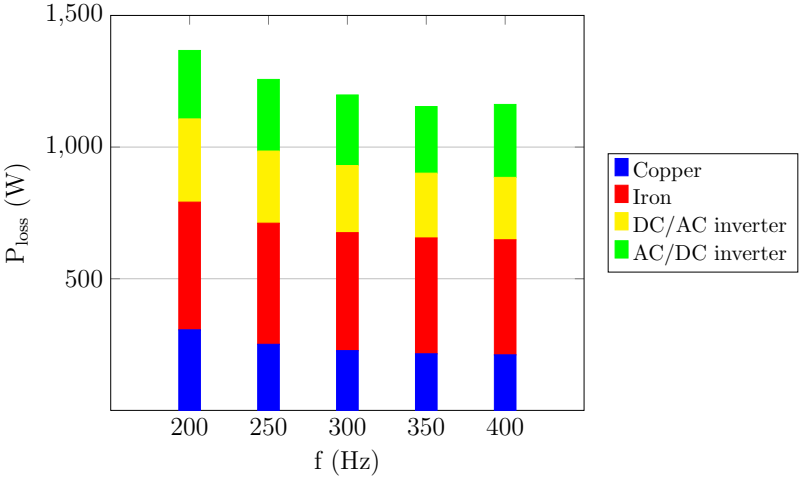

Figure 3.7: Calculated system losses for various frequencies.

Based on all previously described loss effects, the combined efficiency from DC to DC is 87% at 200 Hz and is increased to 89% at 400 Hz as shown in Fig. 3.8. Even if a highly optimized AC/DC converter with a 99% efficiency such as [67] would have been used, a total efficiency of only 88% from AC grid to battery would be achieved at 400 Hz. Although inverters with improved efficiency could be used, for example using SiC devices, the overall efficiency remains significantly lower than that of dedicated onboard chargers, which have reported efficiency levels up to 94% [3]. The main reason for this gap in system efficiency is the relatively low efficiency of the selected IM as transformer with a maximum of 94%.

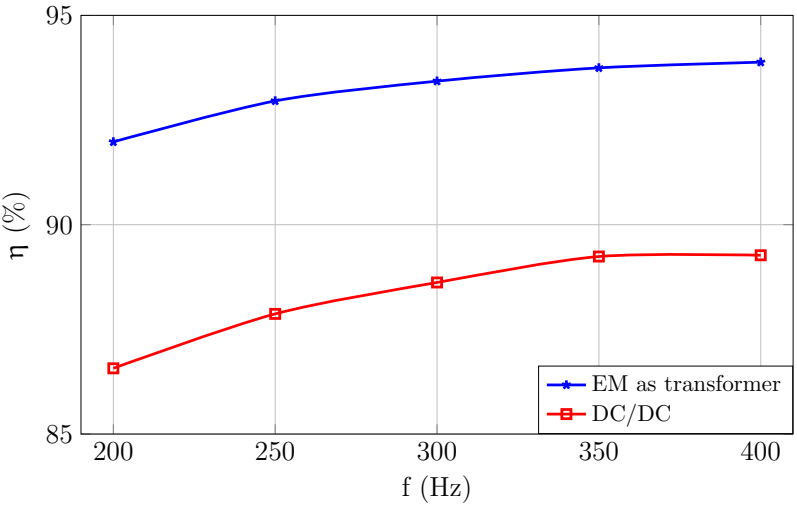

Figure 3.8: Calculated efficiency for various frequencies.

3.2.3 Transformer Efficiency Improvements

A method of efficiency enhancements based on layout changes that reflect a better coupling factor between the primary and secondary winding sets is introduced and reviewed. Therefore, an alternative winding layout is proposed, in which each stator slot carries a primary and a secondary winding instead of only one winding. The standard and improved layouts are shown in Fig. 3.9 (a) and Fig. 3.9 (b) respectively. The goal of this advanced winding layout is to enhance the transformer efficiency by means of an improved coupling factor. The efficiency and coupling factor improvements are analyzed with FEM and are presented in Fig. 3.10 and Fig. 3.11 respectively. Although it might be possible to utilize the introduced winding layout in charging mode, it is preferred for optimized traction capabilities to carry only one winding per slot and to utilize the phase shift between the slots for extra peak torque and lower torque ripple. In such a case, a winding reconnection device is proposed to alternate between the two layouts in charging and traction mode. An extra patent has been filed for this reconnection method [E5]. With efficiency improvements up to 0.5%, it is questionable if the extra cost for reconnection hardware is

worthwhile. Dependent on the EM design, the efficiency difference might be larger.

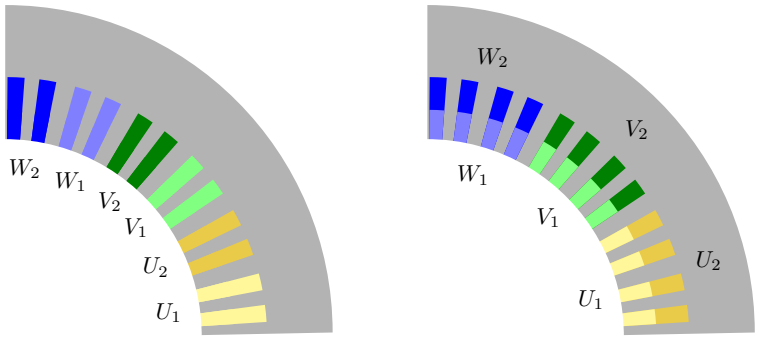

Figure 3.9: EM cross section with (a) standard and (b) novel winding arrangement.

3.3 LV DC/DC Converter Integration

As mentioned in chapter 2, galvanically isolated integrated chargers may include power transfer between the HV bus and the LV board net. Hence, it is possible to extend the analyzed isolated charger concept with additional windings for auxiliary loads connected to the 24 V bus, in a similar way as the concept introduced in [55]. The resulting combined integrated charger and LV DC/DC converter is illustrated in Fig. 3.12. A patent application has been filed [E6].
The analyzed winding placement for the combined charger and LV DC/DC converter is shown in Fig. 3.13. Although conceptually possible, the integration of these extra windings implies that some of the peak power is used to supply the board net and can thus not be used for traction. As a result, a peak traction performance reduction of the EM of approximately 4% is calculated [S3]. Therefore, an additional 4% of active EM volume has to be added to compensate for the reduced peak torque and power output, assuming that the shear stress of the selected IM and thus the torque and power density should not further be increased to respect the material stress limits. With an active volume of 4.58 L, an additional 0.2 L is required to implement the DC/DC transformer

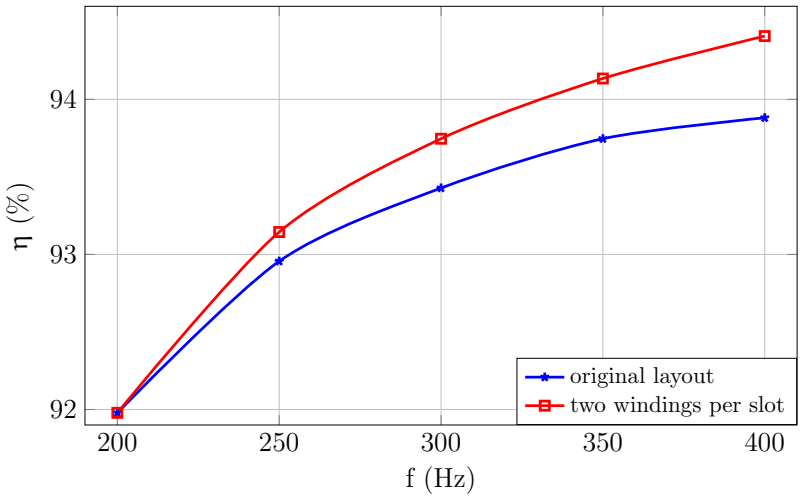

Figure 3.10: Transformer efficiency for standard and improved layout.

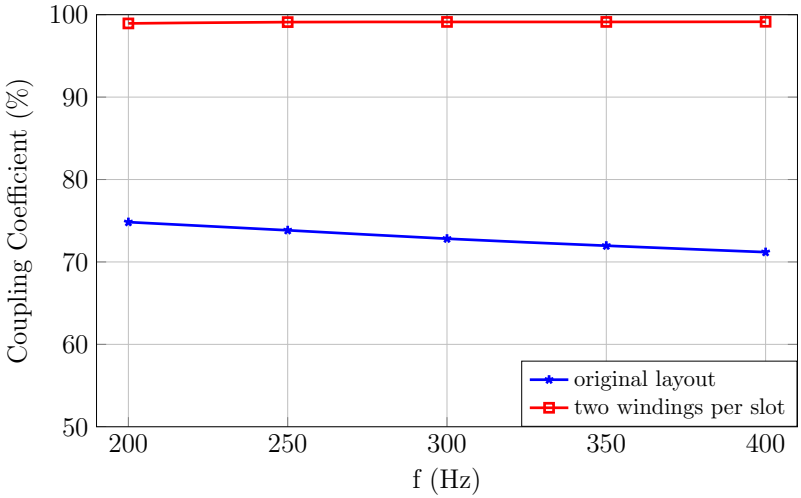

Figure 3.11: Coupling factor for standard and improved layout.

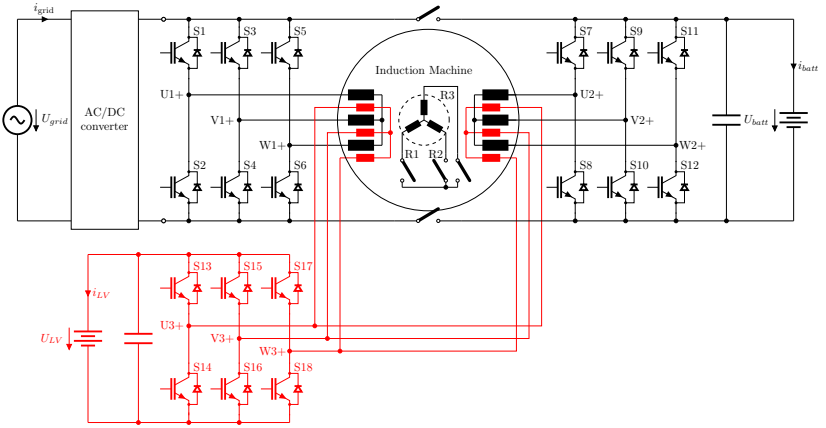

Figure 3.12: Integration of LV DC/DC converter in integrated charger.

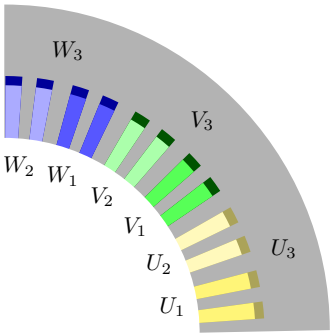

Figure 3.13: Suggested layout for extra winding used for DC/DC converter operation.

functionality in the EM. The main reason for the required active volume of the EM is that the DC/DC converter is required to operate during both charging at vehicle standstill and during normal driving conditions. Hence, it is assumed that auxiliary power take out to the LV DC/DC converter could occur at any EM load condition, including during that of peak traction performance. Moreover, additional power electronics is required to connect the HV and LV batteries. Hence, this further integration is not beneficial in terms of volume reduction when compared to a separate DC/DC converter that operates at much higher switching frequencies and thus, uses much smaller components.

3.4 Cost Analysis

A summary of all required components and drivetrain changes for the isolated charger topology with an estimated cost are listed in Tab. 3.1. The total is with 330 Euro estimated to be similar to the cost of a 11 kW three-phase dedicated onboard charger based on the design of [3]. Note that the LV DC/DC converter for the board net is not included in the analysis due to its high volume. The rotor disconnection switches are the most expensive. These consist of rotating SiC power electronics that can withstand high rotational speeds and high traction currents, as well as a mechanism for rotating control signals. The extra production cost for the winding insertion of the wound rotor are reflected, as this is needed to prevent short circuits in the rotor paths during charging. Furthermore, the winding reconnection device for efficiency improvements is considered optional and should thus be added to the total cost if used. Moreover, it is assumed that the 2x3-phase drive system is already in place, e.g. for redundancy purposes.

Component	**Cost (EUR)**
AC/DC converter	100
rotor disconnection switches	200
wound rotor	30
Total	**330**
optional winding reconnection device	75

Table 3.1: Charging specific added cost distribution.

3.5 Motivation to focus on non-isolated chargers

Significant efficiency improvements in comparison to state of the art topologies for isolated integrated charging using the EM at standstill [53, 55] have been presented. However, with a total AC grid to battery efficiency of 88%, the results are still significantly below that of dedicated onboard chargers with galvanic isolation. Furthermore, the high added cost to the EM for rotor deactivation makes this concept economically unattractive, it is about as expensive and lacks at least 6% of efficiency compared to the dedicated onboard charger concept as presented in [3]. This efficiency reduction is mainly due to the transformer efficiency which is with 94% much lower than that of a high frequency transformer. The efficiency drop is caused by the relatively long air gap and other large EM dimensions required for peak traction capabilities. Moreover, the IM and especially its laminated core is optimized for high power electro-mechanical energy conversion with corresponding high magnetic field densities in traction mode rather than to function as a high efficient transformer for charging. Transformers in dedicated BEV onboard chargers typically operate at much higher frequencies and use ferrite cores instead of laminated steel cores to improve the efficiency. The only found advantage of this concept versus dedicated onboard chargers is some volume savings as the DC/DC stage of a dedicated onboard charger is integrated in the e-drive. However, these savings are estimated at only 44% based on a 11 kW variant of [3]. The main volume that is still left is for the AC/DC converter and the net filter.
Since galvanic isolation when implemented in the EM with a rotor at stand still leads to a significant reduction of efficiency compared to dedicated chargers, it highly recommended to investigate non-isolated integrated chargers and to solve the need for protection against galvanic shock by other measures than isolation. If more cost effective ways of improving the efficiency and deactivation switching gear are available or if an additional use of the rotor disconnection can be identified in the future, it might be worth to reassess the isolated charger concept.
As a preparation for the efficiency assessment of non-isolated chargers, the losses theory of the motor drive system in non-isolated charging mode with DC bias and switching ripple as a main frequency component are assessed in chapter 4. Afterwards, two novel galvanically coupled integrated chargers are introduced in chapter 5 and a detailed efficiency review is presented.

4

Detailed e-drive Losses during Charging Condition

As concluded in chapter 3, integrated charging using the EM as a transformer at standstill is not feasible within limited losses and additional drivetrain cost. Hence, two new concepts using the EM windings as inductances for a non-isolated DC/DC converter are introduced in chapter 5 and are accompanied with efficiency calculations and measurements. In order to provide a detailed losses and efficiency review of the actual concepts in chapter 5, a theoretical overview of the losses behavior of the drivetrain under DC biased charging conditions is provided in this chapter. Calculation methods for copper, iron, and inverter losses are discussed. The model parameters for these losses can significantly differ from those under driving conditions, since charging is typically performed at power levels significantly below traction power, an area that is not always precisely described in most loss models. Moreover, the influence of the switching frequency on the losses is significantly more important in charging mode than in traction mode due to these lower power levels. In addition, the DC current in charging mode has further impact on the validity of the loss models. Therefore, the inverter and EM loss calculation models are reviewed in this chapter and are adapted for charging conditions where needed.
The EM model with 30° phase shift between the primary and secondary winding sets as assessed in chapter 3 was not available as a physical prototype. A similar EM design without phase shift was available in hardware for measurements.

Hence, slight modifications are made to the EM model used in chapter 5 in order to reduce any discrepancies between simulations and measurements of the non-isolated charger concepts. In fact, the stator and rotor geometries and cross sections remain identical to the model of chapter 3, however there are two changes:

- The winding arrangement: while the EM analyzed in chapter 3 has a 30 degrees phase shift between the primary and the secondary winding set, the physical prototype used in chapter 5 has zero degrees phase shift. Therefore, the winding arrangement in the FEM model has been modified to remove the phase shift between the two winding sets to match the FEM model used in chapter 5 with the actual prototype. This results in a slightly lower peak torque and power as well as a slightly lower phase resistance for the design without phase shift.
- The steel material processing: in both models the M330-35A steel is used for both rotor and stator. The EM analyzed in chapter 3 has a BH curve and iron loss parameters for production ready stamped steel for both stator and rotor. However, the available hardware prototype EM used in chapter 5 consists of a stamped rotor and a laser cut stator. Hence, the iron characterization i.e. the BH curve and the iron loss coefficients should be reviewed prior to using the FEM model.

An overview with the most important EM parameters is presented in Tab. 4.1. The BH curves are assessed in section 4.1 and the Steinmetz loss coefficients for the iron losses are reviewed in section 4.2. In addition to the iron properties, the EM copper losses are described in section 4.3. Finally, the inverter losses are reported in section 4.4. All analyses are performed at a temperature of 25 °C as the inverter and EM are Water Ethylene Glycol (WEG) cooled and the actual load during charging is significantly below that of the traction capabilities.

4.1 BH Curve

The BH relationship has been measured for both the laser cut stator and the stamped rotor steel and has been verified with the standard available curve in the FEM model for stamped M330-35A material. Epstein strips of both materials have been measured using a Remagraph C - 500 automated Personal Computer (PC) controlled measurement instrument from MAGNET-PHYSIK [D1] that follows IEC standard 60404-4 [68]. The measurement setup is presented in

Parameter	Value
Power	153/144 kW
Torque	287/270 Nm
Rotational speed	15,000 rpm
Base frequency	171 Hz
Number of poles	4
Phase inductance	1.7/1.2 mH
Phase resistance	103/80 mΩ
Active diameter	180 mm
Active length	180 mm
Airgap length	0.7 mm
Stator lamination	M330-35A, stamped/laser cut
Rotor lamination	M330-35A, stamped

Table 4.1: Key EM parameters.

Fig. 4.1 and is used to measure the magnetization M as function of the magnetic field strength H. The Epstein frame holder with the strips is shown in Fig. 4.2. Several Epstein strips are stacked on top of each other while alternating cut perpendicular to and in the steel rolling direction. The stamped and laser cut Epstein strips are illustrated in Fig. 4.3 and Fig. 4.4 respectively. These Epstein strips are in addition to two measuring coils installed between the poles of a yoke. A magnetic field is induced in the yoke by a current through the yoke windings that is generated from the computer controlled power amplifier. The measuring coils are connected to two electronic flux meters, which measure the magnetization M and the magnetic field strength H. Since M is measured, the flux density B is calculated using

$$B = M + \mu_0 H. \tag{4.1}$$

Hysteresis is not used in FEM to simplify the calculations. Therefore, an anhysteresis curve using an averaging of both hysteresis legs is created from the measured BH curve. The measurement results of the anhysteresis curves are plotted in Fig. 4.5 for both the laser cut and the stamped strips, as well as the original curve for stamped M330-35A that is based on multiple measurements and typically used for simulations. A second plot with an enlarged view of the area at low field strengths is presented in Fig. 4.6. Note that the results can differ

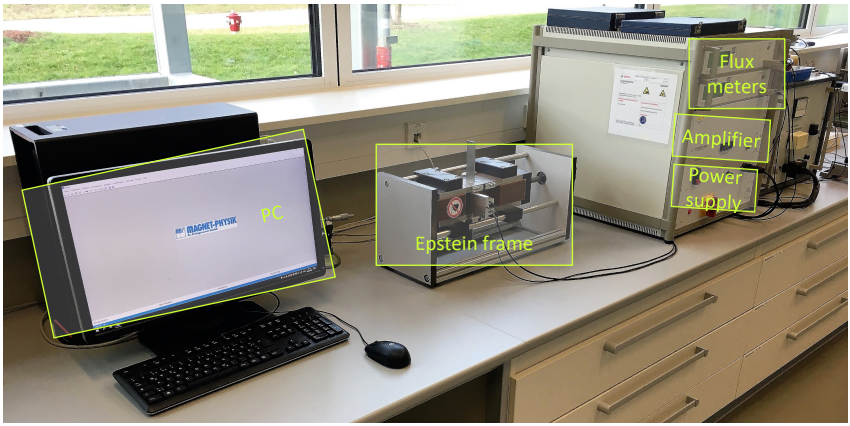

Figure 4.1: Test stand for measurements of the BH curves.

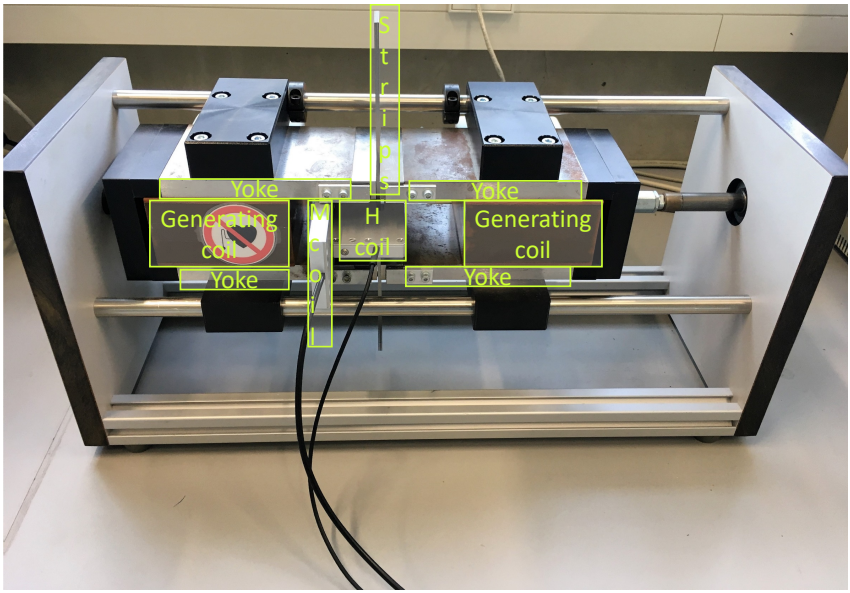

Figure 4.2: Epstein frame for measurements of the BH curves.

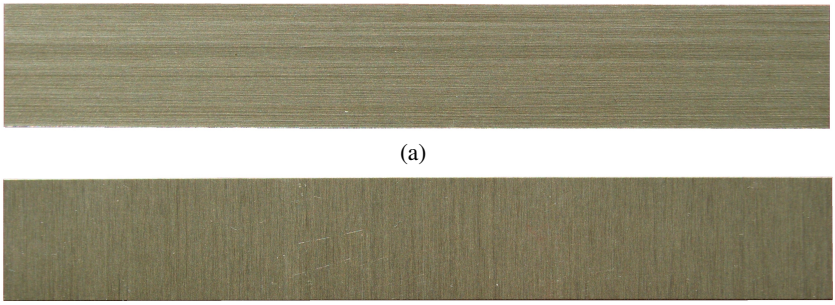

(a)

(b)

Figure 4.3: Stamped Epstein strips (a) in, and (b) perpendicular to steel rolling direction.

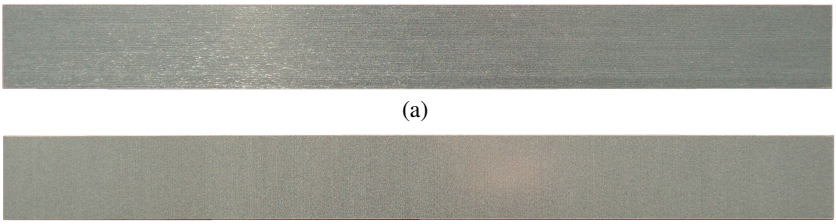

(a)

(b)

Figure 4.4: Laser cut Epstein strips (a) in, and (b) perpendicular to steel rolling direction.

between the different material processing techniques since the grade M330-35A only implies maximum core losses of 3.3 Watt per kg for a field of 1.5 T at 50 Hz. Therefore, the actual material content specification, and thus the behavior of the actual BH curve, may differ from sample to sample as long as the maximum loss requirements at 50 Hz are met. Hence, it was decided to utilize the standard available M330-35A BH curves in the FEM model since it cannot be guaranteed that the measured curves for the samples of Epstein strips are closely matching the curve of the steel in the actually used prototype EM. Note that the laser cut BH curve seems to be more linear up to 1.3 T than the stamped curve, which is more similar to the standard available curve.

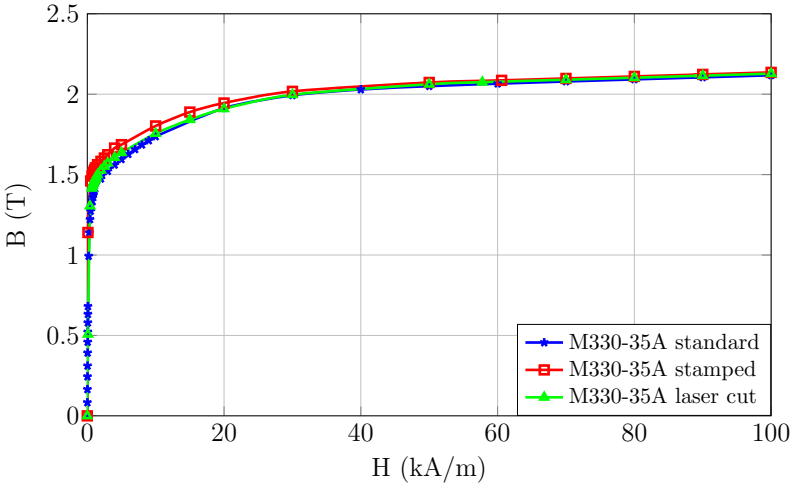

Figure 4.5: BH curve for the measured materials versus the standard M330-35A curve.

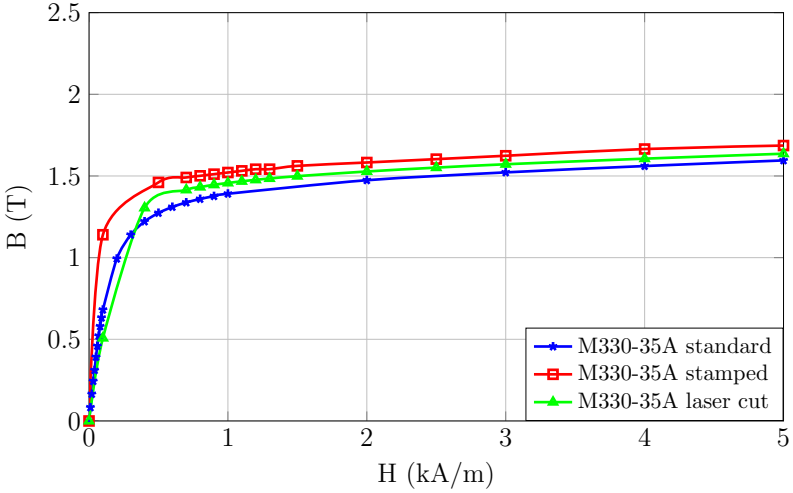

Figure 4.6: Zoomed view of the BH curve.

4.2 Iron Losses

The iron losses in the stator and rotor laminations include hysteresis losses, eddy current losses, and excess losses. The hysteresis losses occur due to the hysteresis loops travelling on the BH curve, which are a result of the magnetization process. Moreover, eddy currents are currents induced in the lamination as a result of the conductivity of the steel and the applied time changing B fields. This effect is similar to the skin effect in the copper windings, and can be reduced by using thinner laminations. Finally, the excess losses describe all losses in addition to the hysteresis and eddy current losses.
The classical hysteresis losses are calculated with the Steinmetz formula in analytical form and/or with aid of a FEM tool:

$$P_{\mathrm{Fe}} = K f^{\alpha} B^{\beta}. \tag{4.2}$$

A more precise calculation method is commonly used for EMs in traction mode and is based on the Jordan loss separation method as described in (3.1), which is repeated here:

$$P_{\mathrm{Fe}} = P_{\mathrm{hys}} + P_{\mathrm{eddy}} = K_{\mathrm{h}} f^{\alpha} B^{\beta} + K_{\mathrm{e}} f^{\gamma} B^{\delta}. \tag{4.3}$$

This equation splits the losses into hysteresis and eddy current components. Typically, α is 1 and γ is set to 2, while parameters K_{h}, K_{e}, β, and δ are based on material measurements. These material parameters are extracted performing specific loss measurements with ring cores of the actual steel as used in the EM and are normally measured for high B fields and the low fundamental frequencies up to several hundreds of hertz. Hence, additional losses due to the switching ripple are usually not reflected. In charging conditions, the EM is typically used at a significantly lower power level, i.e. smaller alternating magnetic fields B_{AC}. Meanwhile, the main contribution to the iron losses is a result of the high frequency switching ripple and its harmonics with even higher frequencies. Moreover, the DC offset current causes a DC offset B_{DC} in the magnetic fields, which might lead to additional losses [69–71], dependent on the level of charging current. Therefore, it is useful to perform iron specific loss measurements for the B fields and frequencies including excess losses and DC offset that are relevant for charging conditions to obtain correct Steinmetz parameters, instead of relying on the material parameters obtained for traction mode that are only valid for unbiased hysteresis and eddy current loss effects at low fundamental frequencies. Thus, measurements have been performed in a similar method as described in [69] by using the test setup as shown in Fig. 4.7.

This test setup follows DIN IEC standard 60404 [72] and is further elaborated in [S4]. A schematic is presented in Fig. 4.8.

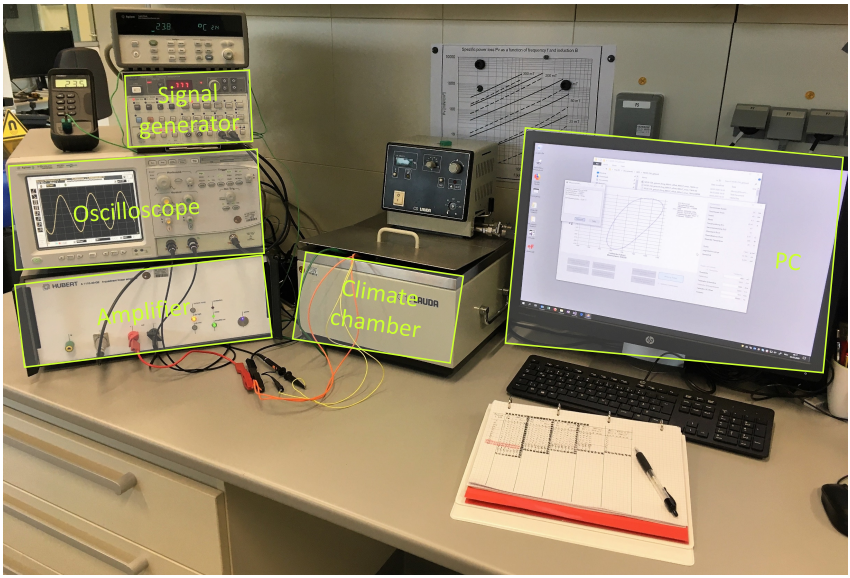

Figure 4.7: Test stand used for specific iron loss measurements.

The desired DC offset magnetic field B_{DC} superpositioned by an AC magnetic field B_{AC} of desired amplitude and frequency is induced in the Core Under Test (CUT) by a PC controlled signal generator with a power amplifier via a current through winding n_1. The core losses are measured with an oscilloscope by the voltage drop $u_{\mathrm{R}}(t)$ across resistor R that represents the magnetic field strength $H(t)$ and by the voltage drop $u_2(t)$ across winding n_2 that represents the magnetic flux density $B(t)$. The power per unit of volume, i.e. the loss power density of the ring, equals the enclosed area of the BH loop multiplied by the frequency [69] and is calculated and stored at the PC. In order to verify that the resulting magnetic field $B(t)$ matches the desired waveform, the PC iteratively controls and adjusts the signal generator. The magnetic flux density is calculated from the measured voltage $u_2(t)$ as

$$B(t) = -\frac{1}{n_2 A}\int_0^t u_2(t)dt + c. \tag{4.4}$$

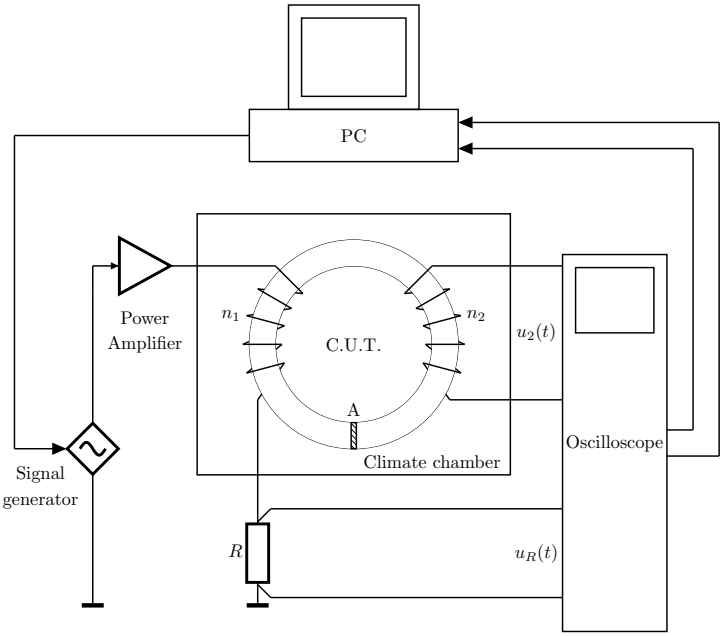

Figure 4.8: Schematic test setup for iron loss measurements.

This measurement is repeated for a range of frequencies using multiple sinusoidal B field amplitudes and DC bias levels. The ring samples with stacked laminations and a total cross section A are installed in a water bath that functions as a climate chamber in order to keep the temperature constant at 25 °C. The typical and maximum accuracy is ±1% respectively ±4% of the reading and is mainly determined by geometrical tolerances of the ring cores. The control and measurements of the B and H fields and corresponding voltages are significantly more precise with an accuracy of ±0.1%.
Since a stamped rotor and a laser cut stator were used in the tested EM, both of material grade M330-35A, two sets of stacked rings have been used for material specific loss measurements. These are pictured in Fig. 4.9: the left ring is made of laser cut steel and the right ring is made from stamped steel. Both are equipped with a primary winding in orange and a secondary winding in yellow. Furthermore, the ring made out of stamped steel sheets has a temperature sensor

installed. In order to obtain a realistic influence of the production process, rather than using a general safety factor, the stamped and laser cut ring cores were ordered from the identical supplier and to be made with similar production processes and parameters as the EM steel in the EM prototype. Therefore, the influences of the production process parameters for laser cutting on the stator loss behavior and for stamping on the rotor loss behavior of the actual EM prototype should relatively well be reflected in the measured specific iron losses. These effects include for example influences of the guillotine shearing [73–77] for the stamped rotor laminations and the laser type, speed, and intensity [74–77] for the laser cut stator laminations.

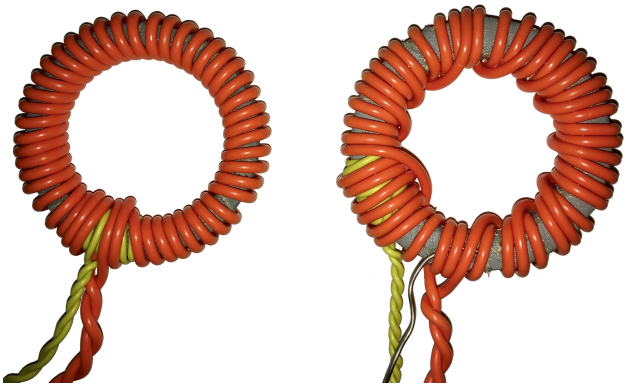

Figure 4.9: Ring probes. Left: laser cut steel, right: stamped lamination.

The iron losses are measured at various frequencies between 5 and 60 kHz in B_{AC} intervals of 100 mT between 0 and 0.5 T. Moreover, offset magnetic fields B_{DC} between 0 and 1.2 T in intervals of 0.2 T DC are used to represent different levels of charging currents. The maximum possible B_{DC} values that were measured for a given combination of frequency and AC field are presented in Tab. 4.2a and in Tab. 4.2b for the stamped rotor and laser cut stator rings respectively. Based on the presented combination of AC fields and frequencies with an interval of 0.2 T DC offset between zero and 1.2 T, a total of 257 and 259 measurements out of the theoretical 455 points are made with the laser cut and stamped rings respectively. Although the power amplifier could supply power for all theoretical points, the thermal limitation reduces the amount of measurement points. Combinations of frequencies and magnetic fields B_{AC} that could not be measured are denoted with 'n.a.'.

$f(kHz)$ \ $B_{AC}(T)$	**0.1**	**0.2**	**0.3**	**0.4**	**0.5**
5	1.2	1.2	1.2	1.2	1.2
10	1.2	1.2	1.2	1.2	1.2
12.5	1.2	1.2	1.2	1.2	1.2
15	1.2	1.2	1.2	1.2	1.2
20	1.2	1.2	1.2	1.2	n.a.
25	1.2	1.2	1.2	0.6	n.a.
30	1.2	1.2	1.2	n.a.	n.a.
35	1.2	1.2	0.4	n.a.	n.a.
40	1.2	1.0	n.a.	n.a.	n.a.
45	1.0	0.0	n.a.	n.a.	n.a.
50	1.0	n.a.	n.a.	n.a.	n.a.
55	0.0	n.a.	n.a.	n.a.	n.a.
60	0.0	n.a.	n.a.	n.a.	n.a.

a Stamped

$f(kHz)$ \ $B_{AC}(T)$	**0.1**	**0.2**	**0.3**	**0.4**	**0.5**
5	1.2	1.2	1.2	1.2	1.2
10	1.2	1.2	1.2	1.2	1.2
12.5	1.2	1.2	1.2	1.2	1.2
15	1.2	1.2	1.2	1.2	1.2
20	1.2	1.2	1.2	1.2	n.a.
25	1.2	1.2	1.2	n.a.	n.a.
30	1.2	1.2	1.2	n.a.	n.a.
35	1.2	1.2	n.a.	n.a.	n.a.
40	1.2	1.2	n.a.	n.a.	n.a.
45	1.2	n.a.	n.a.	n.a.	n.a.
50	1.2	n.a.	n.a.	n.a.	n.a.
55	0.8	n.a.	n.a.	n.a.	n.a.
60	n.a.	n.a.	n.a.	n.a.	n.a.

b Laser cut

Table 4.2: B_{DC} limits of ring cores measured as function of AC B field and frequency.

The losses are plotted as function of B_{DC} in Fig. 4.10 and in Fig. 4.11 for the stamped rotor and laser cut stator steel sheets respectively. Since all iron loss phenomena are included in the ring core measurements, one parameter set per material like in (4.2) can be used to describe all relevant iron loss effects at a given field offset field B_{DC} if α is not fixed to 1 or 2 to only describe the hysteresis or eddy current losses. Two different sets of values for K, α, and β were found: one set of values for the stator and one for the rotor. Moreover, K and β vary for different offset levels, while α remains constant for increased DC offset fields densities [69]. The specific losses as function of DC B field offset are plotted in Fig. 4.12 for the stamped laminations and in Fig. 4.13 for the laser cut laminations. Furthermore, the frequency linearity is plotted for different offset levels and amplitudes of the magnetic field in Fig. 4.14 and in Fig. 4.15 for the stamped and laser cut ring samples respectively. Moreover, the magnetic field linearity is plotted for different offset levels and frequencies in Fig. 4.16 and in Fig. 4.17 for the stamped and laser cut ring samples respectively. The losses are very linear over the AC magnetic field density and frequency range for all offset magnetic field levels B_{DC}. This is especially true for the laser cut probe with the exception of the losses at an offset of 1.2 T and 100 mT amplitude due to saturation effects. This means that this offset level cannot describe the

iron losses well with the Steinmetz equation. Since the iron losses are in this thesis only analyzed for a small charging power, these high offset levels are not present in the steel laminations. Several outliers are also visible, mainly in the plots representing the stamped rotor laminations.
The ratios K/K_0 and β/β_0 of change in the Steinmetz parameters with respect to the values without DC offset are presented in Fig. 4.18. The offset levels of the B fields are 0.2 T DC in the boost windings and 0 T DC and 0.6 T DC in the buck converter in W respectively Y connection for a 6.6 kW load. Thus, six values for K and β are used: three for the laser cut stator and three for the stamped rotor equations, dependent on the circuit and offset level. An overview of all used parameters for the iron loss calculation is provided in Tab. 4.3. The parameters were found using the curve fitting toolbox in Matlab (cftool command). This command creates a surface fit for each B_{DC} offset level based on the losses measured for all B_{AC} and f combinations, and uses the Steinmetz equation as a base. α is determined from the measurements at 0 T DC offset. K and β are determined based on the smallest non-linear least squares error for the parameter values for each offset level. Outliers above 50 W/kg error are identified and removed. Furthermore, the coefficients of determination R^2 and the R^2_{adj} are kept at a maximum while the Root Mean Square Error (RMSE) and the Sum of Squared Errors (SSE) are reduced to a minimum.

Parameter	**Stator value**	**Rotor value**
α	1.52	1.582
K_{boost}	32.9981	15.4636
$K_{\mathrm{buck,W}}$	33.2733	15.479
$K_{\mathrm{buck,Y}}$	33.877	16.9961
β_{boost}	1.823	1.889
$\beta_{\mathrm{buck,W}}$	1.822	1.891
$\beta_{\mathrm{buck,Y}}$	1.809	1.936

Table 4.3: Steinmetz parameters for 6.6 kW load.

The iron losses in the stator and rotor are calculated with the Bosch in-house FEM tool Edyson using (4.2) and the found Steinmetz parameters in post processing for a 2D FEM model of the selected EM. Any calculation method corrections for non-sinusoidal B field waveforms are not explicitly implemented using Modified Steinmetz Equation (MSE) [78, 79], Generalized Steinmetz Equation (GSE) [79, 80], or Improved Generalized Steinmetz Equation (IGSE)

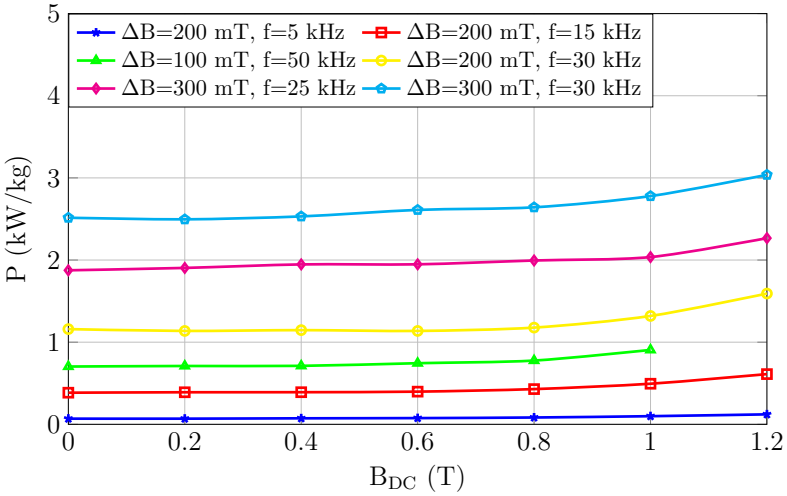

Figure 4.10: Iron losses as function of offset for stamped rotor.

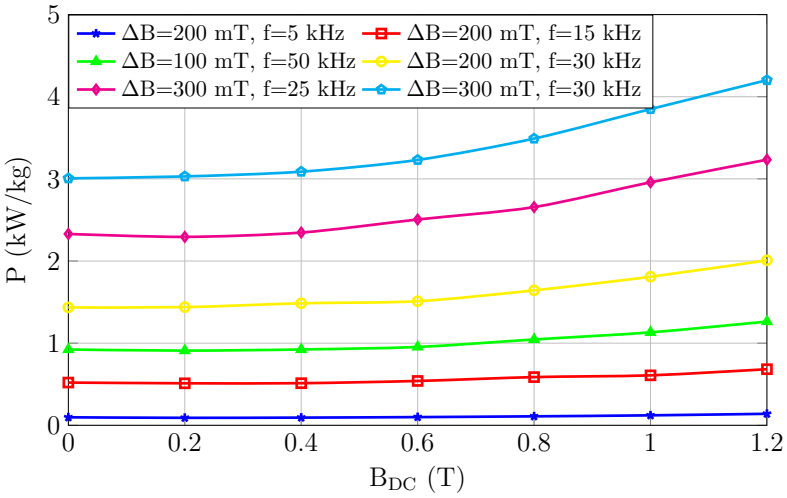

Figure 4.11: Iron losses as function of offset for laser cut stator.

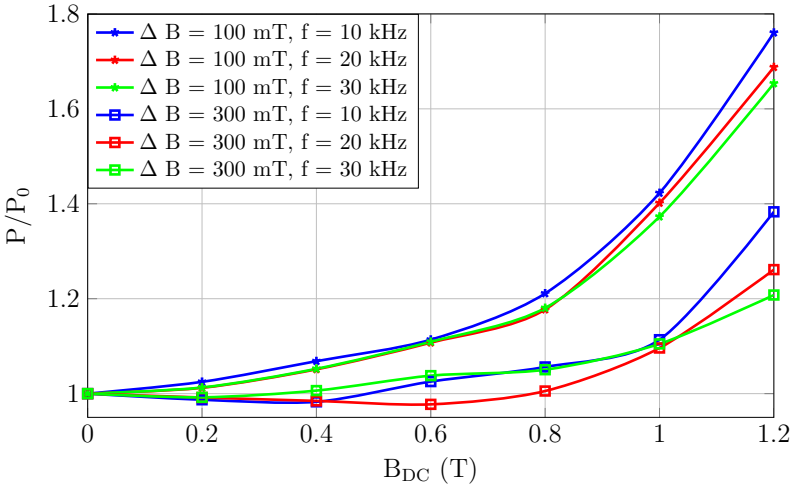

Figure 4.12: Iron losses normalized to 0 T offset for stamped rotor.

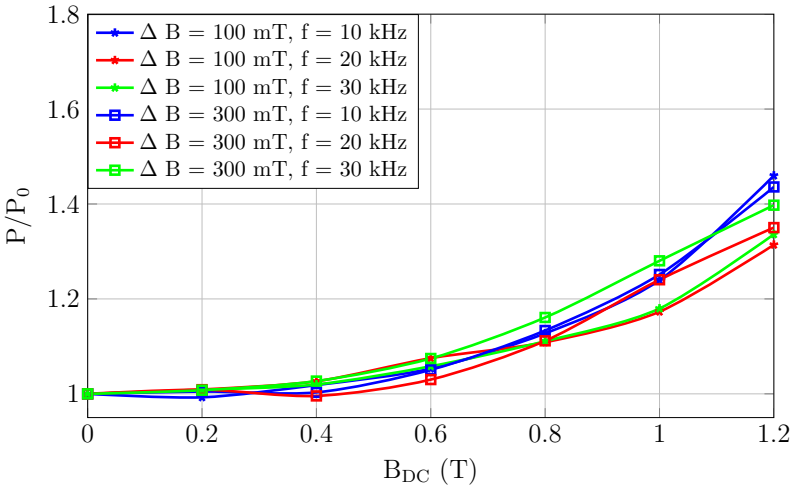

Figure 4.13: Iron losses normalized to 0 T offset for laser cut stator.

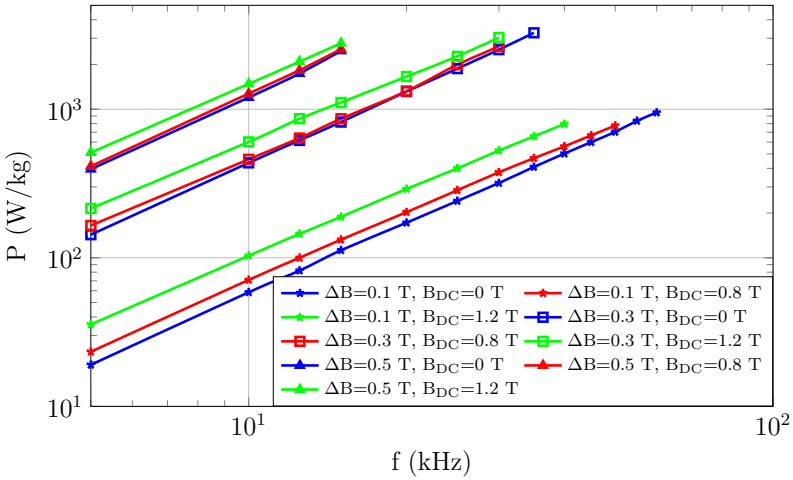

Figure 4.14: Iron losses frequency linearity for stamped rotor.

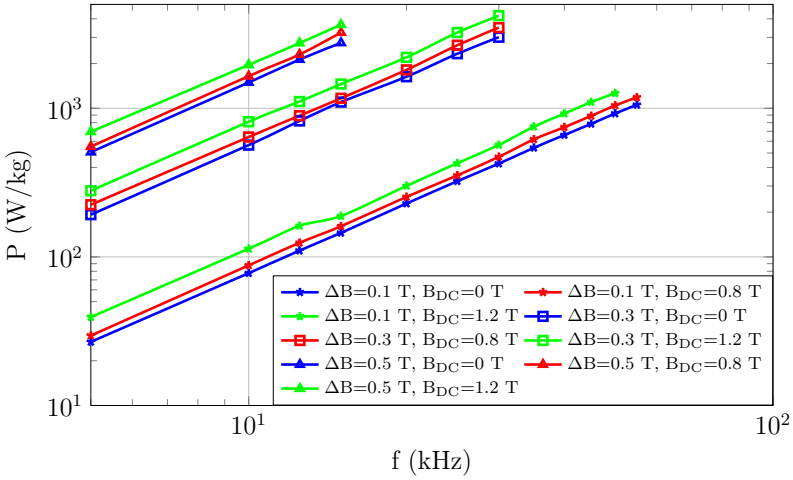

Figure 4.15: Iron losses frequency linearity for laser cut stator.

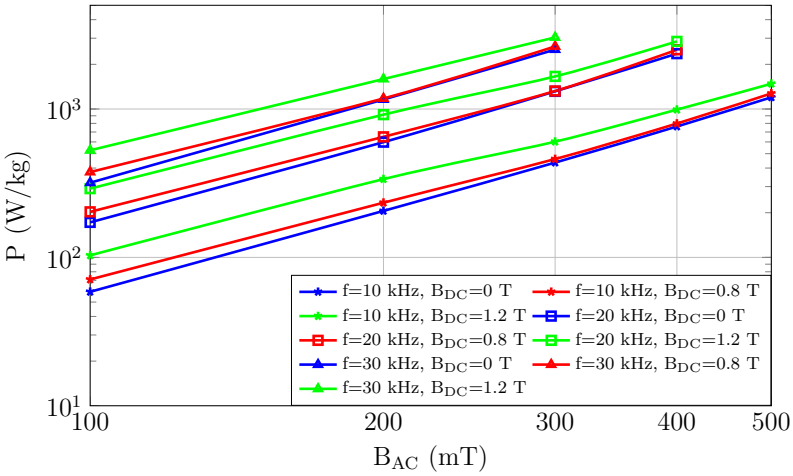

Figure 4.16: Iron losses B_{AC} linearity for stamped rotor.

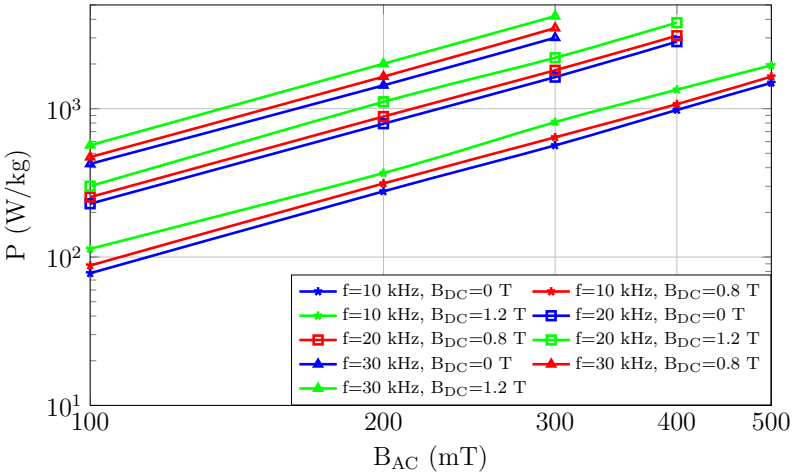

Figure 4.17: Iron losses B_{AC} linearity for laser cut stator.

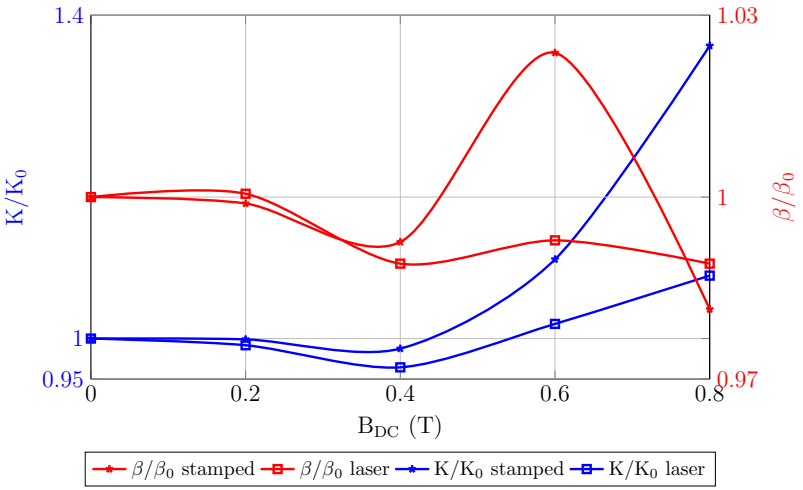

Figure 4.18: Variation ratio of K and β as function of DC offset B field density.

[79, 81]. Instead, effects of non-sinusoidal waveforms is reflected in the Fast Fourier Transformation (FFT) analysis of the B field due to the implementation in the FEM tool, which is duty cycle and waveform independent.

4.3 Copper Losses

Copper losses are all heat losses generated in the EM windings as a result of current flowing through these windings. These losses are caused by the specific resistance of the winding material and the geometrical dimensions of the winding. Copper losses can be divided in those resulting from the main current i.e. the classical Ohmic losses and those from eddy currents resulting from AC B-fields. Furthermore, a differentiation can be made between the losses generated in the active part of the EM as well as losses generated in the end windings. Moreover, the copper losses in the rotor bars should be assessed for induction machines. The classical Ohmic losses and the additional losses due to the eddy currents in the stator windings are analytically described here as a basis for the stator copper losses of the concepts analyzed in chapter 5. The

rotor copper losses will be assessed numerically as part of the FEM simulations in chapter 5.

4.3.1 Classical Ohmic Losses

The classical copper losses, often referred to as DC losses in literature [82], can be calculated using Ohms law

$$P_{\mathrm{Cu,DC}} = I^2 R = I^2 \rho \frac{l}{A}. \tag{4.5}$$

This equation is only valid for homogeneous current density in a conductor, which is typically only true for DC currents. For AC currents, the copper losses can be calculated using

$$P_{\mathrm{Cu,AC}} = \frac{l}{\sigma} \iint_A J^2 \, dA. \tag{4.6}$$

It is rather difficult to define the current density distribution J within a winding and across different windings in the slot due to the interaction of different magnetic fields created by the multiple wire strands within that slot. Although it is possible to calculate this current density with FEM, analytical formulas have been developed to calculate the AC losses with use of two extra loss factors. As a result, (4.5) can with these factors be extended to

$$P_{\mathrm{Cu}} = {I_{\mathrm{DC}}}^2 R_{\mathrm{DC}} + {I_{\mathrm{AC}}}^2 R_{\mathrm{DC}} (k_{\mathrm{P}} + k_{\mathrm{C}} - 1). \tag{4.7}$$

These extra loss factors are dependent on three effects: skin effect and proximity effect described with factor k_{P}, and circulating currents expressed with factor k_{C}. These effects and calculation methods are described in the literature [82–85]. A summary of these phenomena with the most important formulas for analytical calculation is for completeness provided in the paragraphs below.

4.3.2 Skin and Proximity Effect

The skin effect is the phenomenon that describes the inhomogeneous current density as a result of magnetic fields that are generated by alternating currents in the very same wire. These magnetic fields induce eddy currents, which lead to an inhomogeneous current density: the core of the wire has a lower current density and most of the current flows at the surface i.e. the skin of the wire. As a result, higher losses will occur due the locally increased current density. The

skin effect is typically reduced by using multiple isolated thinner wire strands rather than one thick wire.
If multiple wire strands are placed closely together, such as in an EM slot, magnetic fields produced by alternating currents flowing in one wire can induce eddy currents in the other wires that are placed in close proximity of the wire that produces the magnetic field. This is often called the proximity effect.
Both skin and proximity effect take place in the active part of the EM as well as in the end windings, although the former is significantly present [82]. All effects are often combined in one loss correction factor k_{P}. This factor comprises the correction factor for the skin and proximity effect over the active length, $k_{\mathrm{P,AL}}$, and the skin and proximity effect in the end winding, $k_{\mathrm{P,EW}}$, and is calculated over the ratio of active length l_{AL} and end winding length l_{EW} as

$$k_{\mathrm{P}} = \frac{k_{\mathrm{P,AL}} l_{\mathrm{AL}} + k_{\mathrm{P,EW}} l_{\mathrm{EW}}}{l_{\mathrm{AL}} + l_{\mathrm{EW}}}. \tag{4.8}$$

The skin and proximity loss factor for the active part of the EM can be calculated with

$$k_{\mathrm{P,AL}} = \varphi(\beta_{\mathrm{s}}) + \frac{{z_{\mathrm{h}}}^2 - 1}{3} \psi(\beta_{\mathrm{s}}). \tag{4.9}$$

The skin and proximity effects are expressed with the auxiliary functions φ respectively ψ, which are both functions of the reduced strand height β_{s}. These functions can be calculated as

$$\varphi(\beta_{\mathrm{s}}) = \beta_{\mathrm{s}} \frac{\sinh(2\beta_{\mathrm{s}}) + \sin(2\beta_{\mathrm{s}})}{\cosh(2\beta_{\mathrm{s}}) - \cos(2\beta_{\mathrm{s}})} \tag{4.10}$$

and

$$\psi(\beta_{\mathrm{s}}) = 2\beta_{\mathrm{s}} \frac{\sinh(\beta_{\mathrm{s}}) - \sin(\beta_{\mathrm{s}})}{\cosh(\beta_{\mathrm{s}}) + \cos(\beta_{\mathrm{s}})}. \tag{4.11}$$

The frequency dependent reduced strand height β_{s} is calculated with

$$\beta_{\mathrm{s}} = d_{\mathrm{s}} \frac{\pi}{2} \sqrt{f \mu \sigma \sqrt{k_{\mathrm{Cu}}}} \tag{4.12}$$

where d_{s} is the strand diameter and k_{Cu} the slot fill factor. The factor z_{h} identifies the number of strands located on top of each other in radial direction within the slot under the assumption that all strands are equally distributed [82]. This factor is calculated using

$$z_{\mathrm{h}} = h_{\mathrm{slot}} \sqrt{\frac{k_{\mathrm{Cu}}}{A_{\mathrm{s}}}} \tag{4.13}$$

where h_{slot} equals the slot height and A_{s} the area of a single wire strand.
Although stated in [82] that the skin and proximity loss factor $k_{\mathrm{P,EW}}$ for the end windings may be neglected i.e. set to one, it is possible to calculate these effects in the end windings with the identical method to that above with two corrections: the changed reduced strand height $\beta_{\mathrm{s,EW}}$ and the altered factor $z_{\mathrm{h,EW}}$ for the number of strands located on top of each other in the end winding. Therefore, the reduced strand height of the end windings becomes:

$$\beta_{\mathrm{s,EW}} = \beta_{\mathrm{s}} \sqrt{\frac{w_{\mathrm{slot}}}{w_{\mathrm{slot}} + 1{,}2 h_{\mathrm{slot}}}}. \tag{4.14}$$

Parameter h_{slot} represents the slot height and the average slot width is expressed with w_{slot}. Moreover, the factor $z_{\mathrm{h,EW}}$ equals $z_{\mathrm{h}}/2$ [83]. Therefore, the end winding factor $k_{\mathrm{P,EW}}$ is expressed as:

$$k_{\mathrm{P,EW}} = \varphi(\beta_{\mathrm{s,EW}}) + \frac{{z_{\mathrm{h}}}^2 - 4}{12} \psi(\beta_{\mathrm{s,EW}}). \tag{4.15}$$

4.3.3 Circulating Currents

If the wires are divided in multiple individual strands to reduce the skin effect, these tend to have different flux linkages due to a difference in the exact location of each strand within the slot. As a result, extra voltages will be induced in each strand and therefore, extra currents are generated. These currents flow within the parallel strands of a winding and are often referred to as circulating currents. These circulating currents lead to extra losses in the winding, in addition to the skin and proximity losses. The level of these circulating currents, with corresponding losses, is highly dependent on the actual wire displacement within the slot. In other words, the amount of circulating currents is defined by the possibility to place the different parallel strands on the same radius in the slot. An example of this is illustrated in Fig. 4.19, where a good winding layout is presented in the left picture and a bad winding layout is shown in the right picture. If parallel strands of a winding are similarly distributed along the slot radii, a smaller spread in leakage flux is seen and thus, lower circulating currents are induced.

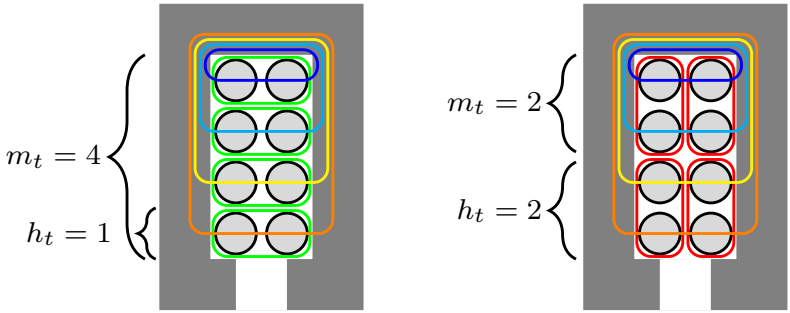

(a) (b)

Figure 4.19: Observed flux leakage in strands for: (a) good, (b) bad winding placement.

The extra loss factor for the circulating currents can also be calculated using (4.10) and (4.11) for the auxiliary functions φ respectively ψ. The loss factor correction losses factor k_C is then calculated using

$$k_C = \varphi(\beta_t) + \eta(\eta+1)\psi(\beta_t). \tag{4.16}$$

Since the circulating currents are present in the entire coil, thus both in the active length and the end winding, any adjustment factors such as in (4.8) are not required [85]. Instead, the reduced turn height, β_t, has an included correction factor for the ratio of the active to the total length. The reduced turn height β_t is calculated as using

$$\beta_t = h_t \sqrt{f\mu\sigma\pi \frac{l_{AL}}{l_{AL}+l_{EW}} \sqrt{k_{Cu}}} \tag{4.17}$$

where h_t is the turn height, i.e. the height of the strands in one winding turn. Furthermore, the parameter η identifies the parallel wire displacement factor and is used to describe the winding placement. It is assumed that each slot has an identical winding placement and that there is no twisting of wires between different slots [82]. In that case, the parallel wire displacement factor η is calculated as:

$$\eta = \frac{m_t - 1}{2}. \tag{4.18}$$

In the example illustrated in Fig. 4.19, it is rather easy to identify the number of turns in radial direction, m_t, and the turn height, h_t. However, in reality it could be hard to determine the exact amount of windings placed in parallel on the same slot height due to the random insertion of the windings in the slots during production. Therefore, it might be best to identify the good and bad cases for m_t and h_t [83, 85]. For the good case, i.e. when the parallel strands almost have identical radial position, the parameters are calculated with:

$$h_{t,good} = \frac{n_{par}}{z_w} d_s \tag{4.19}$$

$$m_{t,good} = \frac{z_h z_w}{n_{par}}. \tag{4.20}$$

For the bad wire placement, the parameters can be calculated as:

$$h_{t,bad} = n_{par} d_s \tag{4.21}$$

$$m_{t,bad} = \frac{z_h}{n_{par}}. \tag{4.22}$$

Parameter n_{par} equals the number of parallel strands and z_h is calculated using (4.13). In contrast, the number of strands in tangential direction z_w is expressed as

$$z_w = w_{slot} \sqrt{\frac{k_{Cu}}{A_s}}. \tag{4.23}$$

Unfortunately, the exact winding placement in the slot could not be determined for the analyzed EM due to an uncontrolled winding insertion process. Therefore, the average value of $k_{C,good}$ and $k_{C,bad}$ based on $h_{t,good}$ and $m_{t,good}$ respectively $h_{t,bad}$ and $m_{t,bad}$ is used for calculation of k_C [83] to represent the average of a best and worst case winding placement.

4.3.4 Total influence of AC copper losses

In summary, the total loss increase for AC currents is calculated by using two loss factors: k_P for the skin and proximity effect, and k_C for the circulating currents. The frequency dependent influence of each factor is plotted in Fig. 4.20 for the IM that is analyzed. The circulating currents are dominant for lower frequencies and the combined skin and proximity effect becomes

dominant for frequencies in the range above 20 kHz. Hence, the circulating currents are the dominant copper loss contributor at grid frequencies and fundamentals of the switching frequency, while the proximity and skin effect become dominant for higher harmonics of the switching frequencies. Since both factors can be calculated over the frequency range, it is possible to calculate the AC copper losses for each frequency using the FFT of a non-sinusoidal current signal. Note that although the loss factor increases steeply for higher harmonics, the total loss components of these higher harmonics remain limited since these harmonics are less prevalent in the currents.

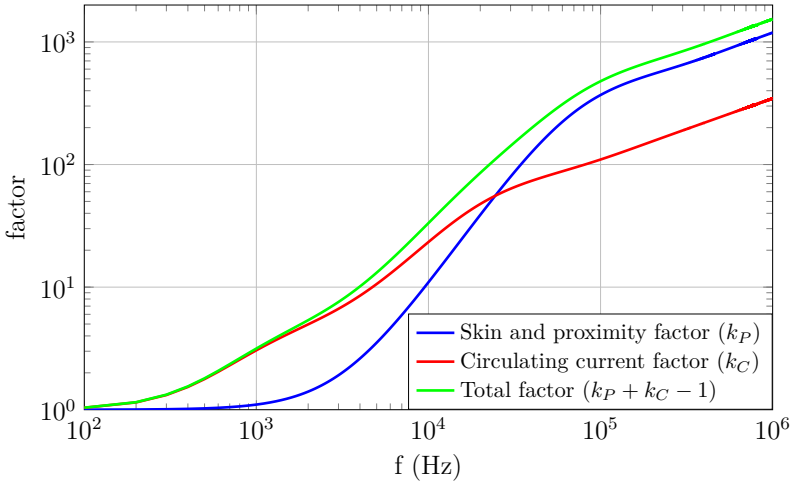

Figure 4.20: Loss factors for AC copper losses for the selected IM.

4.4 Inverter Losses

In contrast to the EM losses, the inverter losses can rather easily be calculated in case of DC biased charging. The conduction losses are calculated over a switching period T_s using

$$P_{\text{cond}} = \frac{1}{T_\text{s}} \int_{t}^{t+DT_\text{s}} u_{\text{CE}}(t) i_{\text{C}}(t) dt + \frac{1}{T_\text{s}} \int_{t+DT_\text{s}}^{t+T_\text{s}} u_{\text{F}}(t) i_{\text{D}}(t) dt \tag{4.24}$$

where D is the duty cycle and T_s is the switching time period. Linear approximation is used for the transistor voltage drop $u_{\text{CE}}(t)$. This approximation is based on datasheet values for the on resistance r_{CE}, the collector current $i_{\text{C}}(t)$, and the no load collector emitter voltage drop U_{CE0}:

$$u_{\text{CE}}(t) = U_{\text{CE0}} + r_{\text{CE}} i_{\text{C}}(t). \tag{4.25}$$

Similarly, the forward voltage drop $u_{\text{F}}(t)$ across the diode is based on the diode forward datasheet values for the resistance r_{F}, the diode current $i_{\text{D}}(t)$, and the no load forward voltage drop U_{F0}:

$$u_{\text{F}}(t) = U_{\text{F0}} + r_{\text{F}} i_{\text{D}}(t). \tag{4.26}$$

Although these linear approximations might lead to an overestimation on chip level, the values for the collector-emitter resistance r_{CE} and the diode forward resistance r_{F} are in reality slightly increased due to additional resistance in busbars and connections. Therefore, the overestimation on chip level might actually be reasonably accurate on a system level. In addition to the conduction losses, the switching losses are calculated using the turn on, turn off, and reverse recovery energies E_{on}, E_{off}, and E_{rr}:

$$P_{\text{sw}} = (E_{\text{on}} + E_{\text{off}} + E_{\text{rr}}) f_\text{s}. \tag{4.27}$$

Two Semikron SKAI 45 A2 GD12-W12DI inverters are used to analyze the different integrated charging concepts of chapters 3 and 5. These inverters are equipped with the SKiM459GD12E4V2 1200 V three-phase IGBT modules with IGBT 4 Trench Gate technology from Infineon. These modules support a nominal phase current of 450 A at a maximum switching frequency f_s of 20 kHz. The conduction losses are well specified in the datasheets [D2, D3] by parameters U_{CE0}, r_{CE}, U_{F0}, and r_{F}. However, the switching energies E_{on}, E_{off}, and E_{rr} for these modules are provided in the datasheet at a DC voltage of 600 V, a semiconductor temperature of 150 °C, and only for collector currents above 150 A [D3]. Since 6.6 kW charging functionality is reviewed in chapter 5 for DC voltages starting at 350 V, the maximum collector current of 20 A is significantly below the minimum current at which the switching losses are provided. Even maximum currents of 30 A for the isolated 11 kW battery charger concept in chapter 3 are still significantly below the values specified in

the datasheet. Moreover, DC voltages below 600 V and temperatures of 25 °C instead of 150 °C are used. Hence, measurements of the inverter switching losses at a double pulse test bench similar to [86] have been performed under real charging conditions, i.e. at DC link voltages in the range of 350-600 V, collector currents between 0-30 A, and at room temperature.
The double pulse method is a standardized method [87] to determine the switching energies of a semiconductor that is illustrated in Fig. 4.21 and Fig. 4.22 for respectively the transistor and the diode measurements. The inductor current $i_{\mathrm{L}}(t)$ is increased to the desired value by turning the transistor of semiconductor S6 on for the first instance. Thereafter, transistor S6 is turned off, and the inductor current $i_{\mathrm{L}}(t)$ commutates to the freewheeling diode of semiconductor S5. After sufficient waiting time, transistor S6 is turned on again and the current $i_{\mathrm{C}}(t)$ and voltage $u_{\mathrm{CE}}(t)$ are recorded with an oscilloscope during the second pulse. At the end of this pulse, the turn off behavior is measured. The turn on and off energies E_{on} and E_{off} respectively are the integral of the product of the measured voltages $u_{\mathrm{CE}}(t)$ across and currents $i_{\mathrm{C}}(t)$ through transistor S6. The reverse recovery energy E_{rr} of the diode is measured by exchanging the setup in Fig. 4.21 with Fig. 4.22. The lower transistor S6 is permanently off and the upper transistor S5 is now controlled. The reverse recovery energy E_{rr} is the integral of the product of the measured voltages $u_{\mathrm{F}}(t)$ across and currents $i_{\mathrm{D}}(t)$ through the diode of semiconductor S6.

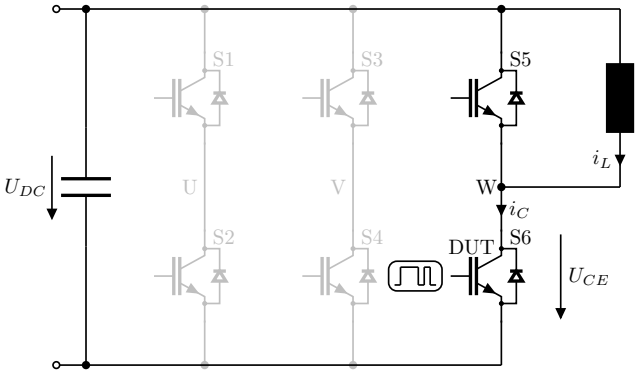

Figure 4.21: Measurement method for E_{on} and E_{off} of the bottom transistor.

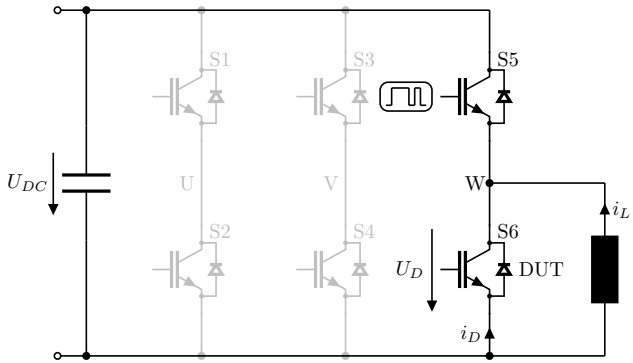

Figure 4.22: Measurement method for E_{rr} of the bottom diode.

The semiconductor switching energies are measured using the fully assembled inverter, i.e. taking into account all relevant components with their parasitic behavior such as the DC link capacitor, the busbars, and the actual preinstalled gate driver board as used in the system measurements in chapter 5. The double pulse test setup is illustrated in Fig. 4.23. The lab setup consists of a measurement cabinet with a power supply in the bottom, and a measurement chamber with the inverter and a Teledyne LeCroy HDO8058 oscilloscope for recording of the device voltages and currents. Furthermore, two inductors that are placed in series with a total inductance of 420 µH are located in the left side of the cabinet. Moreover, a Field Programmable Gate Array (FPGA) that controls the switches is located on the right side of the chamber. This FPGA is connected to a lab PC shown in the right of the picture, which runs a Matlab based control and acquisition tool where the measurement points are entered and where all data is automatically recorded.
The power stage of the inverter is shown in Fig. 4.24. The logic board with gate drivers is not shown as it is normally screwed on top of the IGBT modules.
The collector and emitter potentials of the IGBT modules are connected to a PMK BumbleBee differential voltage probe with ±0.35% accuracy of the reading [D4]. Furthermore, a CWTUM/3/R Rogowski coil from PEM is installed for measurements of the collector current $i_{\mathrm{C}}(t)$ and diode current $i_{\mathrm{D}}(t)$. The accuracy of this current sensor is ±2% of the reading [D5], assuming that the current busbar cannot be placed exactly in the center of the sensor coil. Hence, the total accuracy of the switching energy is ±2.35% of the reading.

Figure 4.23: Test bench for double pulse method with installed inverter.

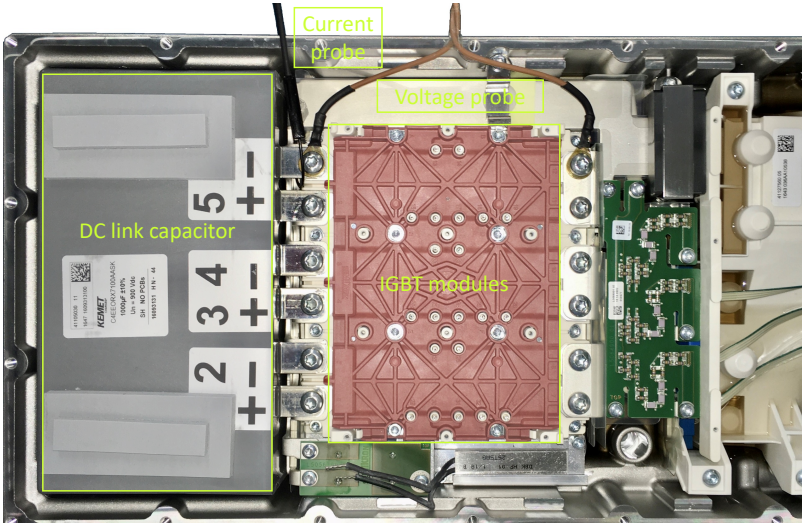

Figure 4.24: Inverter power stage with current sensor and voltage measurement points.

The switching energies are measured for four out of six transistors with representative DC voltages and load currents. The three bottom semiconductors, S2, S4, and S6 are measured to identify the spread between the three phases. Furthermore, S5 is measured to identify the spread between an upper and lower semiconductor pair. Typical switching waveforms at a load current of 8 A and a DC voltage of 375 V are for the turn on, turn off, and reverse recovery behavior of S4 presented in Fig. 4.25, Fig. 4.26, and Fig. 4.27 respectively. It is shown in Fig. 4.26 that the voltage overshoot caused by the stray inductance during the turn off event is very minimal. This is partly due to the low current and voltage and most likely also a result of a snubber circuit in order to limit the voltage overshoot.
The spread in switching energies between the four measured switches is for a voltage of 350 V plotted in Fig. 4.28 for E_{on}, in Fig. 4.29 for E_{off}, and in Fig. 4.30 for E_{rr} respectively. The spread between the switches is minor, especially between the upper and lower semiconductor. As a result, the average values of the three bottom switches are used in all switching loss calculations for all analyzed charging concepts. These average switching energies are plotted as function of voltage and current in Fig. 4.31, Fig. 4.32, and Fig. 4.33 for respectively E_{on}, E_{off}, and E_{rr}.

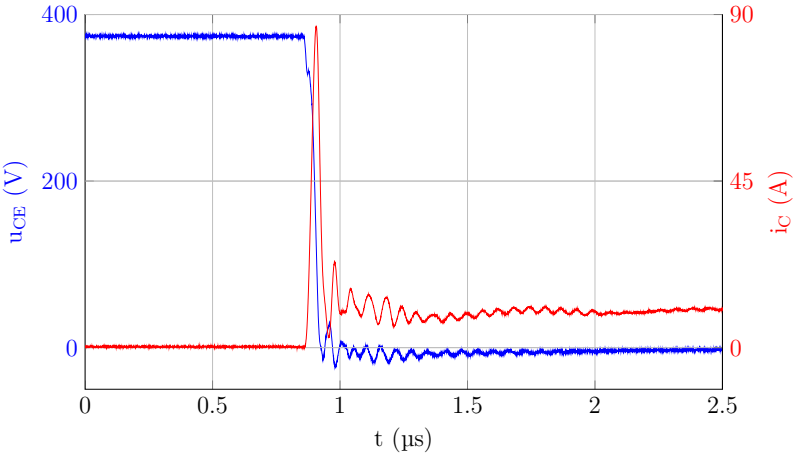

Figure 4.25: Transistor S4 turn on behavior with $u_{\text{CE}}(t)$ in blue and $i_{\text{C}}(t)$ in red.

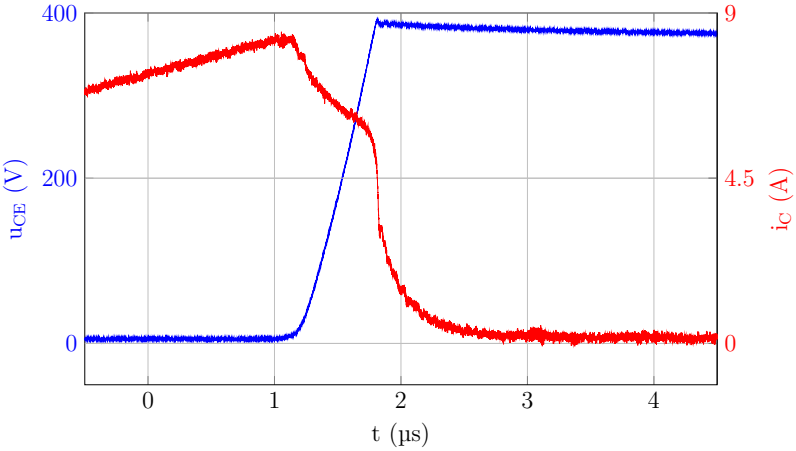

Figure 4.26: Transistor S4 turn off behavior with $u_{CE}(t)$ in blue and $i_C(t)$ in red.

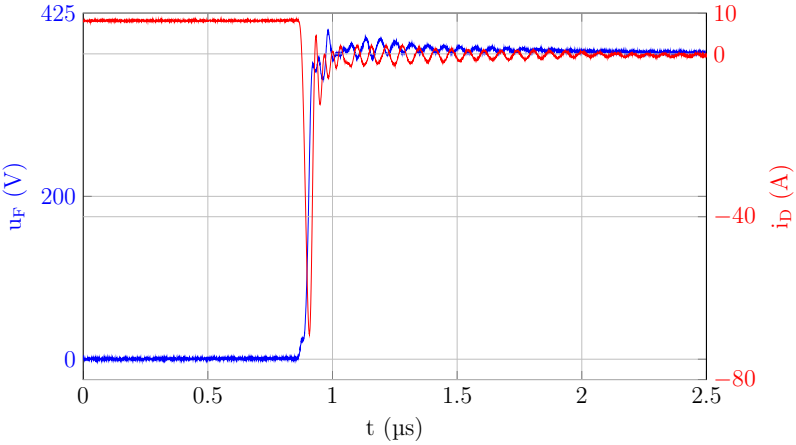

Figure 4.27: Diode S4 reverse recovery behavior with $u_F(t)$ in blue and $i_D(t)$ in red.

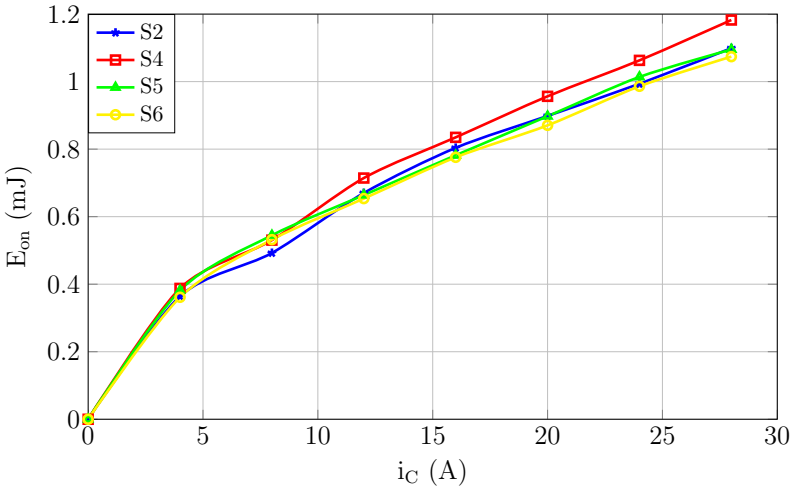

Figure 4.28: Spread in turn on energy at 350 V.

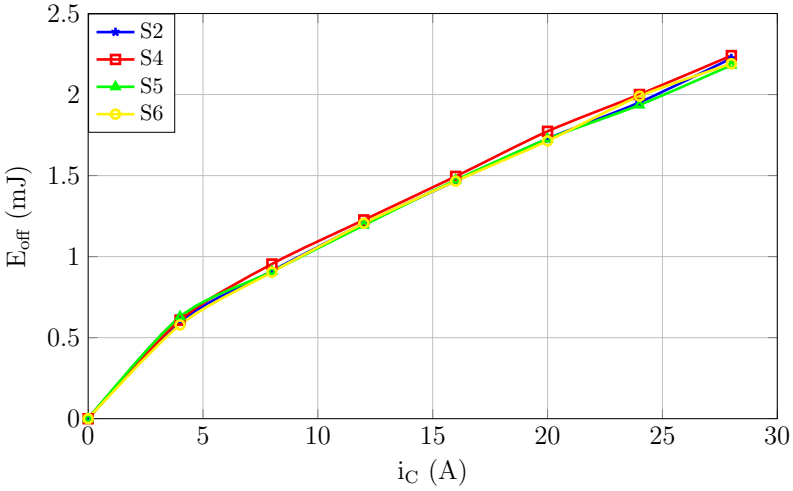

Figure 4.29: Spread in turn off energy at 350 V.

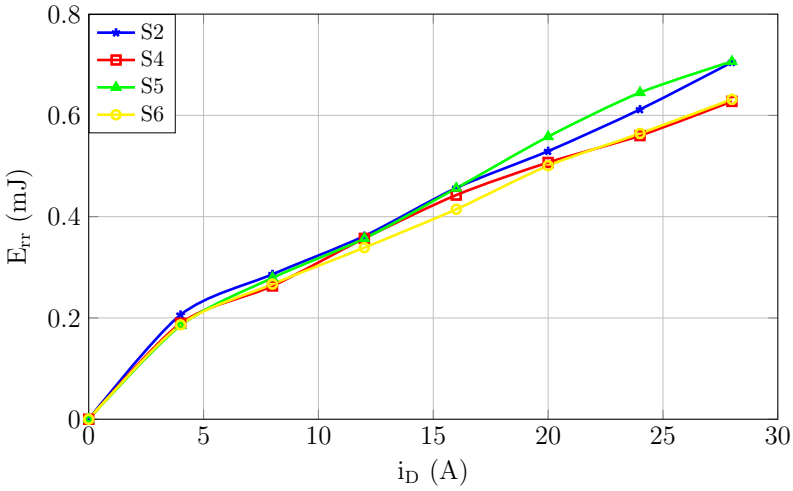

Figure 4.30: Spread in reverse recovery energy at 350 V.

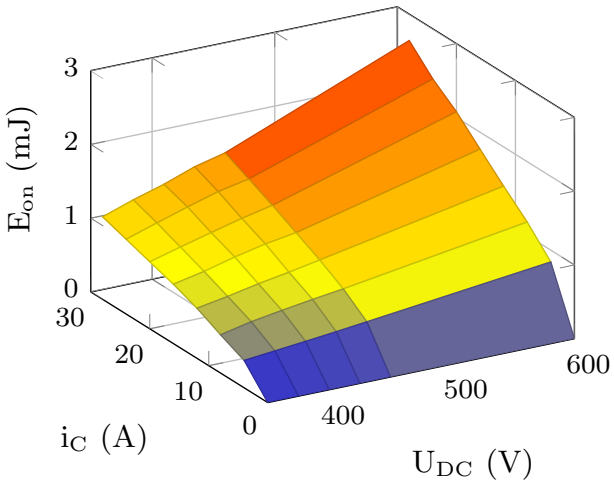

Figure 4.31: Turn on energy under charging conditions.

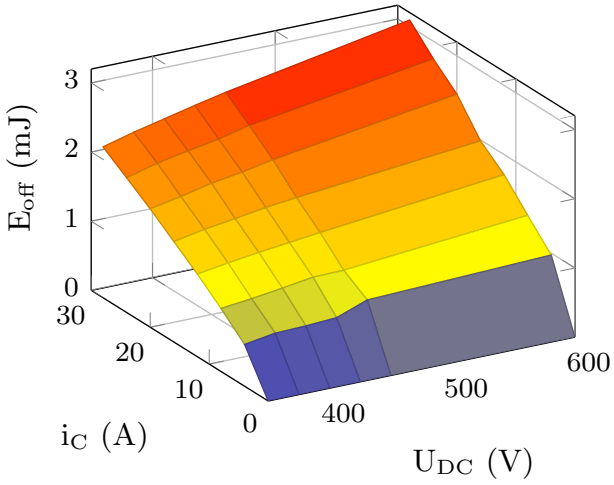

Figure 4.32: Turn off energy under charging conditions.

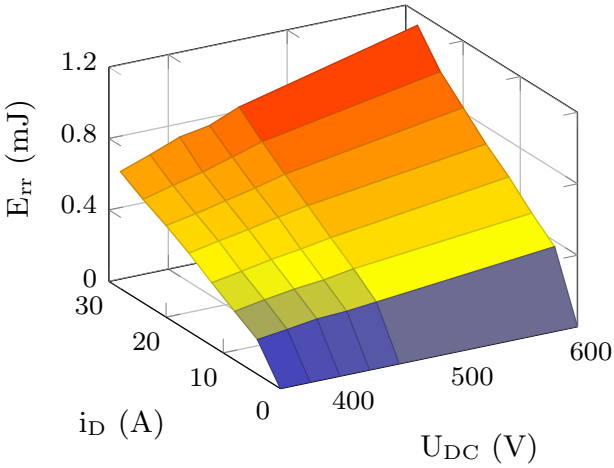

Figure 4.33: Diode reverse recovery energy under charging conditions.

5

Novel Boost-Buck Series Connected Integrated Chargers

As mentioned in chapter 1, battery chargers should contain both voltage step up and step down functionality to support the entire battery voltage range. With the anticipation that non-isolated coupled chargers tend to achieve better efficiency levels than the isolated charger from chapter 3, possible non-isolated charger concepts with boost and buck functionality are derived from state of the art integrated chargers. Two highly efficient novel concepts are introduced in this chapter and provide galvanically coupled integrated charging across a wide battery voltage range without generation of shaft torque. A novel general concept for non-isolated chargers that provides step up and step down functionality is introduced in section 5.1. Thereafter, two concepts are derived from state of the art reconnection variants as discussed in chapter 2 and are described in detail in section 5.2. Afterwards, mathematical modeling of the EM winding voltages and currents is provided in section 5.3. Experimental implementation and first proof of concept results based on the SCIM and power electronics as described in chapter 4 are presented in section 5.4. Moreover, detailed loss and efficiency analysis based on simulations and measurement is reported in section 5.5. Finally, alternative methods to protect against electric

shock during charging are reviewed in section 5.6 since galvanic isolation is avoided.

5.1 Proposed Boost-Buck Integrated Charger

The reviewed basic reconnection methods from chapter 2 that form integrated chargers using a standard three-phase EM are summarized in Tab. 5.1. As previously concluded, none of the discussed reconnection variants of a standard three-phase e-drive have the possibility to operate both as a high efficient boost PFC rectifier and as a buck converter simultaneously unless shaft torque is generated and reconnection switches are needed like in the separate winding concept, or with the need of an AC/DC converter as in the B4-B2 concept. Therefore, it might be better to perform either buck or boost PFC functionality in a three-phase stage. To combine both boost and buck functionality, it might be worth to investigate possibilities for series connection of two three-phase sets of a 2x3 phase drive system.

EM use	**Grid type**	**Function**	**Torque possible**	**Extra hardware**	**Series useful**
Y	single-phase	PFC or buck	yes	switch	yes
W	single-phase	PFC or buck	no	diode rectifier	yes
Open end	three-phase	PFC or buck	yes	switch	yes
Separate	single-phase	PFC & buck	yes	switch	no
B4-B2	DC	Buck-boost	no	PFC switch	no

Table 5.1: Reconnections of three-phase drive systems as a charger.

A series connection of two three-phase electrical drive systems as illustrated in Fig. 5.1 is proposed as a solution for increased battery voltage flexibility. This can easily be achieved when a 2x3-phase drive system with two accessible neutral points, N1 and N2, is used. This concept has been published in [E2]. Furthermore, a patent has been filed for this novel idea [E7]. Note that the 2x3 phase e-drive does not need to be mechanically integrated into one housing, it can also comprise two separate three-phase drive systems that are connected in series during charging. Hence, it is for example possible to utilize the front

and rear wheel drive systems of a vehicle with two drive axles together as an integrated charger. The advantage of the proposed concept in contrast to the buck-boost variant using a three-phase EM is that no expensive reconnection devices are required. Furthermore, it is possible to provide battery charging without generation of shaft torque when the favorable winding connection is chosen. Possible winding reconnections for charging mode of the 2x3-phase e-drive are derived from those reference three-phase winding reconnections that are identified as series useful 'yes' in the last column of Tab. 5.1.

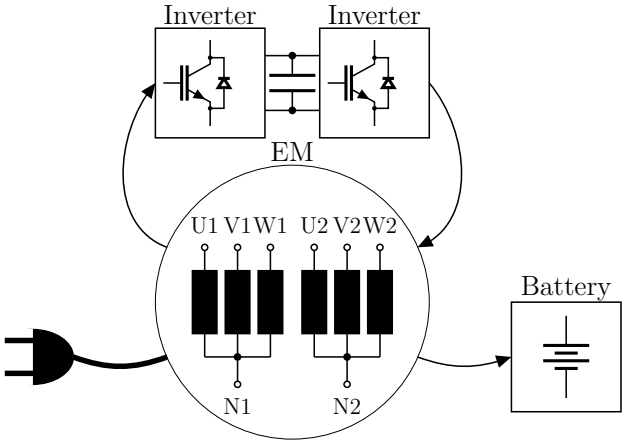

Figure 5.1: Novel non-isolated integrated charging concept.

5.2 Derivation of Hardware Reconnection Variants

The boost-buck series connection can be created by connecting the Y, W, or open end variants of Tab. 5.1 in series with the mirror of each variant, which theoretically provides 3^2=9 topologies that are summarized in Tab. 5.2. Note that the open end concept should be connected via the neutral point to the battery when used as a buck converter, and is thus identical to the W concept for step down conversion. Hence, any concept with the open end winding concept as buck converter can be eliminated and thus, six variants remain available. By elimination of the open end and Y concepts as boost converter to avoid any

potential shaft torque, two variants remain possible: the WY connected and the WW connected integrated charger. These concepts are presented in Fig. 5.2 and Fig. 5.3 respectively. Note that each EM winding system represents one half of the 2x3 phase EM.

	Battery side		
Grid side	**Y**	**W**	**Open end**
Y	motion	motion	motion
W	standstill	standstill	standstill
Open end	motion	motion	motion

Table 5.2: Six-phase drives as boost-buck converter.

Both concepts require a simple single-phase diode bridge rectifier and an Electro Magnetic Interference (EMI) filter for grid connection and filtering of harmonics respectively. Furthermore, a reconnection switch is required for connection of the converter output to the battery. A switch rated for charging currents is sufficient for the WW concept. On the other hand, a switch that withstands the traction phase current is required for the WY concept.

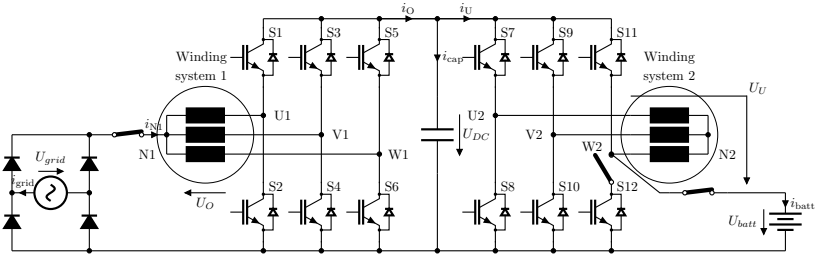

Figure 5.2: WY connected integrated charger.

5.3 Theoretical Modeling

Analytical description of the e-drive voltages and currents as a boost-buck converter with interaction between the windings is provided for a 2x3-phase EM, thus with coupling between the boost and buck windings. This description forms

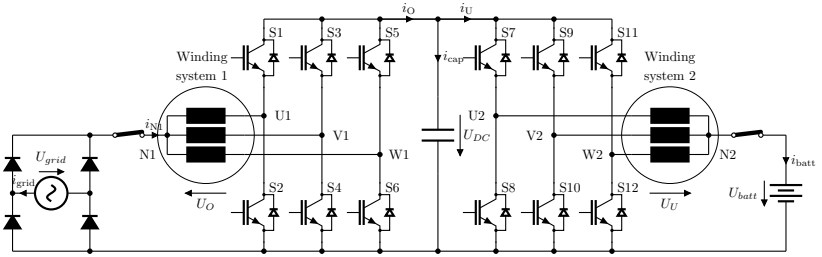

Figure 5.3: WW connected integrated charger.

a foundation for the loss simulations under charging condition. Furthermore, it is verified that the concepts remain at standstill during charging. Finally, the control system is described. Note that phase V2 is connected to the battery in all theoretical and practical analyses of the WY concept, even though phase W2 is connected to the battery in Fig. 5.2 for illustration simplification.

5.3.1 Voltage Equations

Standard operating principles of boost and buck converter voltage input to output ratio as defined per duty cycle D apply to both concepts. In other words, the boost inductor voltage is defined as

$$u_{\mathrm{O}} = \begin{cases} -\left|U_{\mathrm{grid}}\right| & 0 < t < DT_{\mathrm{s}} \\ U_{\mathrm{DC}} - \left|U_{\mathrm{grid}}\right| & DT_{\mathrm{s}} < t < T_2 \\ 0 & T_2 < t < T_{\mathrm{s}} \end{cases} \tag{5.1}$$

assuming Discontinuous Conduction Mode (DCM) at least around the zero crossing of the grid current. The buck winding voltage is defined with two states assuming Continuous Conduction Mode (CCM):

$$u_{\mathrm{U}} = \begin{cases} U_{\mathrm{DC}} - U_{\mathrm{batt}} & 0 < t < DT_{\mathrm{s}} \\ -U_{\mathrm{batt}} & DT_{\mathrm{s}} < t < T_{\mathrm{s}} \end{cases}. \tag{5.2}$$

Note that the boost voltages are referenced as negative, since the boost current flows from the neutral point to the phase connections. These defined voltage states are used to solve the general voltage equation for an EM at standstill

$$\underline{u_\mathrm{s}} = \underline{R} \cdot \underline{i_\mathrm{s}} + \frac{d}{dt}\underline{L} \cdot \underline{i_\mathrm{s}}. \tag{5.3}$$

In the WW concept, each winding is directly connected between two defined voltages, e.g. the rectified grid voltage, DC link capacitor voltage, or the battery voltage. Therefore, each parallel EM phase of the W connection sees an identical voltage. Hence, each phase voltage of the WW concept is identical to the voltage of the regular states of a boost or buck converter. Thus, the EM voltage matrix is defined as

$$\underline{u_\mathrm{s}} = \begin{bmatrix} u_\mathrm{u1} \\ u_\mathrm{v1} \\ u_\mathrm{w1} \\ u_\mathrm{u2} \\ u_\mathrm{v2} \\ u_\mathrm{w2} \end{bmatrix} = \begin{bmatrix} u_\mathrm{O} \\ u_\mathrm{O} \\ u_\mathrm{O} \\ u_\mathrm{U} \\ u_\mathrm{U} \\ u_\mathrm{U} \end{bmatrix}. \tag{5.4}$$

The winding currents are defined as

$$\underline{i_\mathrm{s}} = \begin{bmatrix} i_\mathrm{u1} & i_\mathrm{v1} & i_\mathrm{w1} & i_\mathrm{u2} & i_\mathrm{v2} & i_\mathrm{w2} \end{bmatrix}^\top. \tag{5.5}$$

Furthermore, the resistance matrix is for the WW concept defined as

$$\underline{R} = \begin{bmatrix} R_\mathrm{ph} & 0 & 0 & 0 & 0 & 0 \\ 0 & R_\mathrm{ph} & 0 & 0 & 0 & 0 \\ 0 & 0 & R_\mathrm{ph} & 0 & 0 & 0 \\ 0 & 0 & 0 & R_\mathrm{ph} & 0 & 0 \\ 0 & 0 & 0 & 0 & R_\mathrm{ph} & 0 \\ 0 & 0 & 0 & 0 & 0 & R_\mathrm{ph} \end{bmatrix} \tag{5.6}$$

and the differential inductance matrix as

$$\underline{L} = \begin{bmatrix} L_{\mathrm{u1u1}} & L_{\mathrm{u1v1}} & L_{\mathrm{u1w1}} & L_{\mathrm{u1u2}} & L_{\mathrm{u1v2}} & L_{\mathrm{u1w2}} \\ L_{\mathrm{v1u1}} & L_{\mathrm{v1v1}} & L_{\mathrm{v1w1}} & L_{\mathrm{v1u2}} & L_{\mathrm{v1v2}} & L_{\mathrm{v1w2}} \\ L_{\mathrm{w1u1}} & L_{\mathrm{w1v1}} & L_{\mathrm{w1w1}} & L_{\mathrm{w1u2}} & L_{\mathrm{w1v2}} & L_{\mathrm{w1w2}} \\ L_{\mathrm{u2u1}} & L_{\mathrm{u2v1}} & L_{\mathrm{u2w1}} & L_{\mathrm{u2u2}} & L_{\mathrm{u2v2}} & L_{\mathrm{u2w2}} \\ L_{\mathrm{v2u1}} & L_{\mathrm{v2v1}} & L_{\mathrm{v2w1}} & L_{\mathrm{v2u2}} & L_{\mathrm{v2v2}} & L_{\mathrm{v2w2}} \\ L_{\mathrm{w2u1}} & L_{\mathrm{w2v1}} & L_{\mathrm{w2w1}} & L_{\mathrm{w2u2}} & L_{\mathrm{w2v2}} & L_{\mathrm{w2w2}} \end{bmatrix}. \tag{5.7}$$

However, in the WY converter, the voltages of the secondary phases, i.e. those used in the step down converter, are not explicitly defined as the neutral point is floating rather than connected to a defined voltage. Instead, the phase voltages are dependent on the resistive and inductive ratios between the secondary EM phases as windings U2 and W2 are connected in parallel to phase V2 in series. Hence, the current in phase V2 is opposite to the sum of that in U2 and W2 and the voltage drop across phase W2 is identical to that over winding U2. Summarized in equations, there are two conditions defined by the Y connection of the buck converter:

$$u_{\mathrm{u2}} = u_{\mathrm{w2}} = u_{\mathrm{U}} + u_{\mathrm{v2}} \tag{5.8}$$

and

$$i_{\mathrm{v2}} = -(i_{\mathrm{u2}} + i_{\mathrm{w2}}). \tag{5.9}$$

As a result, the voltage condition (5.8) implies a shortened voltage vector:

$$\underline{u}_{\mathrm{s}} = \begin{bmatrix} u_{\mathrm{u1}} \\ u_{\mathrm{v1}} \\ u_{\mathrm{w1}} \\ u_{\mathrm{u2}} - u_{\mathrm{v2}} \\ u_{\mathrm{w2}} - u_{\mathrm{v2}} \end{bmatrix} = \begin{bmatrix} u_{\mathrm{O}} \\ u_{\mathrm{O}} \\ u_{\mathrm{O}} \\ u_{\mathrm{U}} \\ u_{\mathrm{U}} \end{bmatrix}. \tag{5.10}$$

The current condition (5.9) also implies a shortened current vector:

$$\underline{i}_{\mathrm{s}} = \begin{bmatrix} i_{\mathrm{u1}} & i_{\mathrm{v1}} & i_{\mathrm{w1}} & i_{\mathrm{u2}} & i_{\mathrm{w2}} \end{bmatrix}^{\top} \tag{5.11}$$

Therefore, the resistance and inductance matrices are reduced from a 6×6 to a 5×5 matrix system by applying the two above mentioned conditions. As a result, the resistance matrix R becomes

$$\underline{R} = \begin{bmatrix} R_{\mathrm{ph}} & 0 & 0 & 0 & 0 \\ 0 & R_{\mathrm{ph}} & 0 & 0 & 0 \\ 0 & 0 & R_{\mathrm{ph}} & 0 & 0 \\ 0 & 0 & 0 & 2R_{\mathrm{ph}} & R_{\mathrm{ph}} \\ 0 & 0 & 0 & R_{\mathrm{ph}} & 2R_{\mathrm{ph}} \end{bmatrix}. \tag{5.12}$$

Furthermore, the differential inductance matrix L is rewritten to

$$\underline{L} = \begin{bmatrix} L_{\mathrm{u1u1}} & L_{\mathrm{u1v1}} & L_{\mathrm{u1w1}} & \cdots & L_{\mathrm{u1u2}} - L_{\mathrm{u1v2}} & L_{\mathrm{u1w2}} - L_{\mathrm{u1v2}} \\ L_{\mathrm{v1u1}} & L_{\mathrm{v1v1}} & L_{\mathrm{v1w1}} & \cdots & L_{\mathrm{v1u2}} - L_{\mathrm{v1v2}} & L_{\mathrm{v1w2}} - L_{\mathrm{v1v2}} \\ L_{\mathrm{w1u1}} & L_{\mathrm{w1v1}} & L_{\mathrm{w1w1}} & \cdots & L_{\mathrm{w1u2}} - L_{\mathrm{w1v2}} & L_{\mathrm{w1w2}} - L_{\mathrm{w1v2}} \\ L_{\mathrm{u2u1}} - L_{\mathrm{v2u1}} & L_{\mathrm{u2v1}} - L_{\mathrm{v2v1}} & L_{\mathrm{u2w1}} - L_{\mathrm{v2w1}} & \cdots & L_{\mathrm{u2u2}} - L_{\mathrm{v2u2}} - L_{\mathrm{u2v2}} + L_{\mathrm{v2v2}} & L_{\mathrm{u2w2}} - L_{\mathrm{v2w2}} - L_{\mathrm{u2v2}} + L_{\mathrm{v2v2}} \\ L_{\mathrm{w2u1}} - L_{\mathrm{v2u1}} & L_{\mathrm{w2v1}} - L_{\mathrm{v2v1}} & L_{\mathrm{w2w1}} - L_{\mathrm{v2w1}} & \cdots & L_{\mathrm{w2u2}} - L_{\mathrm{v2u2}} - L_{\mathrm{w2v2}} + L_{\mathrm{v2v2}} & L_{\mathrm{w2w2}} - L_{\mathrm{v2w2}} - L_{\mathrm{w2v2}} + L_{\mathrm{v2v2}} \end{bmatrix}. \tag{5.13}$$

The currents i_{N1} and i_{batt} through the EM neutral points of the boost and buck converter respectively are for the WW and WY concepts analytically calculated using the above equations (5.1)–(5.13). The results are plotted in Fig. 5.4 for the WW concepts and in Fig. 5.5 for the WY concept, both for a charging power of 6.6 kW, a switching frequency of 15 kHz, a DC link voltage of 375 V, and a battery voltage of 350 V. A time interval of 10 ms is chosen, as this is the periodical interval of the rectified 230 V 50 Hz single-phase AC grid.

5.3.2 Shaft Torque

As previously described, a W connection does not generate shaft torque thanks to its balanced winding current. Furthermore, only an initial alignment torque

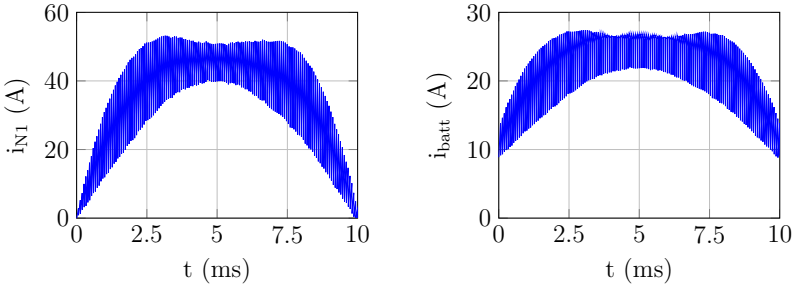

(a) (b)

Figure 5.4: Calculated EM neutral point currents for the WW concept in (a) boost converter and (b) buck converter.

is generated in the Y concept if a DC current is present, like on the battery side. Hence, no torque is expected for the WW and WY concepts during charging. Verification of the zero torque assumption is analyzed with the Bosch in-house FEM tool using the currents as plotted in Fig. 5.4 and Fig. 5.5. The resulting torque ripple is presented in Fig. 5.6. Only a slight torque ripple of less than 0.04% of the peak torque of 270 Nm is introduced for the WY concept due to the unbalance in the EM inductances as a result of the Y connection of the buck windings. The generated torque of the WW concept is a factor 100 lower thanks to the balanced winding currents in the buck windings. These low levels of torque ripple are significantly below the stiction torque of the shaft and wheels and should thus not lead to shaft motion even if no parking brake is applied.

5.3.3 Control System

The WW and WY charger topologies consist of two defined voltages and one defined current: the grid and battery voltages U_{grid} and U_{batt} are prescribed by respectively the AC grid and the battery. Furthermore, the capacitor current i_{cap} of the DC link capacitor is defined by Kirchhoff's current law as the difference between the output current i_{O} from the boost converter and the current i_{U} flowing into the battery connected buck converter:

$$i_{\text{cap}} = i_{\text{O}} - i_{\text{U}}. \tag{5.14}$$

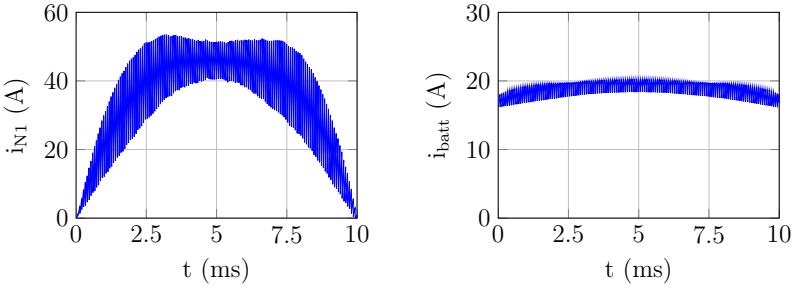

(a) (b)

Figure 5.5: Calculated EM neutral point currents for the WY concept in (a) boost converter and (b) buck converter.

Hence, there are three parameters to be controlled: the grid current i_{grid} to maintain unity Power Factor (PF), the battery current i_{batt} to maintain the requested battery charging power P^*_{batt}, and the DC link voltage U_{DC} to prevent over voltages in the DC link capacitor. Therefore, a control strategy as reported in [88] is suggested. Both inverters are operated in current control mode: the inverter and EM windings connected to the battery are used to control the battery current, and the grid connected inverter is used as a boost PFC converter of the grid current. This current waveform follows the rectified grid voltage waveform to maintain unity power factor and the peak value reflects the current needed to stabilize the DC link voltage to a reference level U^*_{DC}. Hence, the reference grid current i^*_{grid} is determined by a third controller: the DC link voltage controller. Moreover, a feed forward term of the battery current reference i^*_{batt} is used as a second input to the grid current controller for enhanced controller performance. The reference DC link voltage U^*_{DC} is chosen based on minimum need for the grid and battery and may be optimized to reduce the total system losses. Moreover, the actual DC link voltage has a sinusoidal component u_{C} with twice the grid frequency for a single-phase rectified grid voltage. Therefore, sufficient voltage step buffer between the DC and the battery voltages is required. The exact level is derived by [S5]

$$u_{\text{C}} = \frac{i_{\text{cap,AC,pk}}}{C_{\text{DC}} 4\pi f_{\text{grid}}} \tag{5.15}$$

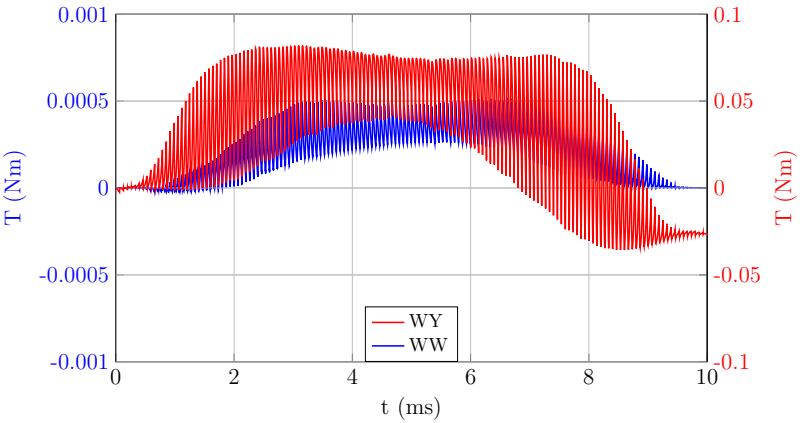

Figure 5.6: Simulated torque ripple.

where $i_{\text{cap,AC,pk}}$ is the AC peak value of grid component of the capacitor current i_{cap}, not reflecting the switching ripple. Since the inverters used to verify the non-isolated charger concepts contain a relatively large DC link capacitor C_{DC}, a difference of 25 V between DC link and battery is sufficient. To accommodate for inverters with smaller capacitors such as those in passenger car vehicles, the losses efficiency analysis of the system as reported in section 5.5 are also analyzed at a 50 V difference between U_{DC} and U_{batt}. Practical realization of the DC link voltage reference U^*_{DC} might for example be implemented with a predefined Look-Up Table (LUT). A schematic overview of the control strategy is presented in Fig. 5.7. The control parameters are reported in [S5] and are based on the calculations provided in [89].

5.4 Implementation

The WW and WY concepts have been implemented using the 144 kW SCIM and two Semikron SKAI2 inverters as described in chapter 4 to operate as a single-phase non-isolated integrated battery charger. These inverters contain a capacitance of 1 mF each, thus the total DC capacitance C_{DC} equals 2 mF. Power conversion from a single-phase 230 V 50 Hz AC source is assessed for battery voltages between 300 and 400 V DC. The hardware setup is presented in

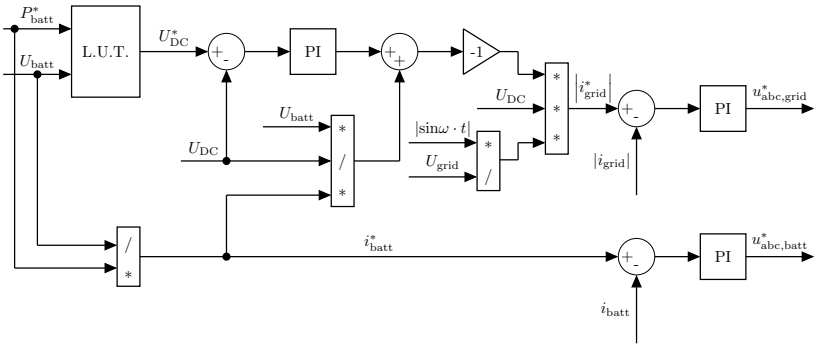

Figure 5.7: Control strategy for the proposed concepts.

paragraph 5.4.1. Furthermore, the power quality requirements such as the Total Harmonic Distortion (THD) and PF are assessed in paragraph 5.4.2.

5.4.1 Hardware Setup

A test setup as reported in [E2, E3, S5] and presented in Fig. 5.8 was used for system measurements of the WW and WY concepts. In addition to the previously described SCIM and Semikron inverters, 600 V diodes from Microsemi [D6] are used as a single-phase bridge rectifier. Eight diodes are used to simplify the mechanical installation of the four two-packs. The inverters and EM are WEG cooled and the diode rectifier is passively cooled using a large heatsink. Furthermore, the EM windings have been brought out to a reconnection board in order to facilitate reconnection between the WW and WY concepts. Phase W2 is located on the back side of the terminal board, all other phases are located on the front.
The operating points for evaluation included battery voltages between 300-400 V and switching frequencies of 10, 15, and 20 kHz. The reference DC link voltage U^*_{DC} was set to 25 V above the battery voltage U_{batt}, with a minimum of 350 V to accommodate some fluctuations of the 50 Hz 230 V grid voltage. The charging power equals 6.6 kW for all analyses unless stated otherwise.
The control system as explained in paragraph 5.3.3 has been implemented in dSPACE Autobox DS1005 Real Time Interface hardware that is controlled with the dSPACE ControlDesk software on a regular PC. This setup uses a Matlab

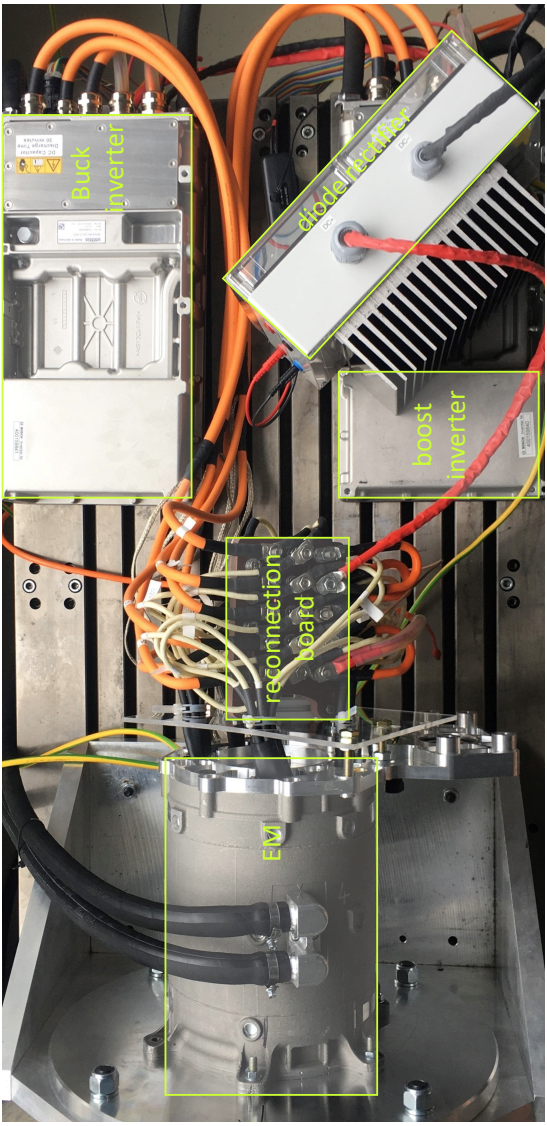

Figure 5.8: Test setup for the WW and WY concepts.

Simulink based model that is programmed into a DS5202 AC Motor Control Solution FPGA base board from dSPACE that is located inside the Autobox. This FPGA board contains implementation of the Proportional Integral (PI) voltage and current controllers and contains dSPACE specific blocks for generation and communication of the Pulse Width Modulation (PWM) signals $u^*_{\mathrm{abc,grid}}$ and $u^*_{\mathrm{abc,batt}}$ via digital outputs to the inverters. Furthermore, the grid voltage is captured with an Analog to Digital Converter (ADC) in order to follow its phase angle with the boost PFC converter. Moreover, the actual inverter phase currents and the DC link voltage are read into the dSPACE system and are used to determine the errors for the current and voltage controllers.
In addition to the e-drive and the control system, two series-connected four quadrant laboratory power supplies of type SM 500-CP-90 from Delta Elektronika are used to simulate the battery voltage. Furthermore, the grid voltage is simulated with a customized 40 kVA AC voltage source from Heiden that can simulate single- and three-phase grids up to 46 A phase current, voltages of 10-500 V, and frequencies of 40-70 Hz. The setup was set to provide the single-phase AC grid voltage. A schematic overview of the test setup is provided in Fig. 5.9. In addition to the system measurements, several loss measurements have been performed with only three out of six phases as a buck converter. In this case, a Regatron TopCon TC.GSS.32.500 is used as a DC voltage source. Some first results have been published in [E2, S6]. More detailed measurements have been reported in [E3, E4, S5].

5.4.2 Power Quality Measurements

As discussed in paragraph 5.3.3, there are three parameters to be controlled: the grid current i_{grid}, DC link voltage U_{DC}, and the battery current i_{batt}. The experimental verification of the control system is reported in this paragraph. The measured grid and battery currents and the DC link voltages of the WW and WY concept are plotted in respectively Fig. 5.10 and Fig. 5.11 for a switching frequency of 10 kHz, a reference DC link voltage of 375 V, and a battery voltage of 350 V. The current ripple on the battery side is in the WW concept significantly larger than in the WY concept. This is a result of the higher buck inductance in the WY concept than in the WW concept. Moreover, it is shown that the increased ripple of the battery current even has some effect on the grid current due to the coupling between the primary and secondary winding set. This influence depends on the coupling of the two winding sets and is thus dependent on the EM layout. An enlarged zoom of the grid currents near the zero crossing of the grid voltage is plotted in Fig. 5.12. It is shown that boost

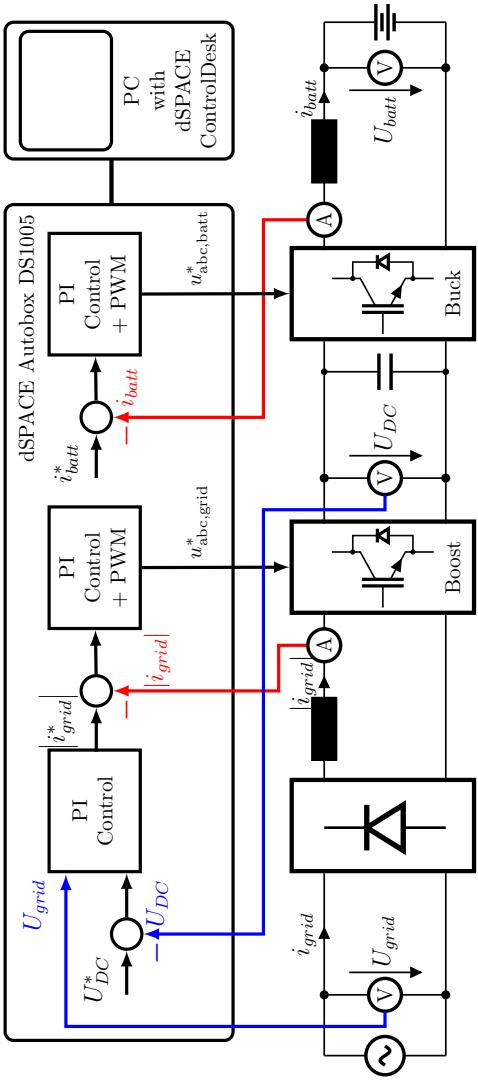

Figure 5.9: Schematic overview of test setup for the WW and WY concepts.

conductor is in DCM around the zero crossing of the grid current as the current reaches zero during multiple switching time periods. In addition to the grid current, the switching ripple of the battery current is presented in Fig. 5.13. There is an influence of the grid current on the battery ripple, due the coupling between the primary and the secondary winding sets.
Two important measures for power quality of grid connected devices are PF and THD. Each grid connected device has to fulfill the requirements in terms of PF and THD. The power factor requirements are specified in [6], which are split in the Displacement Power Factor (PF_{disp}) and the Distortion Power Factor (PF_{dist}). PF_{dist} identifies the ratio between active and apparent power for the fundamental frequency of the grid. PF_{dist} equals the ratio of fundamental current to the total current, and is thus related to the THD by:

$$PF_{\text{dist}} = \frac{1}{\sqrt{1+THD^2}}. \tag{5.16}$$

The total power factor PF is the product of both components. The values are measured for the WW and WY concepts for a 6.6 kW load at a battery voltage of 300 V with a switching frequency of 10 kHz and are listed together with the requirements in Tab. 5.3. It is shown that both concepts fulfill all PF requirements.

Parameter	**Requirement (%)**	**WW (%)**	**WY (%)**
THD	<23	7.16	7.92
PF_{dist}	>95	99.74	99.69
PF_{disp}	>90	97.64	97.03
PF	>85.5	97.39	96.73

Table 5.3: Power Quality results.

A common norm for the THD requirements is IEC61000-3 [90], which specifies the maximum allowed harmonic contents for each of the first thirteen harmonics of the grid frequency as well as a maximum sum for the first 40 harmonics of 23%. The charger's capability to preserve the harmonic content within the norm limits is important, as a failure to do so might lead to additional boost inductors in series to the EM windings, which will result in additional cost and weight. Therefore, it is desired that the norms are fulfilled with the charging concept without extra boost inductors. The THD has been assessed for various battery voltages and charging power levels. The THD as function

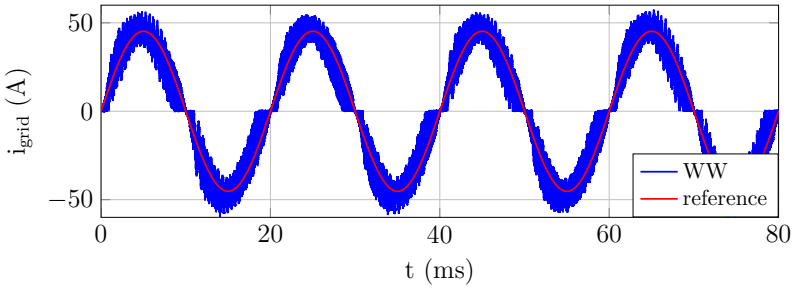

(a)

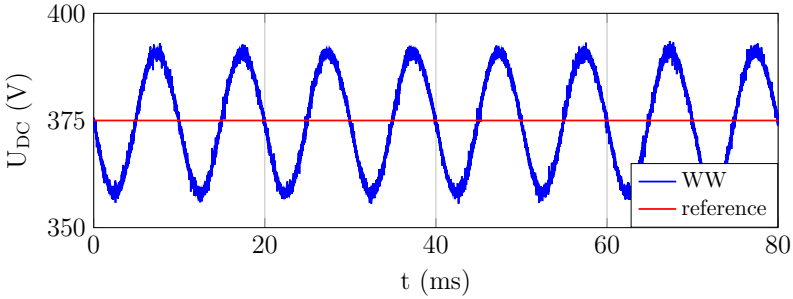

(b)

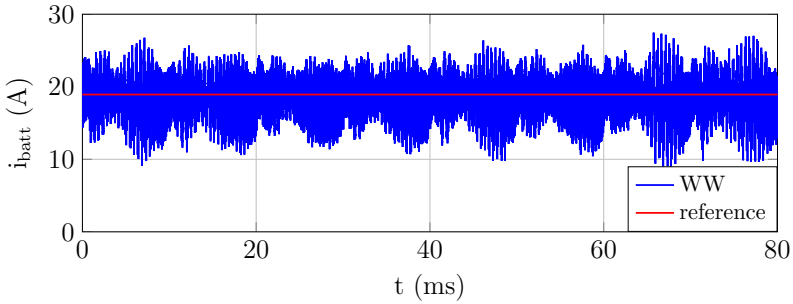

(c)

Figure 5.10: Measured values for the WW concept: (a) grid current, (b) DC link voltage, and (c) battery voltage.

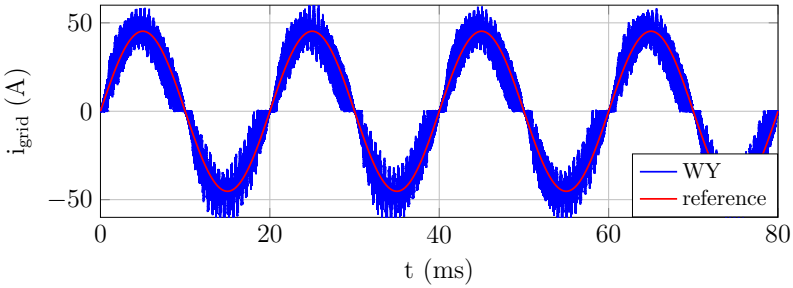

(a)

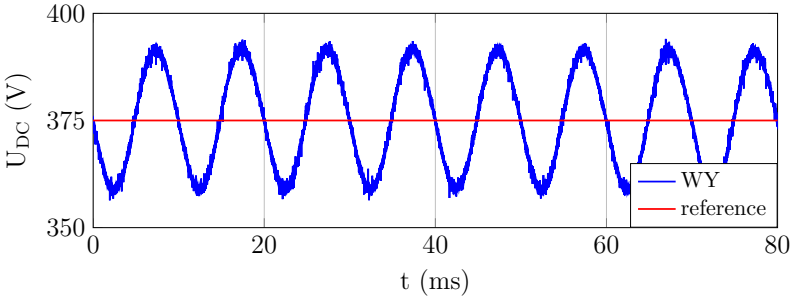

(b)

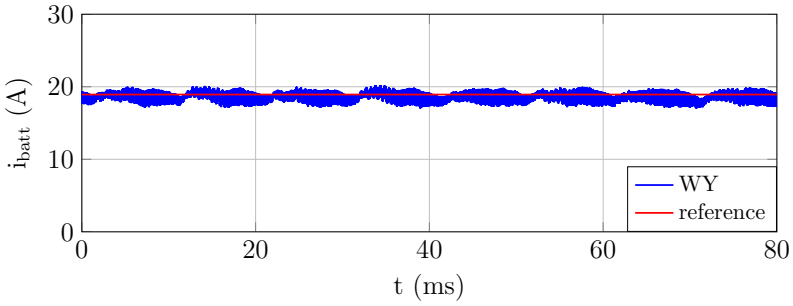

(c)

Figure 5.11: Measured values for the WY concept: (a) grid current, (b) DC link voltage, and (c) battery voltage.

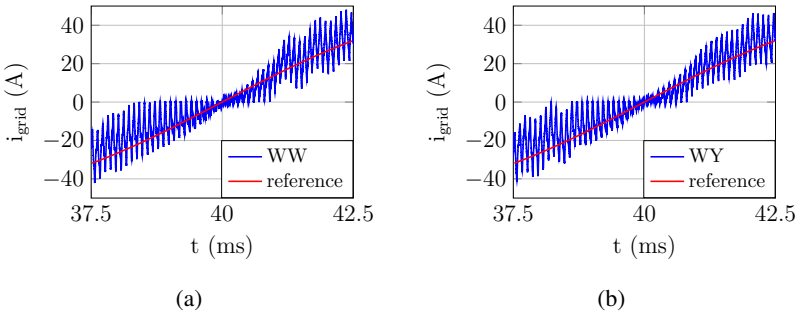

Figure 5.12: Measured grid currents zoomed in around zero crossing of grid voltage for (a) WW concept and (b) WY concept.

of the battery voltage is presented in Fig. 5.14 and Fig. 5.15 for the WW and the WY concepts respectively. Furthermore, THD as function of the charging power in Fig. 5.16 and Fig. 5.17 for both concepts. The THD requirements are met in all analyzed scenarios. In case another EM with smaller inductance would have been used and the THD requirements would not be met, it might be feasible to utilize interleaved switching for an improved effective inductance and thus lower harmonic content [25]. The effects of interleaved switching are not assessed since the used PWM generation modules in the dSPACE hardware support only one duty cycle per inverter and thus, do not allow a phase shift between multiple duty cycles of different inverter phases.

5.5 Losses and Efficiency Analysis

A detailed loss analysis for both concepts, based on the loss mechanisms identified in chapter 4, is presented in this section. Simulations are performed for battery voltages in 25 V intervals between 300 V and 400 V. Different DC voltages and switching frequencies of 10, 15, and 20 kHz are used to identify the efficiency behavior of the WW and WY concepts. Moreover, these simulation results are reviewed with measurements. As a matter of simplification of the loss calculations and measurements, the boost and buck converters were separately analyzed in simulations and measurements. This means that the inverter and EM windings used for step down conversion were disconnected for the boost measurements and vice versa. In simulations, the phase currents of the converter

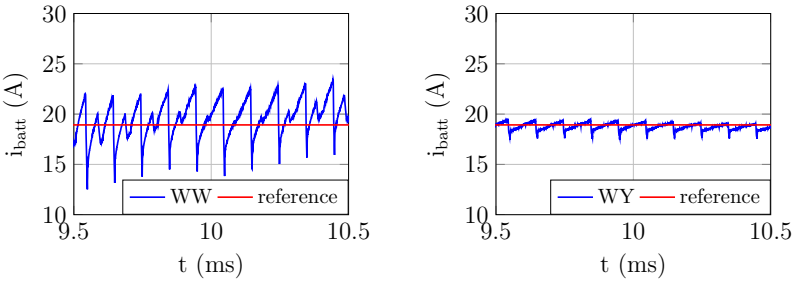

Figure 5.13: Measured battery current switching ripple for (a) WW concept and (b) WY concept.

that was not used is set to zero. The DC link voltage was in the measurements connected to the previously mentioned battery simulator for the boost and DC source for the buck converter. It is shown in Fig. 5.18 that the overall system efficiency closely follows the product of the efficiencies of the separated boost and buck converters [S5] and that the latter is at least not overestimating the total system efficiency. Thus, no significant differences or overestimations are expected between the efficiency numbers presented below based on the cascaded system and the ones measured with the entire system.
An LMG500 power analyzer from ZES Zimmer was used for all losses and efficiency measurements, in combination with the integrated voltage sensors and external IT 60-S Ultrastab current sensors from LEM. The measurement inaccuracy is up to ±1% of the measured efficiency [D7].

5.5.1 Non-isolated Charger Losses

Loss calculations and measurements for a 25 V delta between DC and battery voltage are illustrated in Fig. 5.19 and Fig. 5.20 for the WW and WY concept respectively at a charging power of 6.6 kW. The losses of the WW and WY concepts are for a 50 V difference plotted in Fig. 5.21 and Fig. 5.22 respectively. The labels '10', '15', and '20' in each plot denote the switching frequency in kHz. The total losses are relatively similar between the WW and WY concept, especially at a 25 V difference. The main difference in the loss distribution is that the Y connection causes larger copper losses in the buck winding. This

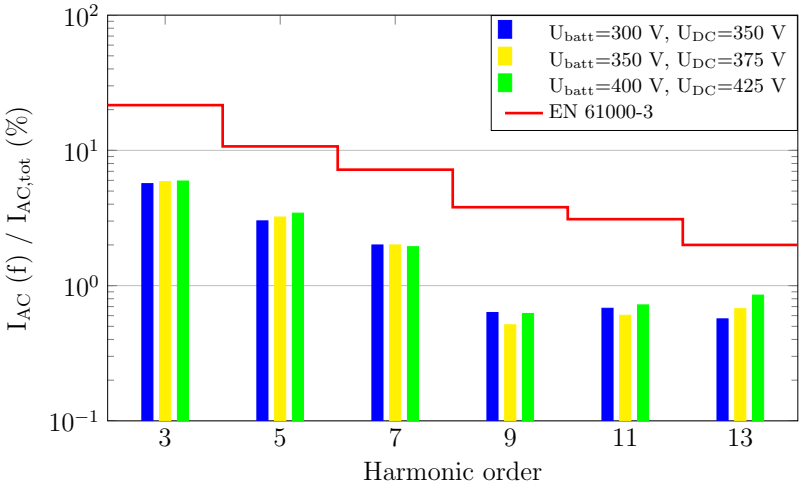

Figure 5.14: THD as function of battery voltage for WW.

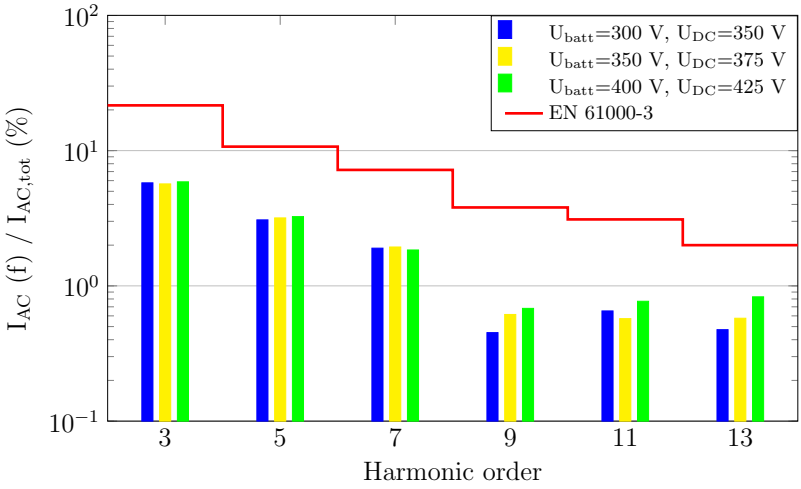

Figure 5.15: THD as function of battery voltage for WY.

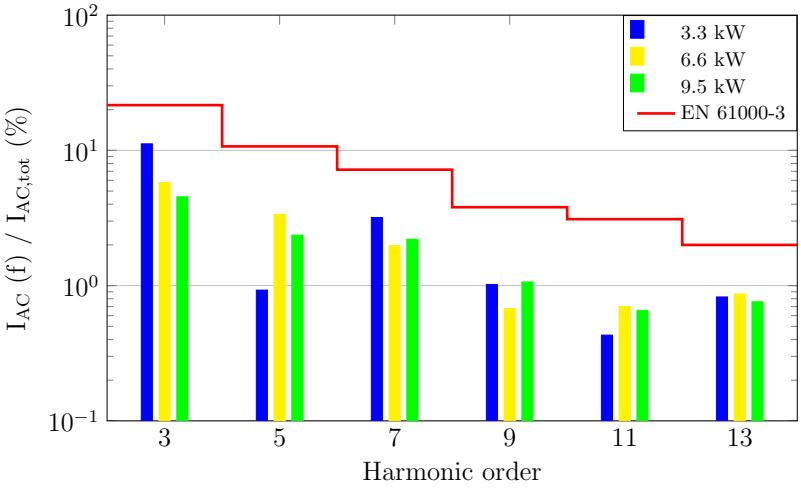

Figure 5.16: THD as function of charging power for WW.

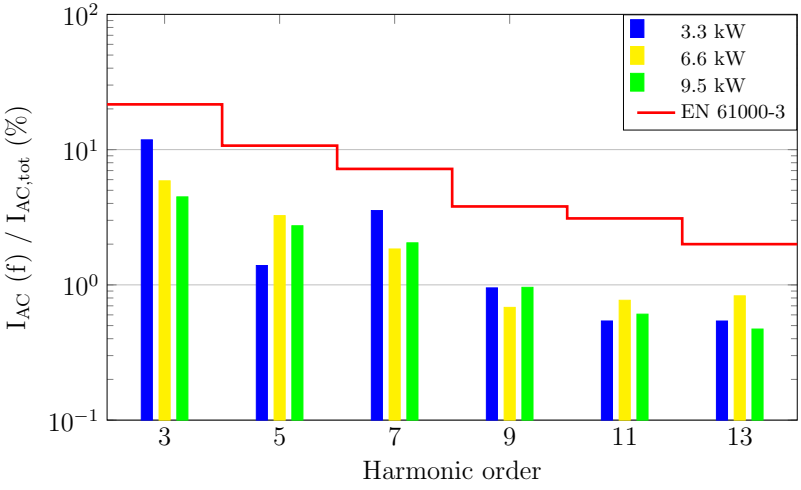

Figure 5.17: THD as function of charging power for WY.

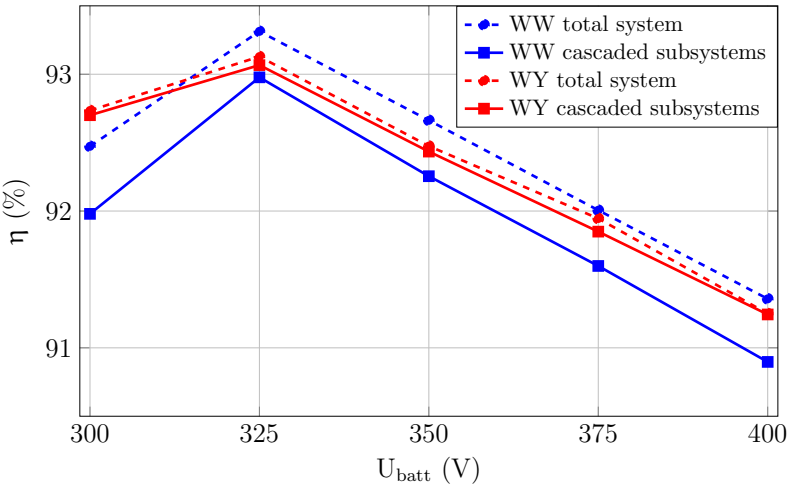

Figure 5.18: Discrepancy between measured and derived system efficiency.

comes however also at the advantage of a higher inductance and thus lower iron losses in the buck converter. Furthermore, the losses are for the WW respectively WY concept 21% and 13% higher at a 50 V offset from the battery voltage than at a 25 V difference. This is explainable since the higher voltage drop means an increased switching ripple, which causes extra AC copper losses and iron losses. Moreover, the increased DC voltages lead to higher switching energies in the inverter. Finally, the iron losses are reduced at increased switching frequencies since the iron loss exponent β of the reduced magnetic fields B_{AC} is larger than the exponent α of the increased frequencies.

5.5.2 Non-isolated Charger Efficiency

The efficiency calculations and measurements for 25 V difference between DC and battery voltage are illustrated in Fig. 5.23 and Fig. 5.24 for both the WW and WY concepts. The efficiencies for a 50 V difference are plotted in Fig. 5.25 and Fig. 5.26 for the WW and WY concepts respectively. All four plots are for a charging power of 6.6 kW. The increase from a 25 V to a 50 V difference leads to an average efficiency drop of 1.6% and 1% for the WW respectively WY

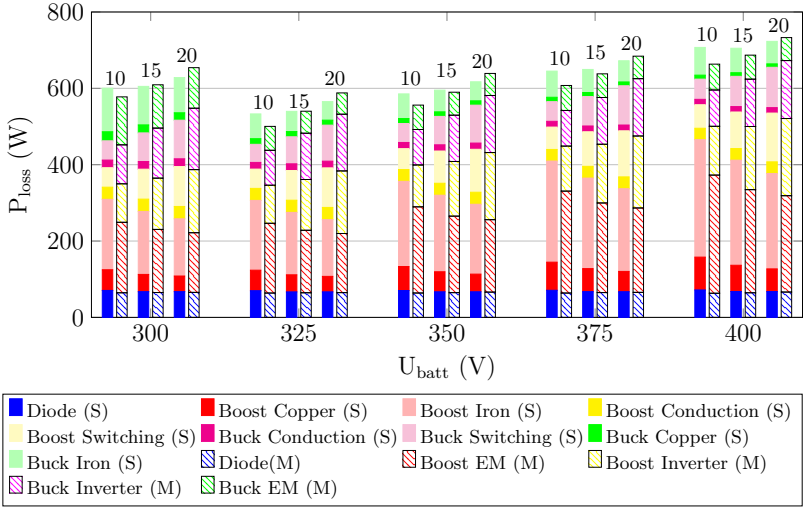

Figure 5.19: Simulated (S) and Measured (M) losses for the WW concept at 25 V delta.

concept. The efficiency is also decreased at enhanced switching frequencies, which is mainly explained by the relatively high switching energies of the inverter. Thanks to the reduced EM losses, there might be an opportunity for increased switching frequencies when using an inverter with lower switching losses. This is investigated in chapter 6.
Further measurements show the efficiency dependency of the charging power for both WW and WY concepts, which is plotted in Fig. 5.27. The WW concept seems more favorable at increased power levels, as the iron losses increase less than the copper losses in the buck stage.

5.5.3 Discussion

The differences between the calculated and measured losses are averaged over all frequencies, DC, and battery voltages and are listed in Tab. 5.4 for each loss component for both the WW and the WY concepts. Percentages above zero indicate that the calculated losses are above the measured losses.
The measured diode rectifier losses are in line with the calculations. The differences between calculated and measured e-drive losses are for the WW

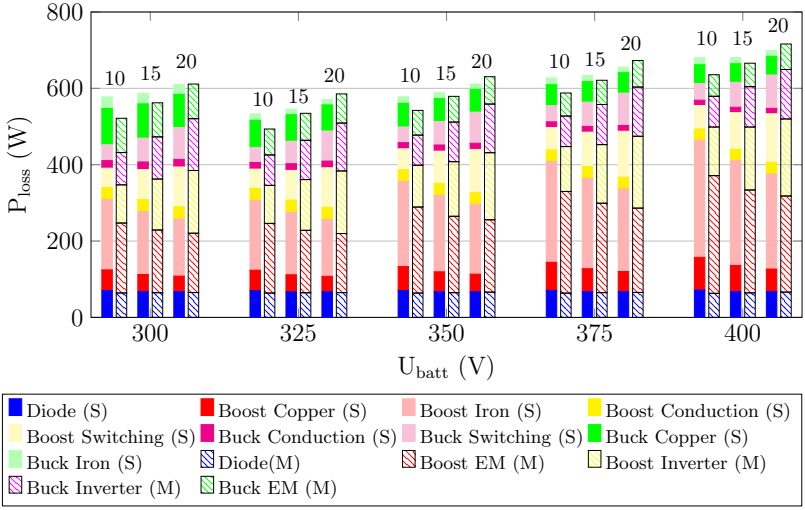

Figure 5.20: Simulated (S) and Measured (M) losses for the WY concept at 25 V delta.

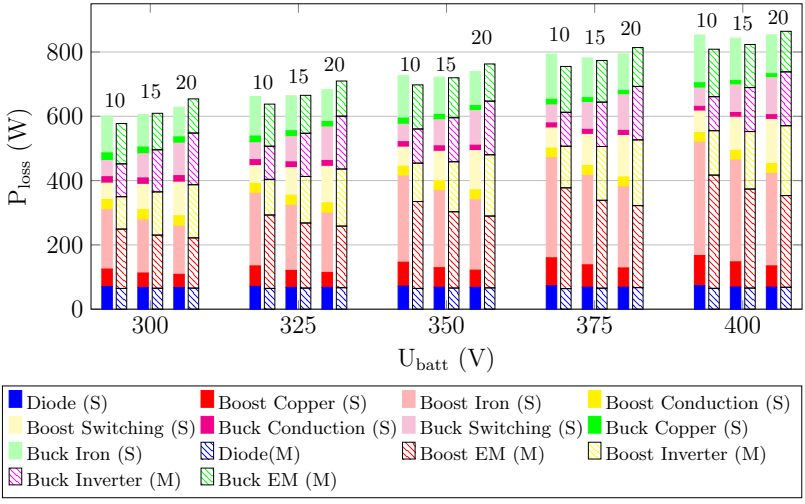

Figure 5.21: Simulated (S) and Measured (M) losses for WW at 50 V delta.

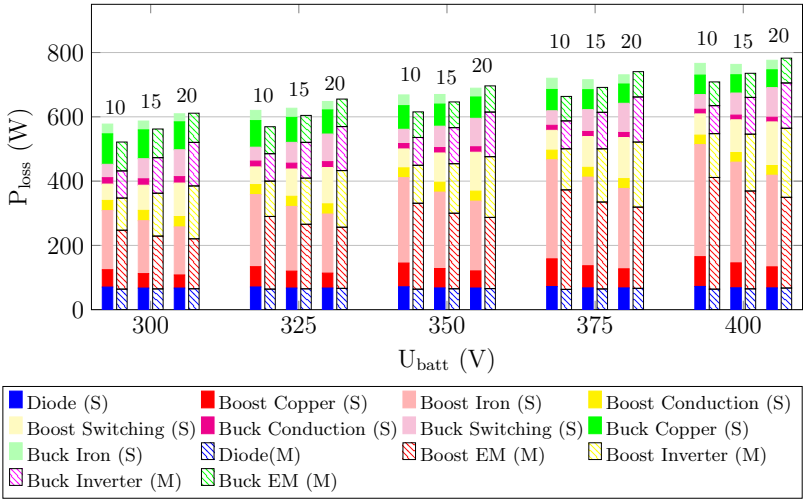

Figure 5.22: Simulated (S) and Measured (M) losses for WY at 50 V delta.

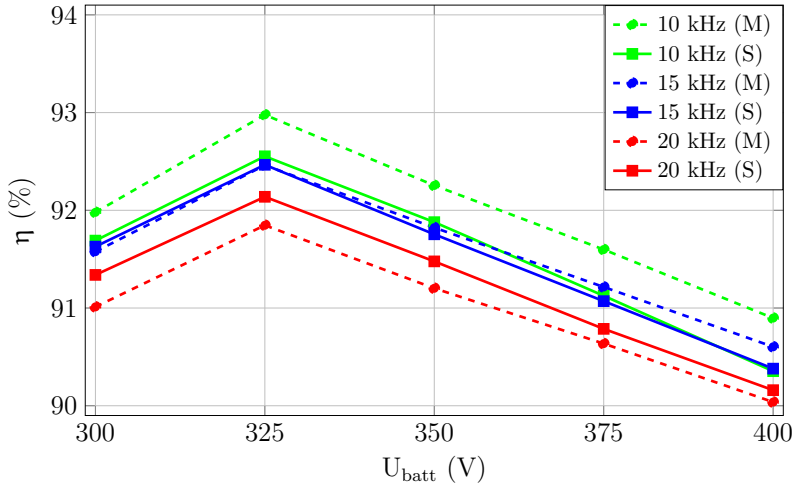

Figure 5.23: Simulated and measured efficiency for WW at 25 V delta.

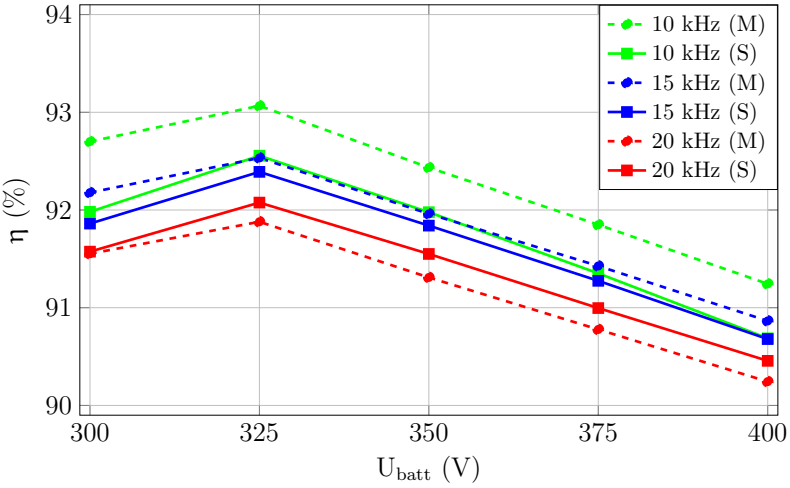

Figure 5.24: Simulated and measured efficiency for WY at 25 V delta.

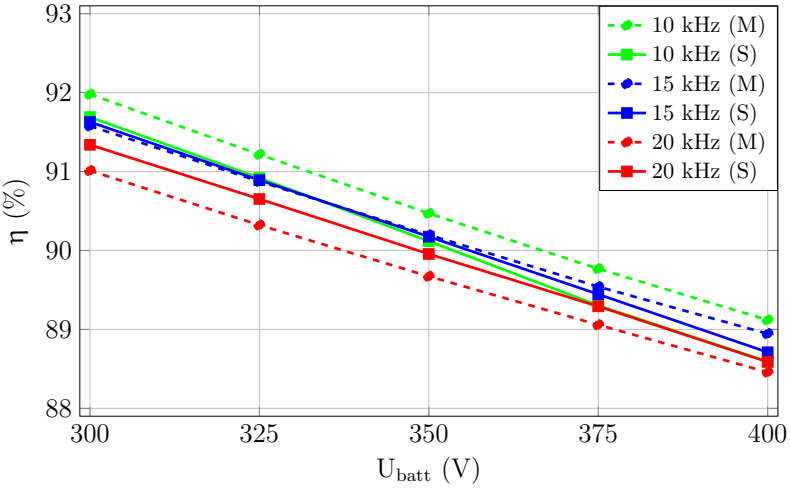

Figure 5.25: Simulated and measured efficiency for WW at 50 V delta.

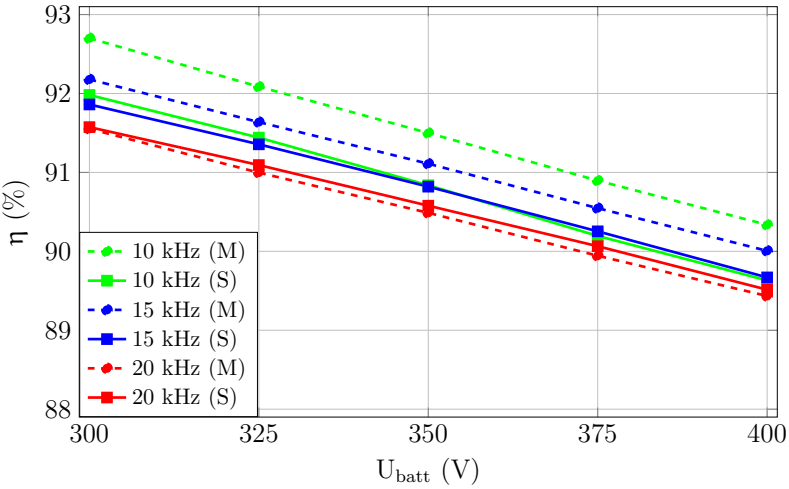

Figure 5.26: Simulated and measured efficiency for WY at 50 V delta.

concept emphasized in Fig. 5.28 for a DC link voltage of 375 V and a battery voltage of 350 V. The measured inverter losses are around 25% above the calculated values, likely due to the increased switching energies as a result of the higher parasitic capacitance when the EM is connected [91, S7]. The EM housing is grounded, by which a parasitic capacitance from phase winding to ground is created. This path is not present in the double pulse measurements, since the inductor housing was not grounded to prevent any influence of external parasitic capacitance on the switching energy measurements. The resulting difference in calculated versus measured inverter losses is more visible at increased values of the switching frequency.

In addition to the difference in inverter losses, the calculated EM losses are above the measured values, which is especially valid for the boost converter with a 25% difference. This is explained by two phenomena: the assumption of k_C based on the winding placement and the sets of Steinmetz parameters that do not exactly reflect the frequency dependent behavior of the iron used in the actual EM.

Reflecting the best case winding placement for k_C due to the unknown winding insertion of the produced EM sample, rather than using the average between

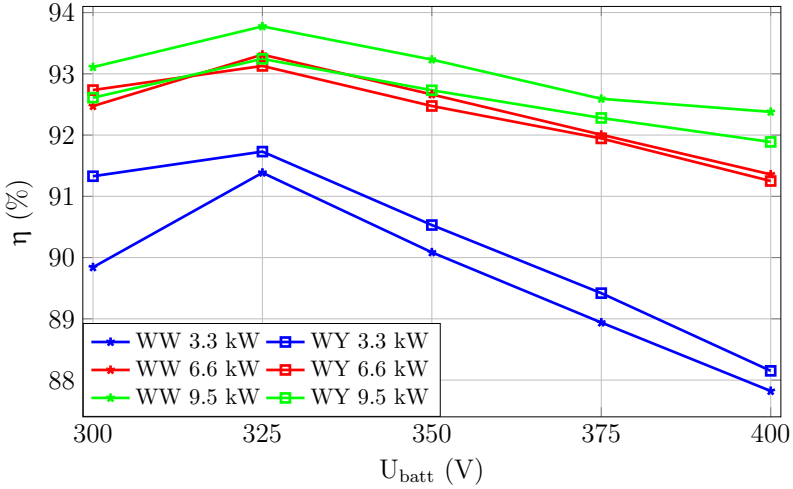

Figure 5.27: Measured system efficiencies at 25 V delta and 10 kHz for different power levels.

best and worst, results in approximately 5% error reduction i.e. in 5-15 Watt reduction of calculated copper losses, dependent on the exact combination of DC and battery voltages, and switching frequency. Moreover, the AC copper loss calculation theory is based on the assumption that each slot has identical winding placement, and that no twisting between slots occurs. In reality, the production process is random and thus, this assumption is not valid. Therefore, the AC copper losses are likely less in reality, especially due to the overestimation of the worst case loss factor [92], that also leads to an overestimated average value for k_C.

In addition to the potentially overestimated copper losses, the other 20% difference in the calculated versus measured EM boost losses could be allocated to the gap in iron losses. The iron losses might be overestimated in the FEM simulation if the actual steel used in the IM has lower losses and less frequency dependency than the steel used for the ring core measurements. Since the IM is not produced from the identical steel batch as the steel used in the measurement rings, there could be a discrepancy between the exact material content as the grade M330 only stands for a specified iron loss density at 50 Hz, not for an

Component	WW	WY
diode rectifier	+6%	+6%
EM boost	+25%	+26%
inverter boost	-22%	-21%
inverter buck	-27%	-26%
EM buck	+12%	+19%

Table 5.4: Loss estimation errors.

exact material content or specified behavior at higher frequencies. Furthermore, the amount of material damage could differ between the laminations of the ring cores and the actual steel used in the EM due to differences in production parameters such as the intensity and speed of the laser cutting [77].

5.6 Safety

The non-isolated integrated charger concepts proposed in this chapter provide a clear efficiency gain over the galvanically isolated concepts described in chapter 3: at least 5% efficiency improvements are reported for the non-isolated concepts since the EM windings are used as inductances instead of being used as a transformer. Since galvanic separation is also one of the safety concepts to protect against electric shock, this safety functionality embedded in galvanically isolated chargers needs to be implemented with other measures in non-isolated chargers as defined in the standards assessed in chapter 1.
As mentioned before, both improved insulation and a residual current detection mechanism with automatic disconnection of supply are allowed safety measures for non-isolated HV battery chargers. Reinforced insulation is feasible, however, it may not be preferred due to the additional thermal resistance between for example the EM windings and the stator core. Such an extra thermal resistance tends to lead to reduced thermal performance, especially in traction mode. Hence, an automatic disconnection of supply with capability of DC fault current detection is required since the integrated charger design does not prevent such currents from flowing in case of an insulation fault, i.e. no galvanic isolation or reinforced or double insulation is present.
If the solution of detection and disconnection of supply is chosen, several detection and disconnection criteria have to be fulfilled. An overview of these

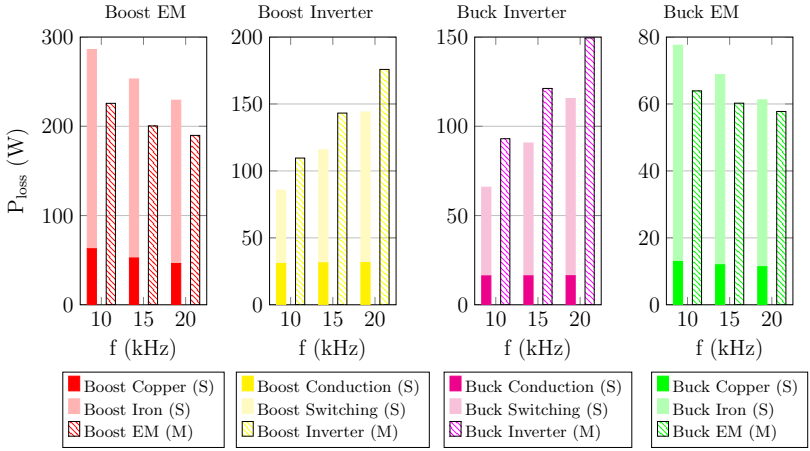

Figure 5.28: Comparison of Simulated (S) and Measured (M) e-drive losses for the WW concept at various switching frequencies and a battery voltage of 350 V.

different criteria based on the safety standards as listed in chapter 1 are presented in Tab. 5.5. Note that IEC 61851 [7] refers to IEC 62955 [93] for these criteria. The lowest current trip level is most difficult to achieve due to the required precision of the detection mechanism. Furthermore, the highest trip level may emphasize the need for fast disconnection gear and poses a requirement on the range of current detection. Three state of the art options for fault current detection are explained in paragraph 5.6.1 and are reviewed in terms of detection capabilities and complexity. Furthermore, these concepts are compared in paragraph 5.6.2.

Norm	Current trip level	Disconnection time
ISO 17409, IEC 62955	6 mA DC	10 s
ISO 17409, IEC 62955	60 mA DC	0.3 s
IEC 62955	200 mA DC	0.1 s
ISO 17409	300 mA DC	0.04 s

Table 5.5: Fault current detection and disconnection requirements.

5.6.1 Residual current detection methods

Three state of the art concepts for residual current detection are described and reviewed in terms of complexity. Furthermore, sensitivity analyses based on practical results are reported. The focus in each concept is placed on detection of the currents, since the disconnection method is identical for each concept and its implementation is considered feasible when switches are used. Solid State Circuit Breaker (SSCB)s with e.g. wide bandgap technologies can be used to reduce the disconnection time [94].
Two detection concepts consist of discrete components: the shunt concept that is based on resistive shunt current measurements, and the inductance concept that is based on inductive current measurements. In addition, a complete solution based on a Differential Current (DI) sensor was reviewed as a reference for residual current detection capabilities. Each concept supports single- and three-phase grids. All concepts are built on a prototype Printed Circuit Board (PCB) that is shown in Fig. 5.29. The shunt resistor is placed between the two red contacts on top of the board. The coil for the inductance concept is placed within the white housing near the bottom right corner of the PCB. In addition, the DI sensor is placed in the top right corner. Furthermore, an Arduino Due microcontroller board is mounted underneath the main PCB on the left side. This microcontroller is used to process the measurement signals and to communicate the measured current values to a PC by means of a Matlab application. Both the inductance concept and the DI sensor solution were tested using DC fault currents superpositioned on top of sinusoidal AC phase currents. The test setup for these concepts is presented in Fig. 5.30. In contrast to the inductance and DI sensor concepts, the shunt concept was tested using a DC load current since superpositioning of DC fault currents onto AC loads was not possible within the same neutral conductor. Therefore, an alternative test bench as illustrated in Fig. 5.31 was used to verify the detection capabilities of the shunt concept. All current measurements are verified with a HP 34401A precision multimeter with ±100 µA accuracy for all measurements up to ±0.5 A, and a ±1.2 mA accuracy for all other measurements.

Shunt Concept

The first concept for residual current detection is based on current measurement through a precise shunt resistor, in which the total conductor current is represented by a voltage drop across the shunt. The shunt resistor is placed in the neutral conductor, which allows for a low-side measurement i.e. at a low

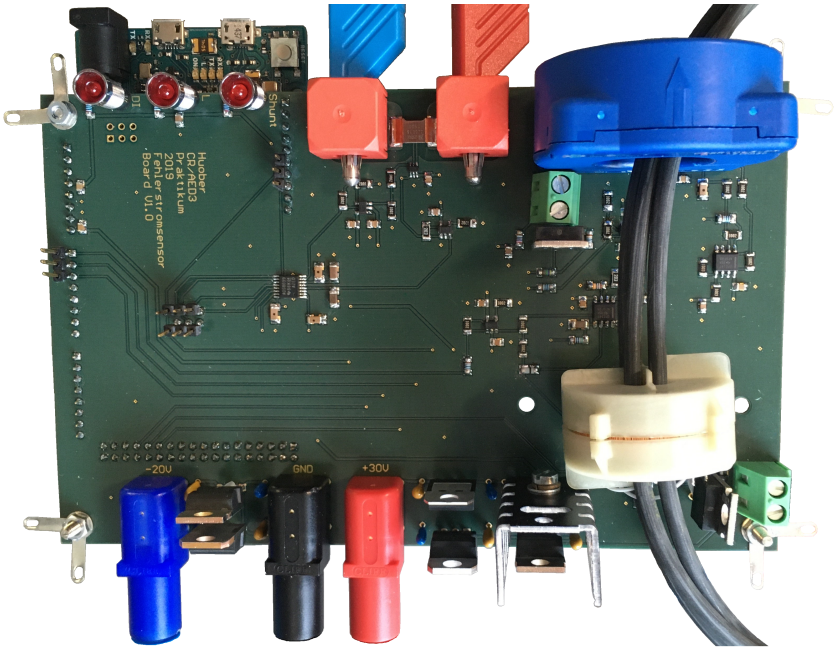

Figure 5.29: Experimental implementation of three residual current detection concepts.

potential after the main load. Thus, the electronics of the analog front end used to read the voltage drop across the resistor is also exposed to a low potential. As a result, isolation from high voltage is not required. Moreover, placing the shunt resistor in the neutral conductor path also allows DC residual current measurements in three-phase chargers. Residual currents are detected based on the principle of mean value tracking over the AC grid time period. If no fault is present, the average resistor voltage drop for the grid time period equals zero. However, the mean value will not be zero if a residual direct current is present in the neutral conductor. Ideally, there is a linear relationship between the average voltage drop and the amount of residual current. Therefore, the sensitivity of the shunt concept is in ideal case linear across the current detection range.
A schematic overview of the fault detection circuit is provided in Fig. 5.32. A DC fault could occur on the DC side of the AC/DC converter as illustrated in the overview. Protection of such currents is provided by the shunt concept since the DC fault current is measured by means of a non-zero average voltage

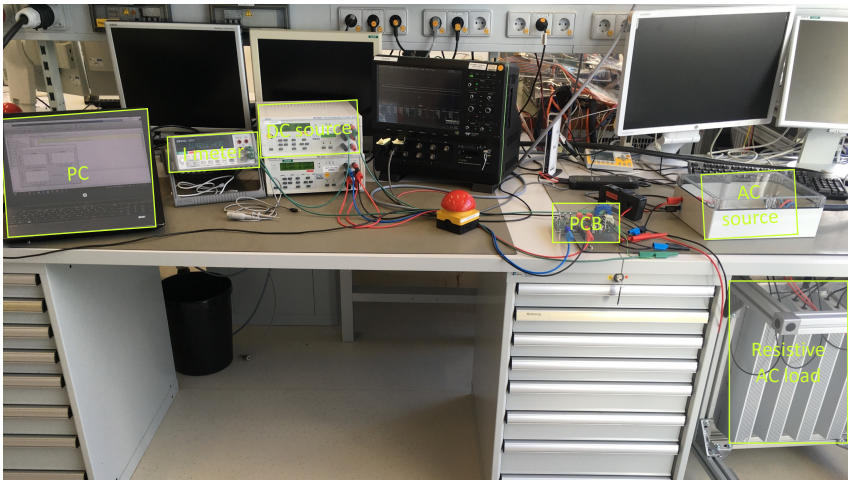

Figure 5.30: Test setup for residual current detection verification for inductance and DI concepts.

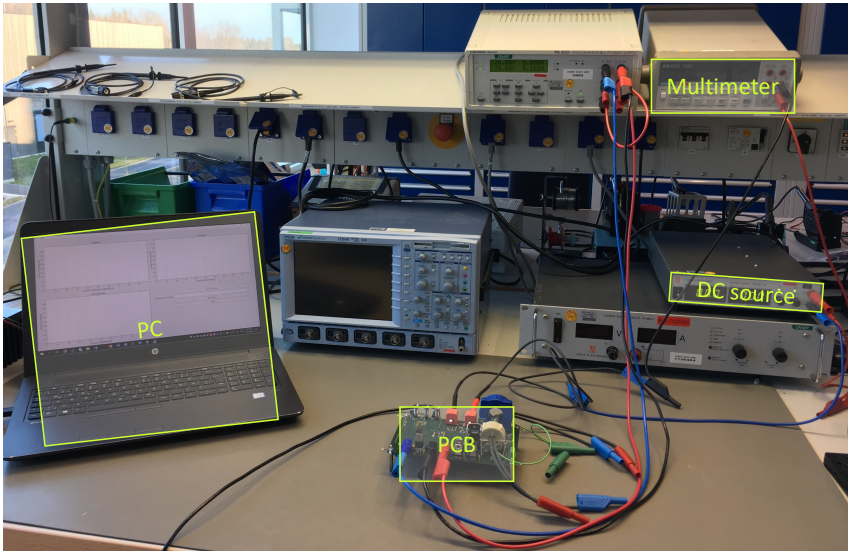

Figure 5.31: Test setup for residual current detection verification for the shunt concept.

drop across the shunt resistor. The voltage drop across the shunt resistor is amplified by a high precision current sense amplifier with very low gain and offset error. As the current sense amplifier only outputs positive voltages, two Operational Amplifier (OPA)s are used to remove the offset added by the current sense amplifier and to provide a sinusoidal voltage signal at the input of the ADC. In theory, any offset that is left at the ADC input signal represents the DC residual current. This remaining signal is sampled with an ADC and is averaged over the grid frequency by a Micro Control Unit (MCU). If the absolute value of this average is above the values allowed by the norms for the respective duration, the relays are triggered to interrupt power supply to the battery charger.
The precision of residual current detection is significantly dependent on the gain and offset error of the current sense amplifier and OPAs, which originate from the non-ideal semiconductors at the inputs of these amplifiers. The offset error is dominant for small currents and is defined as the output voltage at zero input current. Furthermore, there is a temperature drift, which is considered a small component and a slow moving process in comparison to the offset error. The fault detection quality for low residual currents can be improved by calibration of the offset error if necessary. Calibration is done by performing a measurement at zero shunt resistance current e.g. before the charger is connected. The gain error becomes dominant for higher residual currents. The gain error is the relative variance of the amplification compared to its nominal amplification value. Although this error might be calibrated by introducing a precise test current into the shunt, it is a difficult to perform routine since it is hard to reproduce a precise test current. Therefore, components with a very small gain error were chosen.
In addition to the errors introduced by the amplifiers, the offset, Least Significant Bit (LSB) accuracy, and sampling rate of the ADC influence the detection precision since the fault current is a small percentage of the total measured current through the neutral conductor. The influence of these errors can be reduced by selecting a larger shunt resistance value, since that leads to a higher output voltage for a given measured current and thus means less influence of the absolute errors. On the other hand, a resistance of 10 mΩ already implies a power consumption of 10 W at a 32 A Root Mean Square (RMS) phase current, i.e. an efficiency drop of 0.15% at 6.6 kW charging power.
In order to limit the losses, a 3 mΩ resistor from Isabellenhütte was chosen for the proof of concept. Although this resistance has a $\pm$1% tolerance [D8], this influence can be neglected as the tolerance is assumed to be equally distributed across a full sine wave and is thus averaged out in the mean value calculation. In addition, the INA215 from Texas Instruments is used as current sense amplifier

and has an amplification factor of 75, a typical gain error of ±0.02%, and a typical offset error of ±1 µV [D9]. A sampling frequency of 40 kHz was used to minimize noise effects due to discretization. This value is based upon the maximum processing speed of the MCU. An 18 bits ADC was chosen for current detection accuracy of approximately ±0.5 mA. The relative current error as function of shunt current is presented in Fig. 5.33. Note that the ratio is almost constant, which indicates the gain error. Furthermore, the steep drop-off near zero current indicates the offset error.

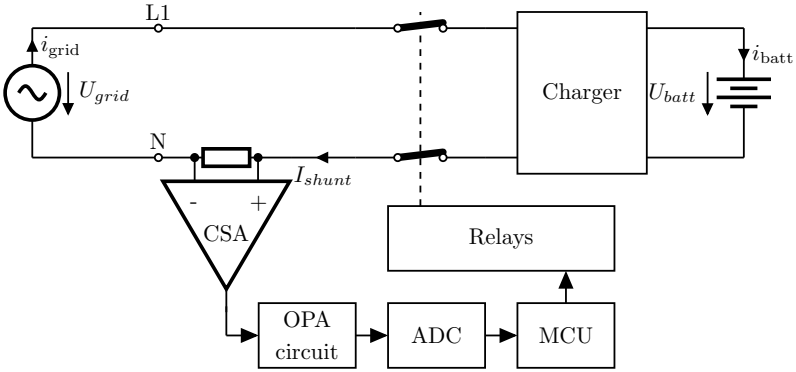

Figure 5.32: Overview of the shunt fault detection concept.

Inductance Concept

The second concept uses a toroidal inductor with a soft-magnetic core. It is very similar to the concept [95] used in Type B RCDs, a class of RCDs that can detect DC fault currents. The concept detects these fault currents by measurements of change in inductance. All current carrying conductors, i.e. the phase(s) and neutral, are wired through the center of a toroidal inductor core. In normal operation i.e. when no residual current is present, the electromagnetic field of all conductors equals zero because the same amount of current enters and leaves the charger. In case of a residual current, only the magnetic field strength H of the residual current will remain, as it equals the difference between the current entering the system and the current leaving the system via the grid connection. Although the fields created by DC fault currents do in contrast to those from AC

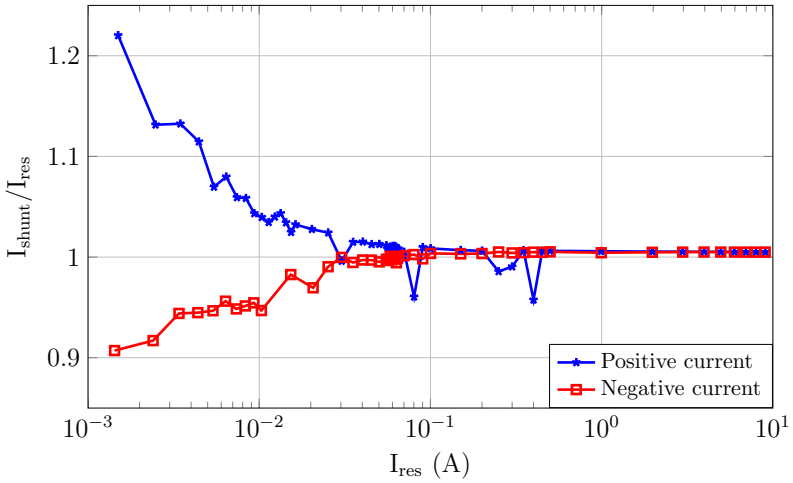

Figure 5.33: Relative error as function of load current for shunt concept.

faults not directly induce a voltage in a passive coil, the core saturates from the DC fault current. This saturation is detectable since it leads to a reduction of the relative permeability μ_r defined by

$$\mu_r = \frac{B}{\mu_0 H}. \tag{5.17}$$

A change in relative permeability leads to a change in inductance, as for a toroid described by

$$L = \frac{\mu_0 \mu_r n^2 l}{2\pi} ln(\frac{r_o}{r_i}). \tag{5.18}$$

The change in inductance is visible by applying a sinusoidal voltage U_{sig} across the toroid windings n and the in series connected resistor R, which is expressed as

$$U_{sig} = I(j\omega L + R). \tag{5.19}$$

The voltage is generated by the MCU using a PWM signal. The current I through the inductor is measured with a shunt resistance R by a differential

amplifier built from two OPAs. The output voltage of the OPAs is converted into a digital signal by the ADC and is read by the MCU. A block diagram of the concept is presented in Fig. 5.34. An increased output voltage equals an increased shunt current and thus, more saturation in the inductor due to its reduced inductance value. More saturation equals a higher fault current.

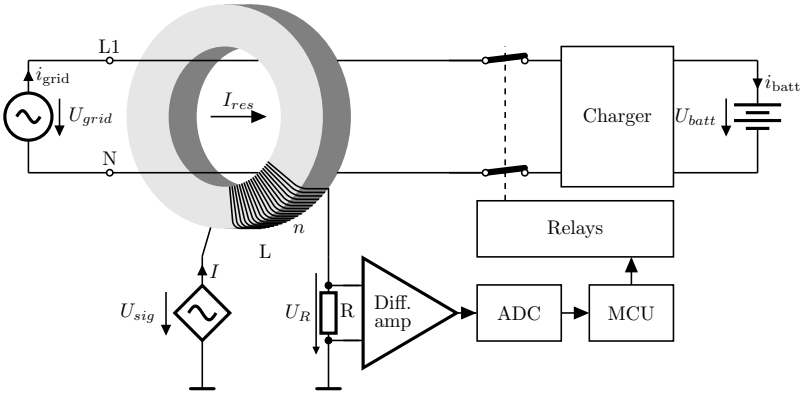

Figure 5.34: Overview of the inductance fault detection concept.

In contrast to the resistive concept, less precision of the ADC and more offset and gain inaccuracy of the OPA are tolerated since only the fault current is measured instead of the full load current. Therefore, the standard 10 bits ADC of the MCU is sufficient. On the other hand, the current measurement capabilities are heavily determined by the saturation of the inductor: once saturated, higher levels of residual currents are not properly detected. In this analysis, a ready wound inductor from a Siemens SIQUENCE 5SM3342-4 type B RCD was used as a proof of concept to analyze the measurement capabilities of this 30 mA household RCD over the entire range of charger fault current limits. In addition, the combined impedance of the inductance and the resistance shall be sufficiently large such that the sinusoidal field induced in the coil does not lead to any change in inductance. A resistance value R of 50.6 kΩ was chosen [S8] for a signal voltage U_{sig} with an amplitude of 1 V and a frequency of 50 Hz. The current detection sensitivity is illustrated with measurements in Fig. 5.35, where the measured current I and thus the coil voltage increase with increased levels of DC fault current. As indicated in the illustration, DC residual currents above approximately 100 mA no longer lead to an increase in measured current.

This means that the concept cannot identify whether a fault current of 100 mA or e.g. 300 mA is present. Hence, the detection quality of fault currents in this concept is heavily dependent on the inductor saturation curve. Therefore, it might be difficult to reach sufficient capabilities to detect both the minimum and maximum trip level properly [S8].

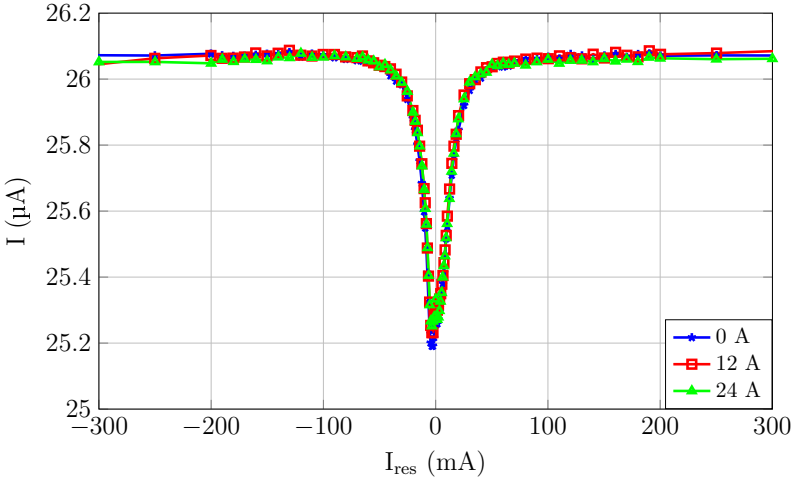

Figure 5.35: Inductor current as function of residual current for inductance concept, measured for load currents of 0, 12, and 24 A.

DI sensor

The last concept consists of a dedicated residual current sensor that is also based on the phenomenon of changed inductance, yet implemented by a fluxgate probe and with active compensation. The concept is shown in Fig. 5.36. A CTSR 0.3-P type sensor from LEM is used, which has detection capabilities up to an RMS fault current of 300 mA [D10]. The sensor consists of a soft-magnetic core, a fluxgate probe with a primary winding n_1 used to detect a change in inductance, a secondary winding n_2 around the magnetic core, and electronics. In order to measure a residual current passing through the magnetic core, all current carrying conductors are wired through this core, identical to the inductance concept. Because the sensor measures the difference between the

current entering a system and the current leaving a system, it is also referred to as differential current (DI) sensor. Thus, any magnetic field present in the core of the sensor is introduced by a residual current. The external field caused by this residual current is detected using a fluxgate probe i.e. a saturable magnetic core with winding n_1 and current I_1. A change in this current I_1 represents a change in inductance of the fluxgate probe. Furthermore, an electronic controller will introduce a current I_2 in the secondary winding n_2 to compensate the detected magnetic field back to zero and to reach the inductance value at zero fault current. The current I_2 passing through the secondary winding represents the amount of residual current passing through the current carrying conductors i.e. the residual current divided by the number secondary windings n_2. With a winding ratio of 1000, the additional power consumption for the compensation is negligible [D10]. The main advantage of the active current compensation in the secondary winding n_2 of this concept over the inductance concept is that the inductor does not saturate thanks to the compensated current. As a result, the DI sensor is more linear over the entire residual current detection range. The secondary current is measured by an internal shunt R and passed to the sensor output as a voltage. An accuracy of 0.6 mA is achievable, reflecting the LSB error of the 10 bits ADC used in the MCU. The relative error as function of the fault current for different loads is presented in Fig. 5.37.

5.6.2 Comparison

The three described residual current detection concepts are compared in terms of cost, current detection range, power consumption, ADC requirements, and volume. The results of this comparison are presented in Fig. 5.38. In this radar chart, the concepts are rated relatively to each other from one to three, where three identifies best case. Furthermore, a cost breakdown of the most expensive required components is provided in Tab. 5.6. It is assumed that no special ADC is required for the inductance and the DI sensor concepts, since a standard 10 bit ADC is likely available in the MCU. This resolution is sufficient as only the actual fault current instead of the entire phase current is read in these concepts. The cost of the shunt and inductance concept are similar and are about a third of the cost of the DI sensor concept. Furthermore, the concepts are rated as function of cost and fault current detection range. This relationship is plotted in Fig. 5.39. Although the shunt and inductance concept have similar cost, the range of fault current detection is significantly larger for the resistance concept as the inductor saturates at higher currents. The DI sensor has a similar current measurement range as the shunt concept, however, it comes at about a factor

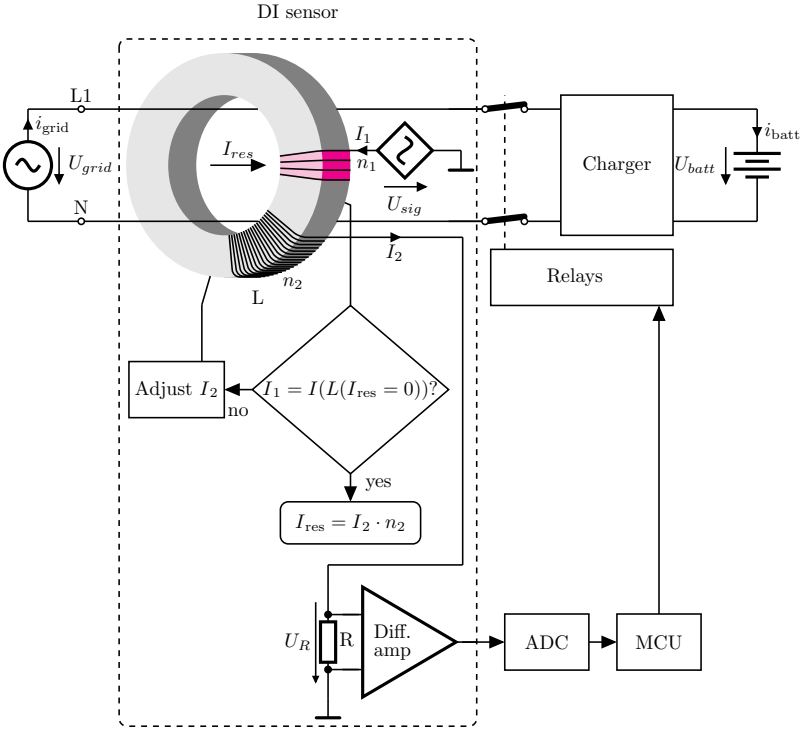

Figure 5.36: Overview of the DI detection concept.

three higher cost. Finally, the shunt concept has highest power consumption and requires least volume thanks to the used shunt instead of toroid for current measurement. Note that the volume of each solution is small in comparison to the required volume for the other charging specific components such as reconnection switches and an EMI filter.

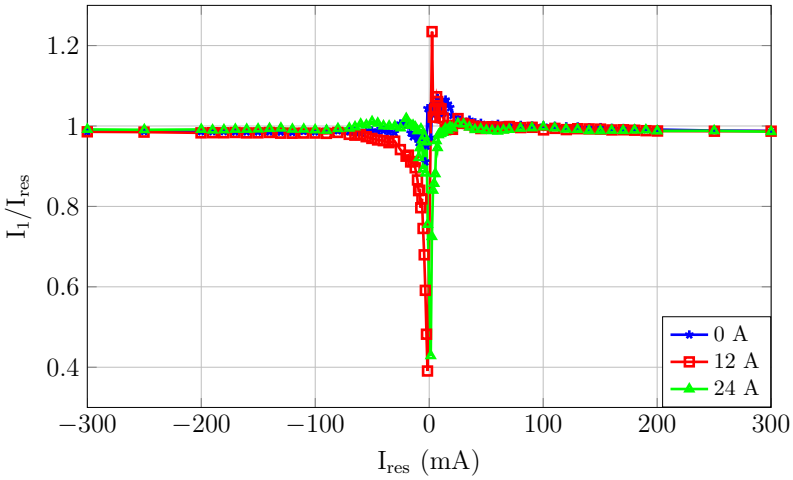

Figure 5.37: Error as function of residual current for DI sensor, measured for load currents of 0, 12, and 24 A.

	Cost ratio (%) per concept		
Component	**Shunt**	**Inductance**	**DI**
Shunt	3	0	0
Inductor	0	15	0
Operational amplifier	12	20	8
Current sense amplifier	4	0	0
ADC	17	0	0
DI sensor	0	0	92
Total	36	35	100

Table 5.6: Cost ratio comparison of different residual current detection concepts.

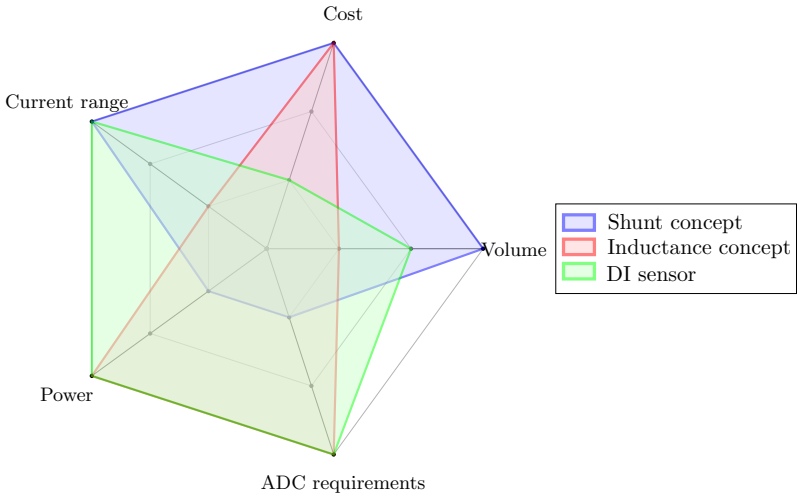

Figure 5.38: Radar chart comparing different fault detection concepts.

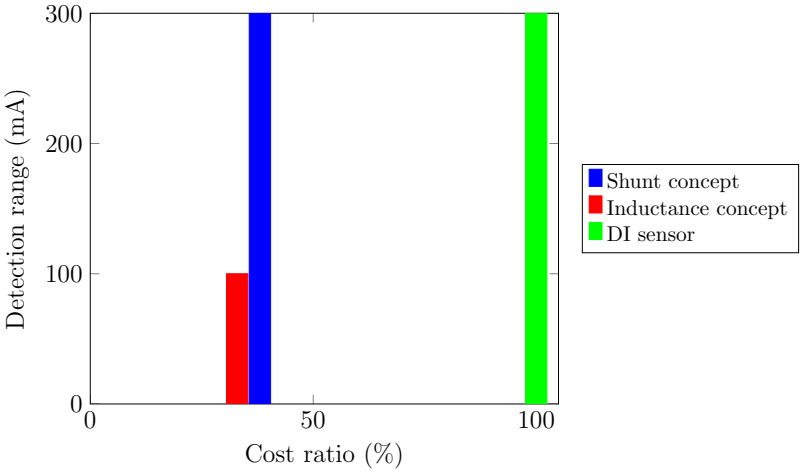

Figure 5.39: Cost versus detection range for different fault detection concepts.

6

Outlook: SiC efficiency improvements

SiC Metal Oxide Semiconductor Field Effect Transistor (MOSFET) is a well-known wide bandgap semiconductor technology that improves the drivetrain efficiency by reducing the semiconductor switching energies in comparison to classical silicon IGBT devices such as those used in the previously analyzed Semikron inverter. By reduction of the switching energies, a reduction of the inverter switching losses becomes possible if the same switching frequency is maintained. In addition to the reduced switching losses, the conduction losses can be reduced by active rectification instead of using the passive freewheeling diode, since the conduction losses of the MOSFET are purely ohmic and do not contain a forward threshold voltage as the diodes and IGBTs have. These benefits especially lead to efficiency improvements in partial load conditions, such as relatively low power charging. In the results presented below, active switching is applied to the boost converter as those diodes are on for a rather long period, especially near the peak of the rectified sine wave, enabling potential energy savings. However, the freewheeling diodes of the buck converter are on for short periods only since the duty cycle D is close to 1, i.e. there is a small voltage step down. Therefore, it is assumed that the turn on and off losses of the active freewheeling would outweigh the diode conduction losses in the buck converter and thus, active freewheeling is only applied to the boost stage.

An inverter design based on generation 3 SiC MOSFET transistor samples from STMicroelectronics is used for a theoretical review of the amount of losses reduction and efficiency improvements of the two novel non-isolated integrated charger concepts. These semiconductor samples are used in Bosch proprietary modules and are not yet commercially available, although this generation is announced in [96]. The inverter voltage class is 1200 V and the nominal phase current is 450 A, which are both identical to the values of the previously assessed Semikron IGBT inverter. The resulting on resistance $r_{DS,on}$ of these SiC devices equals 2.343 mΩ. The system losses for both semiconductor technologies are plotted for 20 kHz in Fig. 6.1 and Fig. 6.2 for the WW and WY concept respectively with both a difference of 25 V between DC link and battery voltage, still with a minimum of 350 V to accommodate some fluctuations of the grid voltage. A detailed overview of the reduction in conduction and switching losses for the SiC semiconductors is provided in Fig. 6.3 and Fig. 6.4 for the WW and the WY concept respectively. Furthermore, the increased system efficiencies are plotted in Fig. 6.5 and Fig. 6.6 for both the WW and the WY concept. An average reduction of 65% in inverter losses is possible when comparing silicon IGBT to SiC MOSFET technology at identical switching frequency of 20 kHz. This leads to an average efficiency improvement of 2.2%. Even if the silicon inverter calculations at 10 kHz are chosen as a reference, an efficiency increase of 1.7% is achieved using the SiC inverter at 20 kHz.
In addition to the above mentioned efficiency improvements between the IGBT and MOSFET inverters at identical switching frequencies, an effort is made to increase the switching frequency to 30 kHz to review any potential further efficiency enhancements as the EM losses could be further reduced. An increase from 20 to 30 kHz does not lead to an enhanced efficiency as is shown in Fig. 6.7. Since it is theoretically possible to distinguish between the switching frequencies between the boost and buck stages, further analysis is presented for a case where the buck efficiency is kept at 20 kHz and the boost frequency is increased to 30 kHz. This strategy leads to an efficiency enhancement of 0.1% at a battery voltage of 350 V, however also to an efficiency drop of 0.15 % at a battery voltage of 400 V. The extra losses at increased battery voltages are due to the non-linear increase in switching energies at higher DC voltages. The following two recommendations are given:

- The switching frequency of the buck stage should be kept at 20 kHz as there is less potential for reduction in iron losses due to the small voltage step down, while the switching losses are still increased at higher switching frequencies.

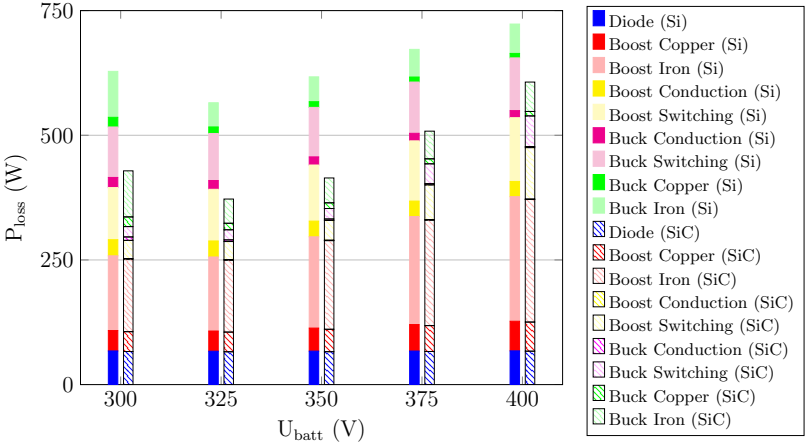

Figure 6.1: System losses for the WW concept with IGBTs (Si) and MOSFETs (SiC).

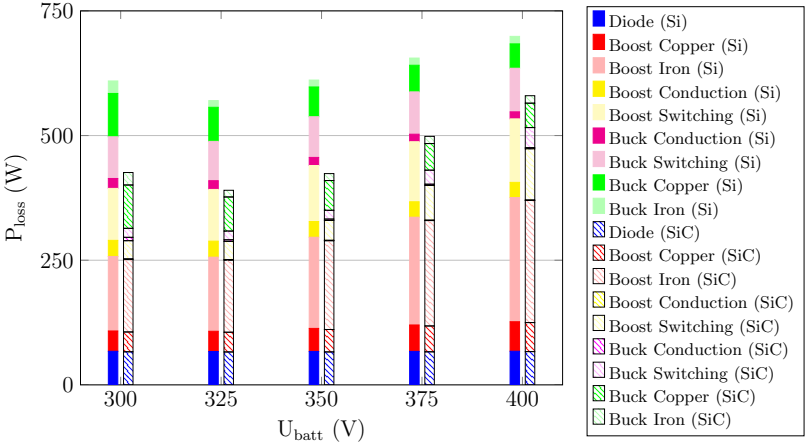

Figure 6.2: System losses for the WY concept with IGBTs (Si) and MOSFETs (SiC).

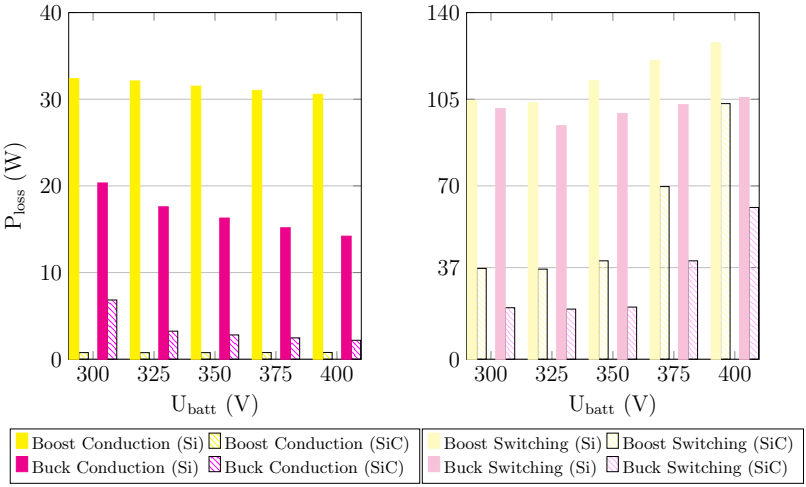

Figure 6.3: Inverter losses for the WW concept with IGBTs (Si) and MOSFETs (SiC).

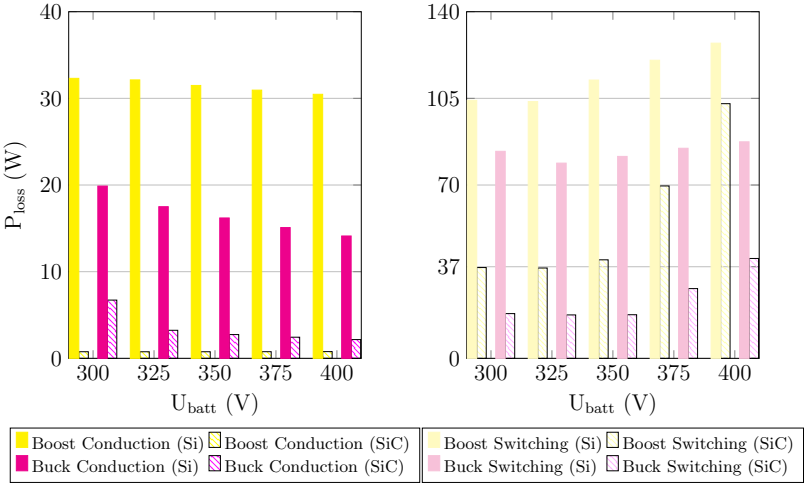

Figure 6.4: Inverter losses for the WY concept with IGBTs (Si) and MOSFETs (SiC).

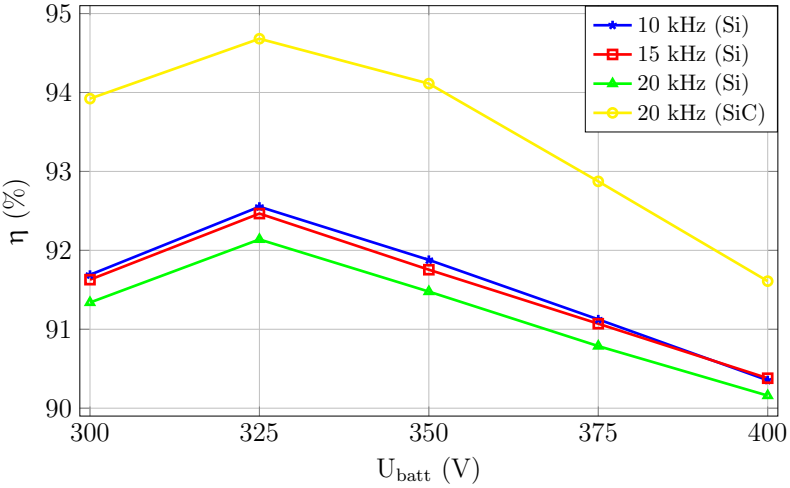

Figure 6.5: Efficiency for the WW concept with IGBTs (Si) and MOSFETs (SiC).

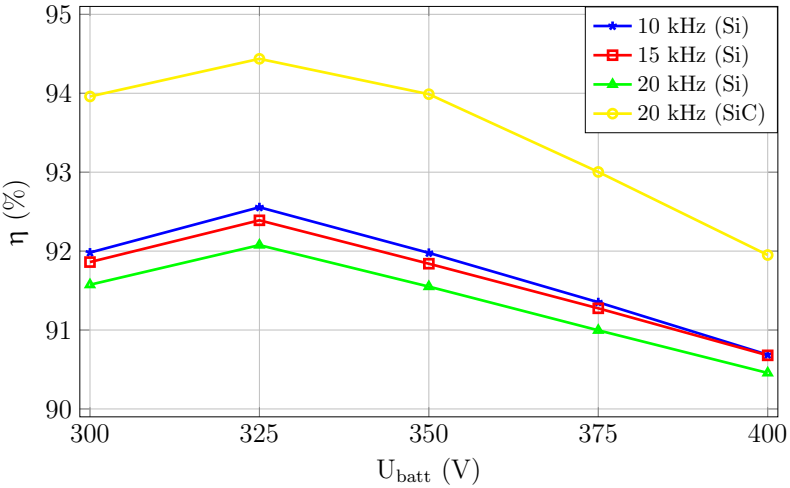

Figure 6.6: Efficiency for the WY concept with IGBTs (Si) and MOSFETs (SiC).

- The switching frequency of the boost stage should only be increased for lower battery voltages to achieve maximum efficiency across the entire charging cycle.

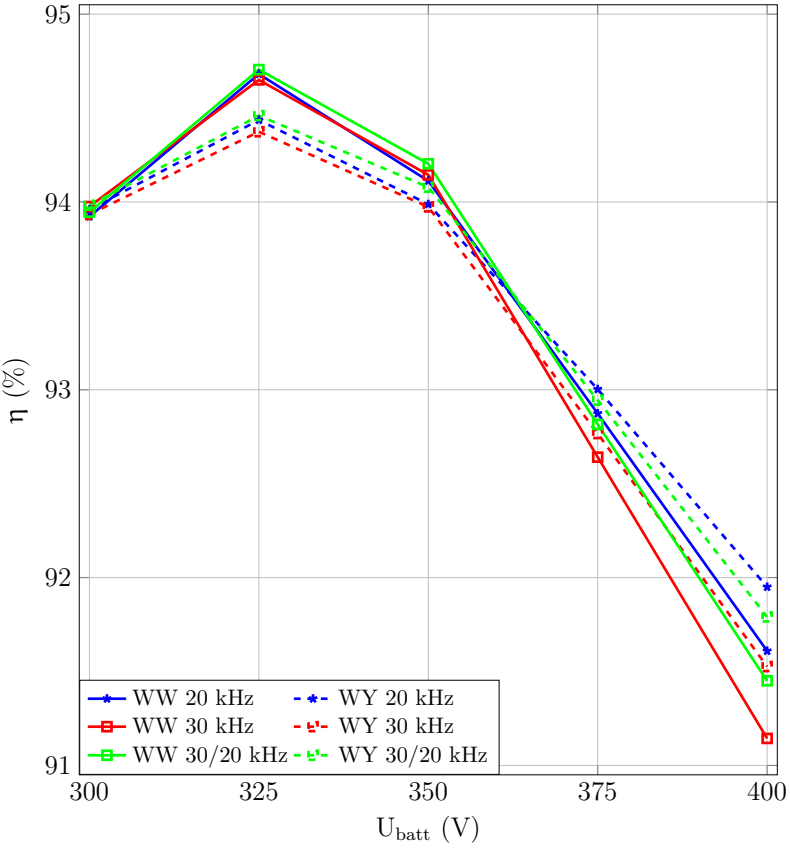

Figure 6.7: Efficiency using SiC MOSFETs at different switching frequencies.

7

Conclusion and Future Work

7.1 Conclusion

State of the Art

A study of regulations and standards concluded that galvanic isolation is not a mandatory measure against electrical shock if fault currents are avoided by other measures e.g. fault current detection with automatic disconnection of the supply. Even though galvanic isolation is not mandatory, several reported integrated chargers use isolation as a protection against electrical shock. Hence, an overview of 33 state of the art isolated and non-isolated integrated charger concepts reported by the industry and academia, which aim to reduce powertrain cost and weight, has been provided in this thesis. Several of these concepts are based on similar use of powertrain. Hence, these concepts have been grouped in the seven found categories of powertrain use: inverter only charging, involving one three-phase EM, involving multiple three-phase EMs, using multi-phase machines as inductors, multi-phase machines as a transformer, concepts using the HV, and LV DC/DC converters. Furthermore, these concepts have been reviewed and compared in terms of topology and powertrain functionality as a charger, advantages and disadvantages, efficiencies, required additional components, compatible EM types, and shaft motion during charging. A summary of this comprehensive comparison is provided in Tab. 2.1–2.3. Most concepts using the e-drive provide either step up or step down functionality, not both. Concepts that do provide both conversion steps require either expensive

reconnection switches and come with shaft torque, or provide poor efficiency. Concepts providing either step up or step down could be combined with the HV DC/DC converter if available. Alternatively, the LV DC/DC converter for the board net could be used in the charging process, although this limits the charging power. Multi-phase e-drives provide more flexibility for integration of step up and down conversion. Therefore, three new concepts based on 2x3 phase EMs have been developed.

Isolated Battery Charger

A new isolated integrated charger concept with the goal to improve the efficiency from state of the art isolated charger concepts while avoiding rotor shaft rotation has been reviewed. In this concept, the e-drive is used as an isolated DC/DC converter with the EM as a transformer at standstill. Therefore, a IM or EESM with a rotor that can be opened is required to prevent shaft rotation during charging. Theoretical analysis with FEM of this concept using a 153 kW SCIM as an 11 kW 600 V battery charger indicate maximum efficiencies of 89% from DC/DC. A dedicated front end AC/DC converter is required for charging from AC grids, which leads to a maximum charger efficiency of 88%. A novel efficiency improvement method by means of a winding reconnection layout is proposed, which indicate up to 0.5% efficiency improvements. Moreover, the novel idea of placement of additional windings in the stator slots with a high turn ratio to accommodate LV DC/DC conversion is proposed, e.g. for the purpose of providing energy to the board net for the vehicle auxiliaries. This functionality is also assessed using FEM modeling. Although technically feasible, the peak power capabilities of the EM are reduced by 4% since some of the power is transferred from the main windings to the board net instead of to the rotor shaft. Therefore, 4% more active EM volume is required to compensate for the reduction in peak performance assuming that no further peak performance density increase is possible. This corresponds to approximately 0.2 L of additional active volume for the analyzed EM with an active volume of 4.58 L. As a result, integration of the board net isolation transformer in the EM is not beneficial since a dedicated transformer could be made much smaller when operating at significantly higher switching frequencies than those used in the inverter. Due to the low efficiency, it is recommended to focus on non-isolated integrated charging. The LV DC/DC converter can then not be integrated as the board net requires galvanic isolation from the HV battery. In addition to the efficiency analysis, a cost analysis of the added components for this isolated charger concept is presented. Cost similar to that of a dedicated onboard charger

are reported, mainly due to the expensive adjustments needed to the rotor in order to avoid shaft rotation during charging. The only found advantage of the isolated charger concept over a dedicated onboard charger is the estimated 44% volume saving.

Losses under DC biased load

As a result of the low efficiency and high cost of the isolated charger concept, novel non-isolated integrated charger concepts have been developed and are investigated. In non-isolated integrated chargers, the e-drive is typically used under DC biased charging condition. Therefore, the EM copper and iron loss theory is applied to obtain a better understanding of the efficiency levels for non-isolated integrated charger concepts. Material measurements have been performed for the laser cut stator and the stamped rotor steel of the used EM. These form a basis for the characterization of the Steinmetz parameters that describe the iron losses, which were calculated using FEM for the frequency area of the switching frequency and for loads as present during charging. The values of these Steinmetz parameters change over the level of DC load, causing an offset in the magnetic field density. Therefore, three different sets of parameters were found, dependent on the exact load and connection of EM windings. Furthermore, the copper losses including skin effect, proximity effect, and circulating currents are assessed in analytical form with the use of frequency dependent correction factors for the regular ohmic resistance. In addition to the EM losses, the switching energies of the used Semikron silicon IGBT inverters were measured as those were not specified for the small operating currents during charging.

Non-isolated Battery Chargers

A novel topology for integrated charging without galvanic isolation has been presented and reviewed. The concept consists of a 2x3 phase e-drive that is in charging mode used as a series connected boost-buck converter. Although these two three-phase winding sets could be integrated into a single housing, it is also possible to use two separate three-phase e-drives in series connection. The topology consists of a full bridge diode rectifier to connect single-phase grids to the first three-phase winding set. This three-phase subsystem is operated as a boost PFC converter and is used to stabilize the DC link voltage to a predefined level while maintaining unity power factor. In addition, a step down converter is connected to the vehicle battery by using the second three-phase

subsystem of the e-drive. Different reconnection variants have been assessed in terms of connection possibilities and conceivably generated shaft torque. Two reconnection variants are proposed for non-isolated battery charging without developed shaft torque: the WW concept and the WY concept. All three EM windings and corresponding inverter legs of a three-phase system are connected in parallel in the boost stage, thus creating a W type of connection. A W connection or a Y connection, where two phases are placed in parallel with the third winding in series, is proposed for the step down stage since this converter converts stationary direct currents. Therefore, any potential shaft torque other than an alignment torque at start of charging is avoided in Y connection for the buck converter. Assuming that the six-phase e-drive is already in place, only a reconnection switch, a diode rectifier, an EMI filter, and a detection and disconnection device for interruption of supply in case of fault currents are required. Analytical description is provided in order to solve the voltage equations for boost and buck operation with a six-phase EM, especially to describe the equations for the WY variant where the neutral point of the buck converter windings is floating. The zero torque condition for both WW and WY concepts is verified with FEM simulations and a control system is described. In addition, an experimental prototype has been implemented to prove 6.6 kW charging functionality between 300-400 V battery voltage with switching frequencies of 10, 15, and 20 kHz and from a single-phase 230 V 50 Hz AC grid rated at 32 A. Power quality measurements have proven that both concepts fulfill the norms with respect to harmonic distortion of the grid current. Moreover, a detailed losses breakdown and efficiency analysis in both calculations based on the described losses theory and in measurements has been provided. Efficiency levels up to 93% are reported at a switching frequency of 10 kHz and the error between losses calculations and measurements is well within ±1% for all operating points. The EM losses are overestimated up to 26% and the inverter losses are underestimated up to 27%. Although the efficiencies of the WW and WY concepts are comparable, there are more iron losses and less copper losses in the WW concept due to the lower inductance and resistance of the W winding connection in the buck stage.

Residual Current Detection

Three state of the art concepts for detection of DC fault currents are described and analyzed in terms of complexity, cost, and fault detection performance for a range of trip levels between 6 and 300 mA. Moreover, experimental results have been presented for all three concepts. One concept is based on resistive

measurements using a shunt in the neutral conductor and it has been shown that detection of currents was even possible at the lowest trip level of 6 mA if components and their tolerances are correctly chosen. A second concept consists of a toroid inductor with a core in which the line and neutral wires are placed. If a difference in current between both wires exists, a magnetic field causes reduced core permeability and thus a change in inductance. This change in inductance is measured by the inductor current when a sinusoidal voltage is applied. The coil current corresponds to the amount of fault current, which is no longer precise once the core is in saturation and is thus sensitive to the core layout. It was found that this concept is least able to detect the wide range of fault current trip levels. In addition to the two concepts built from discrete components, a complete DI sensor solution has been assessed. It is shown that this sensor has good detection capabilities for all trip current levels, similar to the shunt concept. However, the DI concept is about three times more expensive than either the shunt or the inductor concept.

Silicon Carbide

Finally, charger efficiency improvements of 1.7-2.2% have been shown for SiC inverters based on calculations for both WW and WY concepts if the switching is increased from 10 to 20 kHz. Moreover it was found that a further increase in switching frequency to 30 kHz for the boost stage could lead to an additional 0.1% efficiency improvement only for lower battery voltages. The switching frequency of the step down converter should not be further increased as this stage has a lower potential for reduction of iron losses, while the switching losses would still be increased at enhanced switching frequencies. A maximum charger efficiency of 94.7% is reached. These results are comparable with that of dedicated onboard chargers, yet with significantly fewer components and thus, at a significantly lower cost and weight. The reported efficiencies make the proposed WW and WY concepts excellent low cost high efficient integrated single-phase AC battery chargers for vehicles that contain a six-phase e-drive or two three-phase drive systems, already today for silicon inverters and especially in the future once the price reduction of SiC inverters make those mainstream.

7.2 Future Work

Future research activities include a number of areas varying from losses calculation and efficiency enhancements to functionality aspects including the integration of the RCD concepts and three-phase AC grids.

Losses and efficiency

More precise loss calculations can reduce the gap between calculated and measured values. The switching energies for the inverter could for example be measured with the actual EM and cables to include the actual parasitic capacitances that are seen during the switching events in order to obtain more accurate values of the switching energies in the actual use case [S7]. Although precise specific iron Steinmetz parameterization remains difficult for already built EMs, it is possible to produce ring samples along with the stator and rotor laminations for newly built machines. This would reduce the spread in material and production processing properties and helps to reduce the error between calculated and measured iron losses. The effects of core saturation due to high strength magnetic offset fields could cause errors in the loss description when using Steinmetz parameters. The quality of the loss calculations should thus be verified for high charging currents. Consideration of a more random winding insertion during production as suggested in [92] could lead to a more accurate estimation of the AC copper losses, mainly thanks to a better estimation of the correction factor k_C for the circulating currents.
The charging efficiency could be enhanced by several aspects. On a system level, it is possible to introduce interleaved switching, which leads to an enlarged effective inductance. Therefore, a reduced switching ripple with lower iron and AC copper losses are expected. Possible shaft torque and vibration effects due to the high frequent ripple that is no longer balanced across the windings should be investigated. Furthermore, a Proportional Resonant (PR) controller could be used to reduce the second harmonic power ripple component of the DC link voltage [97, 98]. This allows for a reduction in the difference between the DC link and battery voltages and thus, leads to a reduced DC link voltage with enhanced efficiency as a result. In addition to these changes in switching strategy, efficiency improvements by means of EM and inverter design are possible. For example, as the diodes in the boost inverter are more used during charging, it could be worth to investigate optimizations for reduced diode conduction losses. Moreover, a lower voltage class could where possible further decrease the inverter losses during charging. Furthermore, the EM

iron losses might be reduced by selection of a core made from thinner steel laminations, or even from Soft Magnetic Composite (SMC). Although the latter one significantly reduces the iron losses, it is questionable if the increased cost and effect on peak traction capabilities are acceptable.

Functionality

A charging capability and efficiency comparison of the non-isolated charger functionality across different EM categories such as the EESM and the widely used PMSM could be evaluated. Specifically, the magnet losses and effects on efficiency of PMSMs should be assessed. Moreover, rotor alignment to the stator currents could be investigated. As mentioned before, the Y connection could impose alignment torque on a PMSM rotor that is not aligned. This shaft torque could potentially lead to partial demagnetization if the rotor cannot not be aligned during initialization of the charging process, e.g. if the rotor shaft is mechanically locked by the parking brake. Partial demagnetization of the magnets could occur if high charging currents in the stator coils induce magnetic fields in opposite direction of the magnet flux and with field strengths above the coercivity value H_C. Although it is not expected that the entire magnet is susceptible for this high field strength, the magnet edges could potentially irreversibly be damaged due to this effect. As a result, the peak capabilities in traction mode might be reduced. Therefore, the feasibility of the Y connection should be investigated for higher charging currents in cases where rotor alignment is not possible.
A suggestion for connection of three-phase AC grids is made by utilizing a winding arrangement for the boost PFC stage like the center tap winding concept as discussed in paragraph 2.4.1 followed by the W or Y connection for the step down converter. A variant with a 2x3 phase EM followed by a three-phase EM in W connection is illustrated in Fig. 7.1 for simplified drawing purposes. However, it is of course feasible to use a 3x3 e-drive instead. At least the 2x3 phase windings used in the boost PFC converter have to be placed in the same housing with each winding of a phase in opposite direction of each other such that zero MMF is developed during charging. An additional advantage of the three-phase grid connection using a center tap winding is the ability of bi-directional power flow for Vehicle to Grid (V2G) applications.
Further integration of the RCD concepts in the actual powertrain is also required to verify detection capabilities and cost effectiveness in a real use case. An effort should be made to understand any potential residual currents flowing through the parasitic paths present in the powertrain under different ambient scenarios,

which might trigger a nuisance trip of the RCD and interrupt charging even in the scenario that there is no-one present and an electric shock does not occur [99]. While electric shocks shall be prevented at all times, the charging process should still be completed within the expected duration and should not be interrupted due to a nuisance trip of the RCD.
Finally, charging functionality integration in the powertrain implies additional use of these components. Therefore, the combined traction and charging duration leads to an increased lifetime requirement. Hence, an analysis should be made to verify that the additional lifetime requirements due to charging do not lead to a significant increase in powertrain component cost.

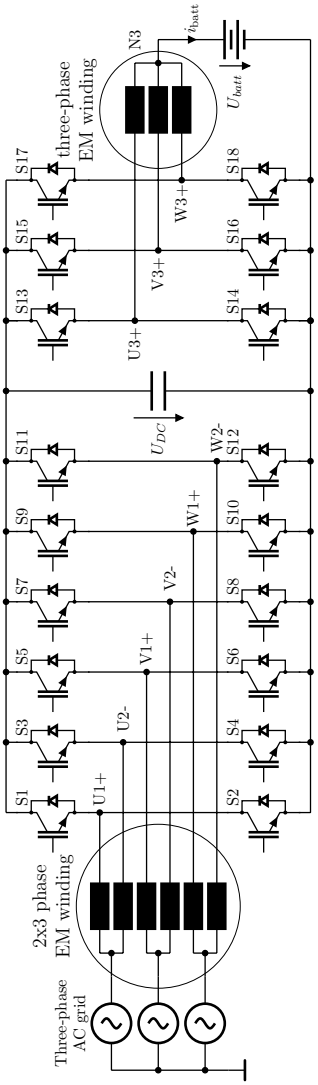

Figure 7.1: Three-phase integrated charger with step up and down functionality.

Nomenclatures

Acronyms

2D	Two Dimensional
4WD	Four Wheel Drive
AC	Alternating Current
AC/DC	Alternating Current to Direct Current
ADC	Analog to Digital Converter
BEV	Battery Electric Vehicles
CCM	Continuous Conduction Mode
CSI	Current Source Inverter
CUT	Core Under Test
DC	Direct Current
DC/DC	Direct Current to Direct Current
DCM	Discontinuous Conduction Mode
DI	Differential Current
EESM	Electrically Excited Synchronous Machine
EM	Electrical Machine
EMI	Electro Magnetic Interference
FEM	Finite Element Method
FFT	Fast Fourier Transformation
FPGA	Field Programmable Gate Array
FSCW	Fractional Slot Concentrated Winding
GSE	Generalized Steinmetz Equation
HV	High Voltage
IGBT	Insulated Gate Bipolar Transistor
IGSE	Improved Generalized Steinmetz Equation

IM	Induction Machine
LSB	Least Significant Bit
LUT	Look-Up Table
LV	Low Voltage
MCU	Micro Control Unit
MMF	Magneto Motive Force
MOSFET	Metal Oxide Semiconductor Field Effect Transistor
MSE	Modified Steinmetz Equation
OPA	Operational Amplifier
PC	Personal Computer
PCB	Printed Circuit Board
PELV	Protected Extra Low Voltages
PF	Power Factor
PF_{disp}	Displacement Power Factor
PF_{dist}	Distortion Power Factor
PFC	Power Factor Correction
PI	Proportional Integral
PMSM	Permanent Magnet Synchronous Machine
PR	Proportional Resonant
PWM	Pulse Width Modulation
RCD	Residual Current Device
RMS	Root Mean Square
RMSE	Root Mean Square Error
SCIM	Squirrel Cage Induction Machine
SELV	Separated Extra Low Voltages
SiC	Silicon Carbide
SMC	Soft Magnetic Composite
SoC	State of Charge
SRM	Switched Reluctance Machine
SSCB	Solid State Circuit Breaker
SSE	Sum of Squared Errors
THD	Total Harmonic Distortion
V2G	Vehicle to Grid
VSI	Voltage Source Inverter
WEG	Water Ethylene Glycol
WRIM	Wound Rotor Induction Machine

Symbols

General

A	Cross sectional area
B_{AC}	AC component of magnetic flux density
B_{DC}	DC component of magnetic flux density
B	Magnetic flux density
C_{DC}	DC link capacitance
H_{C}	Coercivity value of magnetic field strength
H	Magnetic field strength
I_1	Primary current
I_2	Secondary current
I_{AC}	RMS AC current
I_{DC}	DC current
I_{M}	Magnetization current
I	RMS current
J	Current density
$\underline{L}$	Inductance matrix
L	Inductance
M	Magnetization
$P_{\mathrm{Cu,AC}}$	AC copper losses
$P_{\mathrm{Cu,DC}}$	DC copper losses
P_{Cu}	Copper losses
P^*_{batt}	Reference battery charging power
P_{loss}	Losses
R_{DC}	DC copper resistance
R_{ph}	EM stator phase resistance
$\underline{R}$	Ohmic resistance matrix
R	Ohmic resistance
U^*_{DC}	Reference DC link voltage
U_{DC}	DC link voltage
U_{batt}	Battery voltage
U_{grid}	Grid voltage
U_{sig}	Signal voltage
η	Efficiency
f_{grid}	Grid frequency

f	Frequency
i_{N1}	Primary neutral point current
i_{O}	Boost output current
i_{U}	Buck input current
i^*_{batt}	Reference battery current
i_{batt}	Battery current
i^*_{grid}	Reference grid current
i_{grid}	Grid current
$\underline{i_{\mathrm{s}}}$	Stator phase current vector
i_{u1}	Primary u phase current
i_{u2}	Secondary u phase current
i_{v1}	Primary v phase current
i_{v2}	Secondary v phase current
i_{w1}	Primary w phase current
i_{w2}	Secondary w phase current
l	Length
μ_0	Permeability of air
μ_{r}	Material specific relative permeability
μ	Permeability
n_1	Primary coil winding
n_2	Secondary coil winding
n	Number of coil turns
ω	Angular frequency
ρ	Specific resistivity
r_{i}	Inner radius of toroid
r_{o}	Outer radius of toroid
σ	Specific conductivity
t	Time
$u_2(t)$	Secondary winding voltage
u_{O}	Boost inductor voltage
$u_{\mathrm{R}}(t)$	Resistive voltage drop
u_{U}	Buck inductor voltage
$u^*_{\mathrm{abc,batt}}$	Reference phase modulation voltages for battery side converter
$u^*_{\mathrm{abc,grid}}$	Reference phase modulation voltages for grid side converter
$\underline{u_{\mathrm{s}}}$	Stator phase voltage vector
u_{u1}	Primary u phase voltage
u_{u2}	Secondary u phase voltage

u_{v1}	Primary v phase voltage
u_{v2}	Secondary v phase voltage
u_{w1}	Primary w phase voltage
u_{w2}	Secondary w phase voltage

AC Copper Losses

A_s	Strand cross sectional area
$\beta_{s,EW}$	Reduced strand height for end winding
β_s	Reduced strand height
β_t	Reduced turn height
d_s	Strand diameter
η	Parallel winding displacement factor
h_{slot}	Slot height
$h_{t,bad}$	Turn height for bad case of winding placement
$h_{t,good}$	Turn height for good case of winding placement
h_t	Turn height
$k_{C,bad}$	Circulating current loss factor for bad case of winding placement
$k_{C,good}$	Circulating current loss factor for good case of winding placement
k_{Cu}	Slot fill factor
k_C	Circulating current loss factor
$k_{P,AL}$	Proximity loss factor for the EM core
$k_{P,EW}$	Proximity loss factor for the end winding
k_P	Proximity loss factor for both the EM core and end winding
l_{AL}	Length of the EM core
l_{EW}	Length of the end winding
$m_{t,bad}$	Number of turns in radial direction for bad case of winding placement
$m_{t,good}$	Number of turns in radial direction for good case of winding placement
m_t	Number of turns in radial direction
n_{par}	Number of parallel strands
ψ	Auxiliary function for proximity effect
φ	Auxiliary function for skin effect
w_{slot}	Slot width

$z_{\mathrm{h,EW}}$	Number of strands stacked in radial direction for the end winding
z_{h}	Number of strands stacked in radial direction
z_{w}	Number of strands stacked in tangential direction

Iron Losses

K_0	Factor for iron losses at 0 T offset
K_{boost}	Factor for iron losses for the boost circuit
$K_{\mathrm{buck,W}}$	Factor for iron losses for the buck circuit in W connection
$K_{\mathrm{buck,Y}}$	Factor for iron losses for the buck circuit in Y connection
K_{e}	Factor for eddy current losses
K_{h}	Factor for hysteresis losses
K	Factor for iron losses
P_{Fe}	Iron losses
P_{eddy}	Eddy current losses
P_{hys}	Hysteresis losses
R^2	R square, coefficient of determination
R^2_{adj}	Adjusted R square, coefficient of determination
α	Coefficient for frequency
β_0	Coefficient for magnetic flux density at 0 T offset
β_{boost}	Coefficient for magnetic flux density for the boost circuit
$\beta_{\mathrm{buck,W}}$	Coefficient for magnetic flux density for the buck circuit in W connection
$\beta_{\mathrm{buck,Y}}$	Coefficient for magnetic flux density for the buck circuit in Y connection
β	Coefficient for magnetic flux density
δ	Coefficient for field density of eddy current losses
γ	Coefficient for frequency of eddy current losses

Power Electronics

D	Duty cycle
E_{off}	Transistor turn off energy
E_{on}	Transistor turn on energy
E_{rr}	Diode reverse recovery energy
P_{cond}	Inverter conduction losses

P_{sw}	Inverter switching losses
T_2	Time at which inductor current reaches zero
T_{s}	Switching time period
U_{CE0}	No load collector emitter conduction voltage drop
$u_{\mathrm{CE}}(t)$	Collector emitter voltage drop
U_{F0}	No load diode forward voltage drop
$u_{\mathrm{F}}(t)$	Diode forward voltage drop
f_{s}	Switching frequency
$i_{\mathrm{cap,AC,pk}}$	Peak value of capacitor grid AC current component
$i_{\mathrm{C}}(t)$	Collector current
$i_{\mathrm{D}}(t)$	Diode current
$i_{\mathrm{L}}(t)$	Inductor current
i_{cap}	Capacitor current
r_{CE}	IGBT on resistance
$r_{\mathrm{DS,on}}$	MOSFET on resistance
r_{F}	Diode forward resistance
u_{C}	Capacitor voltage

List of Figures

List of Tables

References

Own Publications

[E1] E. Hoevenaars, T. Illg, and M. Hiller, "Novel Integrated Charger Concept Using an Induction Machine as Transformer at Standstill," in *2020 IEEE Vehicular Power and Propulsion Conference*, Gijon, Spain, November 2020.

[E2] E. Hoevenaars, Q. Wang, P. Schumann, and M. Hiller, "Novel Integrated Charger Concepts Using Six Phase Electrical Machines as Boost-Buck Converter," in *PCIM Europe digital days 2020*, Germany, July 2020.

[E3] E. Hoevenaars and M. Hiller, "Efficiency of Motor and Inverter Reconfigured as a Boost-Buck Connected Integrated BEV Charger," in *2021 IEEE Energy Conversion Congress and Expo*, Vancouver, Canada, October 2021.

[E4] E. Hoevenaars and M. Hiller, "Conceptualization and Efficiency Review of Integrated Chargers Using Six-Phase Machines," *IEEE Transactions on Transportation Electrification*, vol. 8, no. 1, pp. 48–61, 2022.

[E5] E. Hoevenaars, Z. Yin, and Q. Wang, "Elektrische Maschine und Verfahren zur Änderung von Wicklungsauslegungen eines Stators einer elektrischen Maschine," *German Patent DE 102019216488 A1*, 29 April 2021.

[E6] E. Hoevenaars, "Elektrische Maschine, Verfahren zum Betreiben einer elektrischen Maschine, Ladesystem," *German Patent DE 102019203703 A1*, 24 September 2020.

[E7] T. Janbein, T. Illg, and E. Hoevenaars, “System,” *German Patent DE 102019210786 A1*, 21 January 2021.

Student Theses

[S1] T. Illg, *Erstellung eines Modells einer sechsphasigen elektrischen Maschine zur Nutzung der Maschine als Transformator*. Master Thesis, Karlsruhe Institute of Technology, 2018.

[S2] Z. Yin, *Electrical Machine Optimizations for EV Transformer and Traction Applications*. Master Thesis, University of Stuttgart, 2019.

[S3] Q. Wang, *Electrical Machine Optimizations for Multiple Power Sources in EV Traction Applications*. Research Thesis, University of Stuttgart, 2019.

[S4] M. Siegle, *Softwareentwicklung zur adaptiven Regelung einer beliebigen Kurvenform für Verlustmessungen weichmagnetischer Werkstoffe*. Research Thesis, University of Stuttgart, 2017.

[S5] K. Beder, *Electrical Machine control and operating strategy for integrated charging applications*. Research Thesis, University of Stuttgart, 2020.

[S6] Q. Wang, *Electrical Machine control strategy for novel integrated charging applications*. Master Thesis, University of Stuttgart, 2019.

[S7] F. Willer, *Fachpraktikumsbericht*. Internship Report, Leibniz University Hannover, 2020.

[S8] J. Huober, *Concept Development for a Residual Current Monitoring Device for the Charging of Electrical Vehicles*. Internship Report, Konstanz University of Applied Sciences, 2020.

Datasheets and Application Manuals

[D1] Brochure, “REMAGRAPH C,” *MAGNET-PHYSIK Dr. Steingroever GmbH*, 2018.

[D2] Datasheet, “SKAI 45 A2 GD12-W12-DI,” *SEMIKRON International GmbH*, 2011.

[D3] Datasheet, “SKiM459GD12E4V2,” *SEMIKRON International GmbH*, 2017.

[D4] Datasheet, “BumbleBee High Voltage Differential Probe,” *PMK GmbH*, 2020.

[D5] Datasheet, “CWT Ultra-mini,” *PEM*, 2018.

[D6] Datasheet, “APT2X101D60J,” *Microsemi Power Products Group*, 2011.

[D7] Brochure, “Brochure LMG500,” *Zimmer GmbH*, 2012.

[D8] Datasheet, “ISA-WELD Precision Resistors BVS Size 3920,” *Isabellenhütte*, 2020.

[D9] Datasheet, “INA21x Voltage Output, Low- or High-Side Measurement, Bidirectional, Zero-Drift Series, Current-Shunt Monitors,” *Texas Instruments*, 2017.

[D10] Datasheet, “Current Transducer CTSR series,” *LEM*, 2014.

Other Literature

[1] M. Woodward, B. Walton, J. Hamilton, G. Alberts, S. Fullerton-Smith, E. Day, and J. Ringrow, “Electric vehicles Setting a course for 2030,” *Deloitte Insights*, 28 July 2020.

[2] T. Schoenen, M. S. Kunter, M. D. Hennen, and R. W. De Doncker, “Advantages of a Variable DC-Link Voltage by Using a DC-DC Converter in Hybrid-Electric Vehicles,” in *2010 IEEE Vehicle Power and Propulsion Conference*, Lille, France, September 2010.

[3] J. Schmenger, S. Endres, S. Zeltner, and M. März, “A 22 kW On-board Charger for Automotive Applications Based on a Modular Design,” in *2014 IEEE International Conference on Energy Conversion (CENCON)*, Johor Bahru, Malaysia, October 2014.

[4] IEC 60050-826:2004, “International Electrotechnical Vocabulary - Part 826: Electrical installations,” International Electrotechnical Commission, Standard, 2004.

[5] S. Czapp, D. Krzysztof, J. Klucznik, and Z. Lubosny, “Low-Frequency Tripping Characteristics of Residual Current Devices,” in *2017 IEEE International Conference on Environment and Electrical Engineering and 2017 IEEE Industrial and Commercial Power Systems Europe*, Milan, Italy, June 2017.

[6] ISO 17409:2015(E), “Electrically propelled road vehicles - Connection to an external electric power supply - Safety requirements,” International Standards Organization, Standard, 2015.

[7] IEC 61851-3-1:2016, “Electric Vehicles Conductive Power Supply System - Part 3-1: General Requirements for Light Electric Vehicles AC and DC conductive power supply systems,” International Electrotechnical Commission, Standard, 2016.

[8] GB/T 18487.1-2015, “Electric Vehicles Conductive Charging System - Part 1: General Requirements,” Standardization Administration of the People’s Republic of China, Standard, 2015.

[9] UL 2231-1, “Standard for Safety for Personnel Protection Systems for Electric Vehicle (EV) Supply Circuits: General Requirements,” Underwriters Laboratories, Standard, 2012.

[10] H. Turker, “Review of Electric Motors for Grid Connected Integrated Battery Chargers in Electric Vehicle Applications,” in *2016 IEEE International Conference on Renewable Energy Research and Applications*, Birmingham, United Kingdom, November 2016.

[11] M. Yilmaz and P. Krein, “Review of Integrated Charging Method for Plug-In Electric and Hybrid Vehicles,” in *2012 IEEE International Conference on Vehicular Electronics and Safety*, Istanbul, Turkey, July 2012.

[12] S. Kinoshita, “Electric system for electric vehicle,” *US Patent no. 5,504,414*, 2 April 1996.

[13] J. Y. Lee, H. S. Song, I. P. Yoo, K. Y. Jang, S. Shin, and J. H. Joo, “System for recharging plug-in hybrid vehicle and control method for the same,” *US Patent no. 8,441,229 B2*, 14 May 2013.

[14] D. Richer, P. Delbosc, J.-P. Ferrieux, B. Chauchat, and M. Brunello, “Mixed electric power supply system comprising an inverter and an alternating-direct converter,” *International Patent WO 97/08009*, 6 March 1997.

[15] T. Umetsu and K. Yomo, “Charger for electric vehicle,” *Japanese Patent no. 06303702A*, 28 October 1994.

[16] N. Inoue, S. Kuriyama, N. Matsudaira, S. Naito, and T. Yokoyama, “Vehicle mount battery charger utilizing motor driving inverter,” *Japanese Patent no. 7193911A*, 28 July 1995.

[17] S. Loudot, B. Briane, and O. Ploix, "Electric motor assembly rechargeable from an electrical mains system, and dedicated connection housing," *International Patent WO 2010/142738 A2*, 16 December 2010.

[18] A. G. Cocconi, "Combined motor drive and battery recharge system," *US Patent no. 5,341,075*, 23 August 1994.

[19] A. Mengatto and J. A. Heerdt, "Analysis and Operation of an Integrated Battery Charger for Using the EV Traction Motor as Filter," in *2017 Brazilian Power Electronics Conference*, Juiz de Fora, Brazil, November 2017.

[20] B. T. Vankayalapati, S. Rajeev, and V. K. Bussa, "Two Stage Integrated On-Board Charger for EVs," in *2018 IEEE International Conference on Industrial Technology*, Lyon, France, February 2018.

[21] W. E. Rippel, "Integrated traction inverter and battery charger apparatus," *US Patent no. 4,920,475*, 24 April 1990.

[22] C. Shi, Y. Tang, and A. Khaligh, "A Single-Phase Integrated Onboard Battery Charger Using Propulsion System for Plug-in Electric Vehicles," *IEEE Transactions on Vehicular Technology*, vol. 66, no. 12, pp. 10 899–10 910, 2017.

[23] L. Solero, "Nonconventional On-Board Charger for Electric Vehicle Propulsion Batteries," *IEEE Transactions on Vehicular Technology*, vol. 50, no. 1, pp. 144–149, 2001.

[24] G. Pellegrino, E. Armando, and P. Guglielmi, "Integrated battery charger for electric scooter," in *2009 European Conference on Power Electronics and Applications*, Barcelona, Spain, September 2009.

[25] G. Pellegrino, E. Armando, and P. Guglielmi, "An Integral Battery Charger With Power Factor Correction for Electric Scooter," *IEEE Transactions on Power Electronics*, vol. 25, no. 3, pp. 751–759, 2010.

[26] S. Loudot, B. Briane, O. Ploix, and A. Villeneuve, "Fast charging device for an electric vehicle," *International Patent WO 2010/103063 A1*, 16 September 2010.

[27] C. Gailla and L. Meysenc, "Conversion stage, electric converter including such a conversion stage, device for converting an ac current into dc current including such a converter, terminal for recharging an electric battery including such a converter or conversion device," *US Patent no. 9,270,182 B2*, 23 February 2016.

[28] S. Loudot, S. Cregut, and M. Ameziani, "Electric motor vehicle comprising a contact or contactless charger," *International Patent WO 2012/028797 A2*, 8 March 2012.

[29] S. Kinoshita, "Electric system of electric vehicle," *US Patent no. 5,629,603*, 13 May 1997.

[30] P. Dupuy, "Electric traction chain for an automobile," *International Patent WO 2010/012924 A2*, 4 February 2010.

[31] B. Briane and S. Loudot, "Interconnection housing for motor vehicle," *International Patent WO 2010/063921 A1*, 10 June 2010.

[32] S. Smolenaers, "A Vehicle Charging Station," *International Patent WO 2018/204964 A1*, 15 November 2018.

[33] T.-H. Liu, Y. Chen, P.-H. Yi, and J.-L. Chen, "Integrated battery charger with power factor correction for electric-propulsion systems," *IET Electric Power Applications*, vol. 9, no. 3, pp. 229–238, 2015.

[34] T.-H. Liu, P.-H. Yi, and J.-L. Chen, "Implementation of an Integrated Battery-Charger for an Electric-Propulsion System," in *IECON 2014 40th Annual Conference of the IEEE Industrial Electronics Society*, Dallas, United States, October 2014.

[35] D.-G. Woo, Y.-S. Kim, G.-B. Kang, and B.-K. Lee, "Advanced Integrated Battery Chargers for Plug-in Hybrid Electric Vehicles," in *2012 IEEE Vehicle Power and Propulsion Conference*, Seoul, Korea, October 2012.

[36] D.-G. Woo, D.-M. Joo, and B.-K. Lee, "On the Feasibility of Integrated Battery Charger Utilizing Traction Motor and Inverter in Plug-In Hybrid Electric Vehicles," *IEEE Transactions on Power Electronics*, vol. 30, no. 12, pp. 7270–7281, 2015.

[37] S. Q. Ali, D. Mascarella, G. Joos, and L. Tan, "Torque elimination for integrated battery charger based on two permanent magnet synchronous motor drives for electric vehicles," *IET Electric Power Applications*, vol. 11, no. 9, pp. 1627–1635, 2017.

[38] S.-J. Lee and S.-K. Sul, "An integral battery charger for 4 wheel drive electric vehicle," in *1994 IEEE Industry Applications Society Annual Meeting*, Denver, United States, October 1994.

[39] S.-J. Lee and S.-K. Sul, "An Integral Battery Charger for Four-Wheel Drive Electric Vehicle," *IEEE Transactions on Industry Applications*, vol. 31, no. 5, pp. 1096–1099, 1995.

[40] L. De Sousa, B. Silvestre, and B. Bouchez, "A Combined Multiphase Electric Drive and Fast Battery Charger for Electric Vehicles," in *2010 IEEE Vehicle Power and Propulsion Conference*, Lille, France, September 2010.

[41] L. De-Sousa and B. Bouchez, "Combined Electric Device for Powering and Charging," *International Patent WO 2010/057892 A1*, 27 May 2010.

[42] L. De-Sousa and B. Bouchez, "Method and Electric Combined Device for Powering and Charging with Compensation Means," *International Patent WO 2010/057893 A1*, 27 May 2010.

[43] S. Lacroix, E. Laboure, and M. Hilairet, "An Integrated Fast Battery Charger for Electric Vehicle," in *2010 IEEE Vehicle Power and Propulsion Conference*, Lille, France, September 2010.

[44] M. Diab, A. Elserougi, A. Abdel-Khalik, A. Massoud, and S. Ahmed, "A Nine Switch Converter Based Integrated Motor Drive and Battery Charger System for EVs Using Symmetrical Six-Phase Machines," *IEEE Transactions on Industrial Electronics*, vol. 63, no. 9, pp. 5326–5335, 2016.

[45] H. J. Raherimihaja, G. Xu, and Q. Zhang, "Review and Novel Options of Three-Phase Integrated Battery Chargers for EVs," in *2020 IEEE Vehicular Power and Propulsion Conference*, Gijon, Spain, November 2020.

[46] N. Sakr, A. F. Sanchez, D. Sadarnac, and A. Gascher, "A combined switched reluctance motor drive and battery charger for electric vehicles," in *2015 41st Annual Conference of the IEEE Industrial Electronics Society*, Yokohama, Japan, November 2015.

[47] J. Jiang and T. Xia, "An Integrated Charger with Central-Tapped Winding Switched Reluctance Motor Drive," in *2017 IEEE 6th International Conference on Renewable Energy Research and Applications*, San Diego, United States, November 2017.

[48] I. Subotic, N. Bodo, and E. Levi, "Single-Phase On-Board Integrated Battery Chargers for EVs Based on Multiphase Machines," *IEEE Transactions on Power Electronics*, vol. 31, no. 9, pp. 6511–6523, 2016.

[49] I. Subotic, N. Bodo, E. Levi, and M. Jones, "Onboard Integrated Battery Charger for EVs Using an Asymmetrical Nine-Phase Machine," *IEEE Transactions on Industrial Electronics*, vol. 62, no. 5, pp. 3285–3295, 2015.

[50] I. Subotic, *Integrated on-board battery chargers for EVs based on multiphase machines and power electronics*. PhD Thesis, Liverpool John Moores University, 2015.

[51] R. Aguirre, A. Lopez-de-Heredia, I. Villar, and G. Almandoz, "On-Board Integrated Battery Charger Using a Nine-Phase FSCW PMSM for an Electric Bus," in *2020 IEEE Vehicular Power and Propulsion Conference*, Gijon, Spain, November 2020.

[52] N. Bodo, E. Levi, I. Subotic, J. Espina, L. Empringham, and C. M. Johnson, "Efficiency Evaluation of Fully Integrated On-Board EV Battery Chargers With Nine-Phase Machines," *IEEE Transactions on Energy Conversion*, vol. 32, no. 1, pp. 257–266, 2017.

[53] F. Lacressonniere and B. Cassoret, "Converter used as a battery charger and a motor speed controller in an industrial truck," in *2005 European Conference on Power Electronics and Applications*, Dresden, Germany, September 2005.

[54] H. Plesko, J. Biela, J. Luomi, and J. W. Kolar, "Novel Concepts for Integrating the Electric Drive and Auxiliary DC-DC Converter for Hybrid Vehicles," *IEEE Transactions on Power Electronics*, vol. 23, no. 6, pp. 3025–3034, 2008.

[55] H. Plesko, J. Biela, and J. W. Kolar, "Design and Analysis of a New Drive-Integrated Auxiliary Dc-Dc Converter for Hybrid Vehicles," in *2008 IEEE Industry Applications Society Annual Meeting*, Edmonton, Canada, October 2008.

[56] S. Haghbin, S. Lundmark, M. Alaküla, and O. Carlson, "Grid-Connected Integrated Battery Chargers in Vehicle Applications: Review and New Solution," *IEEE Transactions on Industrial Electronics*, vol. 60, no. 2, pp. 459–473, 2013.

[57] S. Haghbin, *Integrated Motor Drives and Battery Chargers for Electric or Plug-in Hybrid Electric Vehicles*. PhD Thesis, Chalmers University of Technology, 2013.

[58] S. Haghbin, S. Lundmark, M. Alaküla, and O. Carlson, "An Isolated High-Power Integrated Charger in Electrified-Vehicle Applications," *IEEE Transactions on Vehicular Technology*, vol. 60, no. 9, pp. 4115–4126, 2013.

[59] S. Haghbin, K. Khan, S. Zhao, M. Alaküla, S. Lundmark, and O. Carlson, "An Integrated 20-kW Motor Drive and Isolated Battery Charger for Plug-In Vehicles," *IEEE Transactions on Power Electronics*, vol. 60, no. 8, pp. 4013–4029, 2013.

[60] A. S. Abdel-Khalik, A. Massoud, and S. Ahmed, "Interior permanent magnet motor-based isolated on-board integrated battery charger for electric vehicles," *IET Electric Power Applications*, vol. 12, no. 1, pp. 124–134, 2018.

[61] Y.-J. Lee, A. Khaligh, and A. Emadi, "Advanced Integrated Bidirectional AC/DC and DC/DC Converter for Plug-In Hybrid Electric Vehicles," *IEEE Transactions on Vehicular Technology*, vol. 58, no. 8, pp. 3970–3980, 2008.

[62] D.-H. Kim, M.-J. Kim, and B.-K. Lee, "An Integrated Battery Charger With High Power Density and Efficiency for Electric Vehicles," *IEEE Transactions on Power Electronics*, vol. 32, no. 6, pp. 4553–4565, 2017.

[63] G.-J. Su and L. Tang, "An Integrated Onboard Charger and Accessory Power Converter for Plug-in Electric Vehicles," in *2013 IEEE Energy Conversion Congress and Exposition*, Denver, United States, September 2013.

[64] G.-J. Su and L. Tang, "A New Integrated Onboard Charger and Accessory Power Converter for Plug-in Electric Vehicles," in *2014 IEEE Energy Conversion Congress and Exposition*, Pittsburgh, United States, September 2014.

[65] ISO 6469-3:2018, "Electrically propelled road vehicles - Safety specifications - Electrical safety," International Standards Organization, Standard, 2018.

[66] T. Janbein, "Vorrichtung und Verfahren zum Aufladen eines elektrischen Energiespeichers," *German Patent DE 102018221496 A1*, 31 October 2019.

[67] A. Mallik and A. Khaligh, "A Soft-Switching Strategy for Three-Phase Boost Power Factor Correction Rectifiers," in *IECON 2016 42nd Annual Conference of the IEEE Industrial Electronics Society*, Dallas, United States, October 2016.

[68] DIN EN IEC 60404-4:2009, "Magnetic materials - Part 4: Methods of measurement of d.c. magnetic properties of magnetically soft materials," International Electrotechnical Commission, Standard, 2009.

[69] J. Mühlethaler, J. Biela, J.-W. Kolar, and A. Ecklebe, "Core Losses Under the DC Bias Condition Based on Steinmetz Parameters," *IEEE Transactions on Power Electronics*, vol. 27, no. 2, pp. 953–963, 2012.

[70] M. S. Lancarotte, C. Goldemberg, and A. de Arruda Penteado, "Estimation of FeSi Core Losses Under PWM or DC Bias Ripple Voltage Excitations," *IEEE Transactions on Energy Conversion*, vol. 20, no. 2, pp. 367–372, 2005.

[71] C. Simao, N. Sadowski, N. J. Batistela, and J. P. A. Bastos, "Evaluation of Hysteresis Losses in Iron Sheets Under DC-biased Inductions," *IEEE Transactions on Magnetics*, vol. 45, no. 3, pp. 1158–1161, 2009.

[72] DIN EN IEC 60404-6:2020, "Magnetic materials - Part 6: Methods of measurement of the magnetic properties of magnetically soft metallic and powder materials at frequencies in the range 20 hz to 100 khz by the use of ring specimens," International Electrotechnical Commission, Standard, 2020.

[73] Z. Gmyrek, A. Cavagnino, and L. Ferraris, "Estimation of the Magnetic Properties of the Damaged Area Resulting From the Punching Process: Experimental Research and FEM Modeling," *IEEE Transactions on Industry Applications*, vol. 49, no. 5, pp. 2069–2077, 2013.

[74] M. Veigel, A. Krämer, G. Lanza, and M. Doppelbauer, "Investigation of the Impact of Production Processes on Iron Losses of Laminated Stator Cores for Electric Machines," in *2016 IEEE Energy Conversion Congress and Exposition*, Milwaukee, United States, September 2016.

[75] M. Bali and A. Muetze, "Influences of CO2 Laser, FKL Laser, and Mechanical Cutting on the Magnetic Properties of Electrical Steel Sheets," *IEEE Transactions on Industry Applications*, vol. 51, no. 6, pp. 4446–4454, 2015.

[76] M. Hofmann, H. Naumoski, U. Herr, and H.-G. Herzog, "Magnetic Properties of Electrical Steel Sheets in Respect of Cutting: Micromagnetic Analysis and Macromagnetic Modeling," *IEEE Transactions on Magnetics*, vol. 52, no. 2, pp. 1–14, 2016.

[77] K. Bourchas, A. Stening, J. Soulard, A. Broddefalk, M. Lindenmo, M. Dahlen, and F. Gyllensten, "Influences of Cutting and Welding on Magnetic Properties of Electrical Steels," in *2016 International Conference on Electrical Machines*, Lausanne, Switzerland, September 2016.

[78] A. Reinert Jürgen and Brockmeyer and R. W. A. A. De Doncker, "Calculation of Losses in Ferro- and Ferrimagnetic Materials Based on the Modified Steinmetz Equation," *IEEE Transactions on Industry Applications*, vol. 37, no. 4, pp. 1055–1061, 2001.

[79] Y. Yue Shuaichao and Li, Q. Yang, X. Yu, and C. Zhang, "Comparative Analysis of Core Loss Calculation Methods for Magnetic Materials Under Nonsinusoidal Excitation," *IEEE Transactions on Magnetics*, vol. 54, no. 11, pp. 1–5, 2018.

[80] J. Li, T. Abdallah, and C. R. Sullivan, "Improved Calculation of Core Loss with Nonsinusoidal Waveforms," in *Conference Record of the 2001 IEEE Industry Applications Conference. 36th IAS Annual Meeting (Cat. No.01CH37248)*, Chicago, United States, October 2001.

[81] K. Venkatachalam, C. R. Sullivan, and T. Abdallah, "Accurate Prediction of Ferrite Core Loss with Nonsinusoidal Waveforms Using Only Steinmetz Parameters," in *2002 IEEE Workshop on Computers in Power Electronics, 2002. Proceedings)*, Mayaguez, United States, June 2002.

[82] D. Bauer, *Verlustanalyse bei elektrischen Maschinen für Elektro- und Hybridfahrzeuge zur Weiterverarbeitung in thermischen Netzwerkmodellen*. PhD Thesis, University of Stuttgart, 2018.

[83] T. Lu, *Weiterentwicklung von hochtourigen permanenterregten Drehstromantrieben mit Hilfe von Finite-Elemente-Berechnungen und experimentellen Untersuchungen*. PhD Thesis, Technical University of Darmstadt, 2004.

[84] I. Boldea and S. A. Nasar, *The Induction Machine Handbook*. CRC press, 2001.

[85] D. Bauer, P. Mamuschkin, H.-C. Reuss, and E. Nolle, "Influence of Parallel Wire Placement On The ac Copper Losses in Electrical Machines," in *2015 IEEE International Electric Machines Drives Conference (IEMDC)*, May 2015.

[86] F. Stamer, R. Schwendemann, and M. Hiller, "A multi-dimensional full automatic power semiconductor test bench for accurate semiconductor loss calculation," in *PCIM Europe 2019, International Exhibition and Conference for Power Electronics, Intelligent Motion, Renewable Energy and Energy Management*, Nuremberg, Germany, May 2019.

[87] IEC 60747-9, "Semiconductor devices - discrete devices - part 9: Insulated-gate bipolar transistors (IGBTs)," International Electrotechnical Commission, Standard, 2007.

[88] C. Meza, D. Biel, J. Martinez, and F. Guinjoan, "Boost-Buck inverter variable structure control for grid-connected photovoltaic systems," in *IEEE International Symposium on Circuits and Systems*, Kobe, Japan, May 2005.

[89] M. Alaküla, P. Karlsson, and H. Bängtsson, *Power Electronics - Devices, Converters, Control and Applications*. Lund University, 2019.

[90] IEC 61000-3-12:2011, "Electromagnetic compatibility (EMC) - part 3-12: Limits - Limits for harmonic currents produced by equipment connected to public low-voltage systems with input current > 16 A and $\leq$ 75 A per phase," International Electrotechnical Commission, Standard, 2012.

[91] D. Tochigi, K. Takashima, T. Isobe, H. Tadano, and M. Tomoyuki, "Experimental Verification of a Model of Switching Transients Considering Device Parasitic Capacitance for the Loss Estimation of Soft-switching Power Converters," in *2019 IEEE 4th International Future Energy Electronics Conference*, Singapore, Singapore, November 2019.

[92] C. Roth, F. Birnkammer, and D. Gerling, "Analytical Model for AC Loss Calculation Applied to Parallel Conductors in Electrical Machines," in *2018 XIII International Conference on Electrical Machines*, Alexandroupoli, Greece, September 2018.

[93] IEC 62955:2016, "Residual Direct Current Monitoring Device to be used for Mode 3 charging of Electric Vehicle," International Electrotechnical Commission, Standard, 2016.

[94] R. Rodrigues, Y. Du, A. Antoniazzi, and P. Cairoli, "A Review of Solid-State Circuit Breakers," *IEEE Transactions on Power Electronics*, vol. 36, no. 1, pp. 364–377, 2021.

[95] R. Meyer, "Hochempfindlicher, allstromsensitiver Fehlerstromschutzschalter," *European Patent EP0035120A2*, 9 September 1981.

[96] STMicroelectronics, "SiC power modules for your electric vehicle design," *https://www.st.com/content/dam/pcim-2020/presentations/stmicroelectronics-pcim2020-sic-power-modules-for-your-electric-vehicle-designs.pdf*, July 2020.

[97] L. Zhang, X. Ruan, and X. Ren, "Second-Harmonic Current Reduction and Dynamic Performance Improvement in the Two-Stage Inverters: An Output Impedance Perspective," *IEEE Transactions on Industrial Electronics*, vol. 62, no. 1, pp. 394–404, 2015.

[98] H. Cha, T.-K. Vu, and J.-E. Kim, "Design and control of Proportional-Resonant controller based Photovoltaic power conditioning system," in *2009 IEEE Energy Conversion Congress and Exposition*, San Jose, United States, September 2009.

[99] X. Luo, Y. Du, X. H. Wang, and M. L. Chen, "Tripping Characteristics of Residual Current Devices Under Nonsinusoidal Currents," *IEEE Transactions on Industry Applications*, vol. 47, no. 3, pp. 1515–1521, 2011.